3D Microtumours fabricated by microfluidics: applications in ovarian cancer



Xingyun Yang

St Hilda's College

University of Oxford

A thesis submitted for the degree of

Doctor of Philosophy

Michaelmas 2023

Declaration

The research detailed in this thesis was carried out at the Chemistry Research Laboratory, University of Oxford, under the guidance of Prof Hagan Bayley. All the work presented here is my original contribution, except as explicitly mentioned in the text and acknowledgement of collaboration. The contents of this thesis have not been submitted for any other degree at this university or elsewhere.

Xingyun Yang

October 2023

Abstract

Physiologically relevant *ex vivo* models that accurately replicate features in patients are essential for studying diseases and advancing drug development. However, current *ex vivo* models, such as 2D monolayer cells and laboratory animals, fall short in providing biologically meaningful responses to stimuli.

This thesis describes the fabrication of 3D microtumours – a 3D cell model with tumour cells encapsulated in biocompatible hydrogels – by using a surfactant-free, droplet-based microfluidic platform. The microfluidic technique offers flexibility in the size and cell content of the 3D microtumours, which faithfully recapitulate key characteristics of tumours such as hypoxia, characteristic organisation of the cytoskeleton, and a dose-response to chemotherapeutics close to the physiological range. In addition to ovarian cancer cells, fibroblasts – a significant component of the tumour microenvironment – were incorporated into 3D microtumours to create the more complex interactions between cancerous and healthy tissues.

Finally, the 3D microtumours were employed to form the first 3D model of ovarian cancer minimal residual disease (MRD), which represents a cluster of chemotherapy-resistant cancer cells responsible for tumour relapse. The MRD 3D microtumours resembled cancers in MRD patients in: (1) upregulation of fatty acid metabolism genes; (2) non-genetic heterogeneity of five cell states. Furthermore, a fatty acid oxidation inhibitor, perhexiline, specifically elicited cytotoxicity in MRD ovarian cancer cells but not in bulk cancer cells.

Overall, this 3D microtumour system is ideal for high-throughput drug screening and might be readily adapted for different cancers, as well as accommodate multiple cell types found in complex tumour microenvironments.

Acknowledgements

I would like to express my heartfelt gratitude to all the people have been a part of my journey during my PhD.

First and foremost, my deepest appreciation goes to my family, who have provided unwavering support, endless love, and constant encouragement throughout all my time in this world. Your presence has been my greatest strength.

I am immensely thankful to my supervisor, Prof Hagan Bayley, for exceptional guidance and for imparting the essential skills that every researcher needs. My project collaborator, Prof Ahmed Ashour Ahmed from MRC Weatherall Institute of Molecular Medicine, University of Oxford, whose valuable insights have greatly enriched the meaningfulness of my research. My college advisor, Prof Lorna Smith, for generous guidance, advice, and support related to college life.

I express my sincere gratitude to Dr Linna Zhou, Dr Yujia Zhang from Bayley group, and Dr Mara Artibani from Ahmed group, for their professional assistance in experiments, insightful discussions and suggestions, and their time devoted to reading and providing feedback on this thesis. The entire Bayley group, for sharing exciting scientific endeavours and moments of laughter in the laboratory and in life. In particular, Dr Ravinash Krishna Kumar for guidance with microscopes, Ellina Mikhailova for teaching me tissue culture, Dr Matthew Cornall for organising fantastic group events, and Yuying Ding for sharing useful tips on diets and weight loss.

Last but not least, I would like to express my appreciation to my friends, idols and pets for brightening my life, especially during challenging times when experiments did not proceed as expected. A special thanks to Minghui Liao for always being there for me, Yian Hang for helping with biological questions and sharing ice creams, Chinese singer Zhou Shen for his ethereal voice, the South Korean boy band Super Junior and Lee Hyuk-jae for their unwavering commitment to the stage over the past 18 years, and my beloved pets for their comforting companionship.

Table of contents

Declaration ..... **i**

Abstract ..... **iii**

Acknowledgements ..... **v**

Table of contents ..... **vii**

List of abbreviations ..... **xi**

List of figures ..... **xv**

List of tables ..... **xix**

1 Introduction **1**

1.1 Ovarian cancer 1

1.1.1 Ovarian cancer statistics 1

1.1.2 Ovarian cancer treatment 3

1.1.3 Biophysical parameters of ovarian tissue 4

1.2 Minimal residual disease 5

1.3 Cancer models 7

1.4 3D cell culture technologies 11

1.4.1 Organoids 11

1.4.2 Spheroids 13

1.4.2.1. Scaffold-free spheroids 13

1.4.2.2. Scaffold-based spheroids 14

1.4.3 Organoids vs spheroids for drug screening 17

1.5 Microfluidic technique 18

1.6 Summary of thesis work 24

2 Microfluidic techniques for 3D microtumours fabrication **25**

2.1 Introduction 25

2.2 Fabrication of 3D microtumours by using the microfluidic platform 26

2.2.1 Hydrogels 27

2.2.2 Cell types 31

2.2.3 Cell density and oil 32

2.2.4 Flow rates and shape 35

2.2.5 Size 36
2.3 Characterisation for 3D microtumours 38
2.3.1 Cell assays 38
2.3.1.1 Caspase-Glo 3/7 Assay 38
2.3.1.2 CellTox Green Cytotoxicity Assay 40
2.3.1.3 RealTime-Glo MT Cell Viability Assay 41
2.3.1.4 CellTiter-Glo 3D Cell Viability Assay 42
2.3.1.5 PrestoBlue Cell Viability Assay 43
2.3.2 Cell viability during microfluidic fabrication 45
2.3.3 Long term culture 47
2.4 Summary 49

3 Anticancer drug responses of 3D microtumours 51
3.1 Introduction 51
3.2 Key physiological features recapitulated by 3D microtumours 53
3.2.1 Hypoxia 54
3.2.2 Cytoskeleton organisation 62
3.3 Size distribution of 3D microtumours 65
3.4 Anticancer drug dose-responsive curve 67
3.4.1 Workflow design for drug screening 67
3.4.2 Ovarian cancer 3D microtumours 70
3.4.3 Co-culture 3D microtumours 73
3.5 Cell migration in co-culture 3D microtumours 77
3.6 Summary 79

4 Modelling ovarian cancer minimal residual disease using 3D microtumours 81
4.1 Introduction 81
4.2 Preparation of MRD-mimicking cells 83
4.3 MRD characteristics in 3D microtumours 86
4.3.1 Transcriptomic analysis 87
4.3.2 Lipid transport and metabolism 91
4.3.3 ABC transporters and TIC/CSC markers 94
4.3.4 Non-genetic heterogeneity 97
4.4 FAO inhibitor responses 102

4.5 Transcriptomes FAO inhibitor-resistant 3D microtumours 107
4.6 Summary 113

5 Concluding remarks 117
5.1 Conclusion 117
5.2 Future directions 120

6 Materials and methods 123
6.1 Cell maintenance 123
6.1.1 Culture conditions 123
6.1.2 Cell harvesting, counting and cryopreservation 124
6.2 Cell-hydrogel suspension preparation 125
6.2.1 Matrigel 126
6.2.2 Collagen 126
6.2.3 Agarose 126
6.2.4 Silk fibroin 127
6.3 Microfluidics platform and 3D microtumour fabrication 127
6.3.1 Microfluidic chips 127
6.3.1.1. Drilling hole method 128
6.3.1.2. 3D printed master mould method 129
6.3.2 Microfluidic system setup 130
6.3.3 Fabrication of 3D microtumours 131
6.4 Characterisations of 3D microtumours 132
6.4.1 Size distribution 132
6.4.2 Cell viability 133
6.4.3 Hypoxic core staining 134
6.5 Anticancer drug responses 135
6.6 Minimal residual disease modelling 136
6.6.1 Preparation of MRD- mimicking cells 136
6.6.2 Fatty acid oxidation inhibitor responses 137
6.7 Transcriptomic analysis with bulk RNA-Sequencing 138
6.7.1 RNA extraction and library preparation 138
6.7.2 Processing of RNA-Seq data 138
6.8 Immunofluorescence staining 139

7 Bibliography 141

List of abbreviations

2D	Two-dimensional
3D	Three-dimensional
ABC	ATP-binding cassette
ACADVL	Very long-chain specific acyl-coenzyme A dehydrogenase
ACSL	Long-chain-fatty-acid-CoA ligase
AKR	Aldo-keto reductases
ATCC	American Type Culture Collection
ATP	Adenosine triphosphate
AUC	Area under curve
BSA	Bovine serum albumin
BME	Basement membrane extract
CAF	Cancer-associated fibroblast
CoA	Coenzyme A
CPT	Carnitine palmitoyl transferase
CSC	Cancer stem cell
CTC	Circulating tumour cell
ctDNA	Circulating cell-free tumour DNA
CV	Coefficient of variation
DAPI	4′,6-diamidino-2-phenylindole
DEGs	Differentially expressed genes
DFI	Disease-free interval
DMEM	Dulbecco’s modified Eagle’s medium

DMSO	Dimethyl sulfoxide
ECM	Extracellular matrix
EDTA	Ethylenediaminetetraacetic acid
EMT	Epithelial-mesenchymal transition
FAO	Fatty acid oxidation
FAP	Fibroblast activation protein
FASN	Fatty acid synthase
FBS	Fetal bovine serum
FDA	Food and Drug Administration
FDR	False discovery rate
GEMM	Genetically engineered mouse model
GFP	Green fluorescence protein
GFR	Glomerular filtration rate
GO	Gene ontology
GOBP	Gene ontology biological processes
HGSOC	High grade serous ovarian cancer
HIPEC	Hyperthermic intraperitoneal chemotherapy
HPLC	High-performance liquid chromatography
ID	Inner diameter
JCRB	Japanese Collection of Research Biosources
LGSOC	Low grade serous ovarian cancer
MEM	Minimum essential medium
MRD	Minimal residual disease
NADH	Reduced form of nicotinamide adenine dinucleotide
NADPH	Reduced form of nicotinamide adenine dinucleotide phosphate

NEAA	Non-essential amino acids
OCT	Optimal cutting temperature
PBS	Phosphate-buffered saline
PCA	Principal component analysis
PCR	Polymerase chain reaction
PDK	Pyruvate dehydrogenase kinase
PDMS	Polydimethylsiloxane
Pen-Strep	Penicillin-streptomycin
PFA	Paraformaldehyde
PTFE	Polytetrafluoroethylene
RFP	Red fluorescence protein
RFU	Relative fluorescence units
RLU	Relative luminescence units
RIN	RNA integrity number
RNA-Seq	RNA-Sequencing
RT	Room temperature
SCD	Stearoyl-coenzyme A desaturase
SD	Standard deviation
TIC	Tumour initiating cell
TME	Tumour microenvironment
VEGF	Vascular endothelial growth factor

List of figures

Figure 1.1. Classification of ovarian malignancies. 2

Figure 1.2. The current approach to treat cancer patients, monitor MRD and tumour recurrence. 6

Figure 1.3. Mouse model for cancer research. 10

Figure 1.4. Schematic overview of organoid establishment and application for drug screening. 12

Figure 1.5. Schematic diagram of scaffold-free technologies used for 3D tumour spheroids preparation. 14

Figure 1.6. Schematic diagram of scaffold-based techniques used for 3D tumour spheroids preparation. 17

Figure 1.7. Sketch showing difference in the maintenance of organoids and spheroids. 18

Figure 1.8. Schematic illustration of the fabrication of non-structured spheroids. 20

Figure 1.9. Schematic illustration of the fabrication of core-shell structure spheroids. 21

Figure 1.10. Schematic illustration of a microfluidic platform for therapeutic evaluation. 22

Figure 1.11. Schematic illustration of tumour extravasation modelled by a microfluidic system..... 23

Figure 2.1. Schematic illustration of the fabrication process of 3D microtumours by using the microfluidic platform. 27

Figure 2.2. 3D microtumours composed of OVCAR8 and different hydrogels. 29

Figure 2.3. Brightfield microscope images of 3D microtumours of various gelation time. 31

Figure 2.4. 3D microtumours prepared with cell-hydrogel suspensions of various cell densities. 35

Figure 2.5. 3D microtumours of various shapes. 36

Figure 2.6. 3D microtumours of various sizes. 37

Figure 2.7. Microfluidic chips and 3D microtumours in a PTFE exit tube. . 38
Figure 2.8. Caspase-Glo 3/7 Assay to monitor apoptosis in 3D microtumours. 39
Figure 2.9. CellTox Green Cytotoxicity Assay to quantify dead cells in 3D microtumours. 41
Figure 2.10. RealTime-Glo MT Cell Viability Assay to quantify viable cells in 3D microtumours. 42
Figure 2.11. CellTiter-Glo 3D Cell Viability Assay to quantify viable cells in 3D microtumours. 43
Figure 2.12. PrestoBlue Cell Viability Assay to quantify viable cells in 3D microtumours. 44
Figure 2.13. Range of linear correlation between fluorescence and cell number for PrestoBlue Cell Viability Assay. 45
Figure 2.14. Cell viability at three stages of microfluidic fabrication. 46
Figure 2.15. Long-term culture of 3D microtumours 47
Figure 2.16. Live/Dead staining of 3D microtumours on different days. 48
Figure 2.17. 3D microtumours composed various hydrogels on different days. 48
Figure 2.18. Size of 3D microtumours on different days. 49
Figure 3.1. Hypoxic core staining for 3D microtumours of various size 55
Figure 3.2. Immunofluorescence staining of hypoxia proteins for 3D microtumours. 56
Figure 3.3. Heatmaps showing the expression of hypoxic signature. 58
Figure 3.4. Dot plots showing the main gene ontology biological processes (GOBP) enriched in 3D microtumours. 60
Figure 3.5. Heatmaps showing the expression of cell cycle related genes. 61
Figure 3.6. Dot plots showing the main GOBP enriched in 2D cultures. ... 62
Figure 3.7. Cytoskeleton organisations of *in vitro* and clinical samples. ... 64
Figure 3.8. Size distributions of 3D microtumours 66
Figure 3.9. Schematic diagram showing the evaluation of chemotherapeutic responses with 3D microtumours 68
Figure 3.10. Optimisation of assay reagent incubation time for 3D microtumours. 69

Figure 3.11. Chemotherapeutics responses of OVCAR-5/RFP tumour cells. 70
Figure 3.12. Chemotherapeutics responses of co-culture (50: 50 mixture of OVCAR-5/RFP tumour cells and 3T3 fibroblast cells)..... 74
Figure 3.13. Chemotherapeutics responses of 3T3 fibroblast cells. 74
Figure 3.14. IC_{50} values for 3D microtumours and 2D cultures.. 76
Figure 3.15. Core-shell structure formed by distinct cell migration patterns in co-culture 3D microtumours. 78
Figure 4.1. Schematic diagram of the standard clinical management of patients with ovarian cancer. 84
Figure 4.2. Killing curves for preparing MRD-mimicking cells. 85
Figure 4.3. Principal component analysis (PCA) plot of RNA-Seq data from *in vitro* models and clinical samples. 88
Figure 4.4. DEGs of MRD *in vitro* models compared to clinical samples. . 89
Figure 4.5. Pathway enrichment in MRD 2D: cell cycle and division..... 90
Figure 4.6. Pathway enrichment in MRD 2D: metabolism..... 92
Figure 4.7. Heatmap showing the expression of genes in 3D microtumours and 2D cultures involved in lipid transport and metabolism. The gene list was derived from TOPPFUN Biological processes, response to lipid, GO:0033993. 93
Figure 4.8. Scatterplots showing the log_2 fold change (log FC) of genes involved in lipid metabolism. 94
Figure 4.9. Heatmap showing the expression of genes in 3D microtumours and 2D cultures encoding ABC transporters and TIC/CSC markers. 96
Figure 4.10. 3D microtumours stained with TIC/CSC marker: ALDH3A1. .. 96
Figure 4.11. Deconvolution analysis for 3D microtumours. 99
Figure 4.12. Deconvolution analysis for 2D cultures from literature. 100
Figure 4.13. Deconvolution analysis for organoids from literature. 101
Figure 4.14. Schematic diagram of the treatment of naïve and MRD cells with therapeutics. 103
Figure 4.15. Responses of 3D microtumours to etomoxir. 104
Figure 4.16. Responses of 3D microtumours to perhexiline. 105

Figure 4.17. Genes upregulated in etomoxir-resistant MRD 3D microtumours. 108
Figure 4.18. Etomoxir-resistant 3D microtumours stained with FAO marker. 109
Figure 4.19. Genes upregulated in perhexiline-resistant MRD 3D microtumours. 112
Figure 4.20. Perhexiline-resistant 3D microtumours stained with lipid metabolism marker. 113
Figure 6.1. A microfluidic chip created by drilling hole method. 128
Figure 6.2. A reverse mould for the microfluidic chip. 130
Figure 6.3. Example of size measurement for a 3D microtumour with an elliptical cross-section. 132

List of tables

Table 2.1. Summary of biocompatible hydrogels and their preparation conditions used in 3D microtumour fabrication. 31

Table 2.2. Summary of cells used in 3D microtumour fabrication. 32

Table 2.3. Density of oil or cell culture medium used in phase separation. 33

Table 2.4. Cell viability data at three stages of the microfluidic fabrication. 46

Table 3.1. Dimensions of 3D microtumours of various size groups and compositions. 67

Table 3.2. Calculations for theoretical carboplatin C_{max} and the *in vitro* equivalent dose. 72

Table 3.3. IC_{50} values calculated from carboplatin and paclitaxel dose-response curves. 76

Table 3.4. Comparison of paclitaxel IC_{50} values in co-culture over OVCAR-5/RFP 77

Table 4.1. Optimised conditions for preparing MRD-mimicking cells. 85

Table 4.2. Summary of DEGs number of MRD *in vitro* models compared to clinical samples. 89

Table 4.3. Responses comparison between naïve and MRD 3D microtumours to etomoxir. 104

Table 4.4. Cell viability comparison between etomoxir treated and DMSO control group for 3D microtumours. 104

Table 4.5. Responses comparison between naïve and MRD 3D microtumours to perhexiline. 106

Table 4.6. Killing effect comparison between naïve and MRD 3D microtumours. 106

Table 6.1. Protocol for differentiation of 3T3-L1 cells into adipocytes. 124

Table 6.2. Microplate reader settings for fluorescence intensity measurement to evaluate cell viability. 134

Table 6.3. List of antibodies used for immunofluorescence staining. 140

1 Introduction

1.1 Ovarian cancer

1.1.1 Ovarian cancer statistics

Ovarian cancer represents one of the biggest threats in gynaecological malignancies, with an incidence rate of 3.4%, ranking it eighth, and a mortality rate of 4.7%, ranking it fifth among women worldwide[1]. In the United Kingdom, ovarian cancer is associated with a low 10-year survival rate of 35%[2], which is considerably lower than the 54% survival rate for all cancer combined in females[3]. Despite continuous efforts to ameliorate patient prognosis, the 10-year survival rate for ovarian cancer has shown improvement from 18% in 1971-1972 to 35% in 2010-2011. However, it still lags behind the average 10-year survival rate for all cancers combined, which has increased from 25% to 50% over the same period[4].

Ovarian cancer can be categorised into two primary groups: epithelial ovarian cancer, constituting approximately 95% of cases, and non-epithelial ovarian cancer, accounting for roughly 5% of cases (**Figure 1.1**)[5]. Within epithelial ovarian cancer, two distinct molecular profiles give rise to Type I and Type II tumors[6]. Type I epithelial ovarian cancer, characterised by mutations like KRAS or BRAF, tends to be less aggressive and more indolent, typically occurring in younger patients[7]. On the other hand, Type II tumour acquires major gene alterations in TP53, BRCA1 and BRCA2, making them more aggressive and frequently diagnosed[8]. Histologically, epithelial ovarian cancer can be further

subdivided into four subtypes: serous, endometrioid, mucinous, and clear cell ovarian cancer[9]. The most prevalent morphology is serous subtype, which is classified as low grade serous ovarian cancer (LGSOC, 5 to 10%) when characterised by Type I pathways, and high grade serous ovarian cancer (HGSOC, 70 to 90%) when associated with Type II pathways. Other cell morphologies following Type I pathways include endometrioid (10%), clear cell (10%) and mucinous (3%)[5]. Non-epithelial ovarian cancer originates from cells such as germ cell and sex-cord stromal, with extremely rare cases including small cell carcinomas and ovarian sarcomas[10].

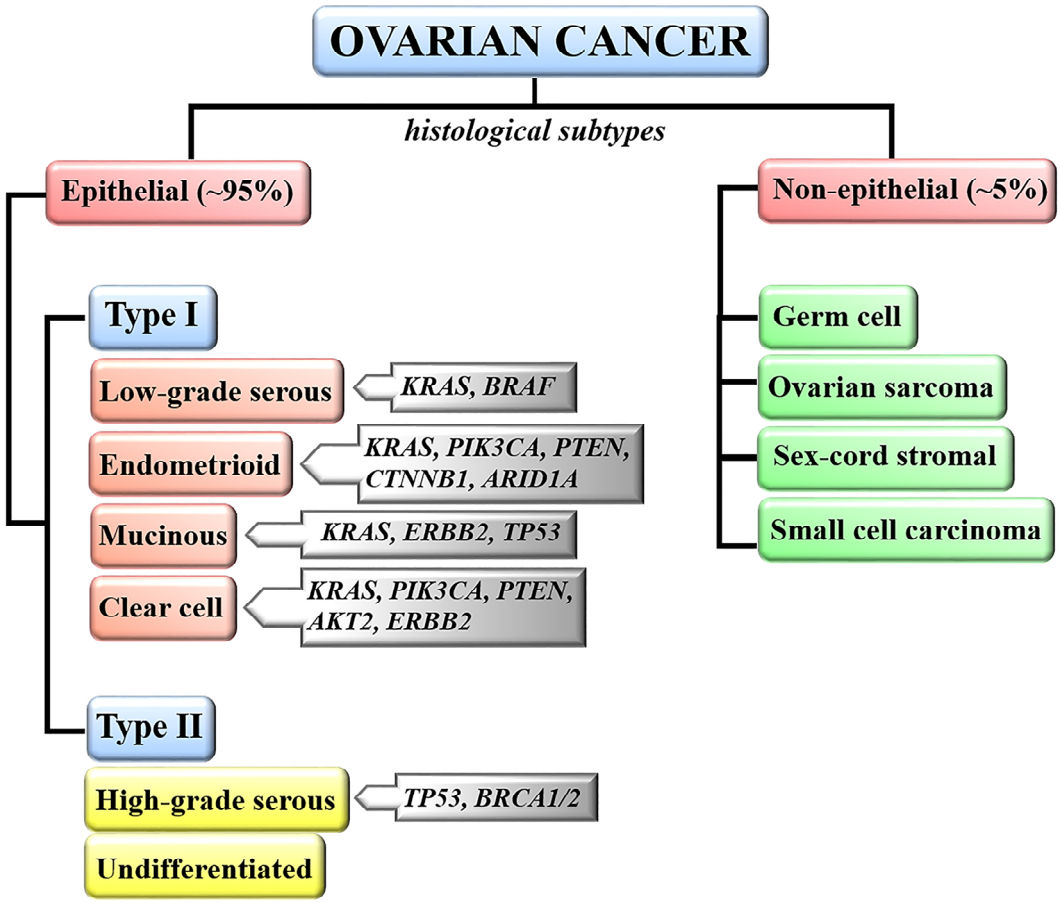


Figure 1.1. Classification of ovarian malignancies. Reprinted from Cybula et al.[5]. The grey boxes indicate the most typically mutated genes for each ovarian cancer subtype.

1.1.2 Ovarian cancer treatment

The standard first-line treatment for ovarian cancer involves a combination of cytoreductive surgery and platinum-based chemotherapy, typically utilising carboplatin and paclitaxel[11]. Despite this treatment approach, recurrence occurs in approximately 70% of patients after their initial treatment, and a significant proportion of these relapses involve platinum resistance[12]. Recurrence is categorised based on the disease-free interval (DFI), which represents the time between the completion of first-line treatment and the initial cue of recurrence. These categories include platinum-resistant (DFI <6 months), partially sensitive to platinum (DFI between 6 and 12 months), and platinum-sensitive (DFI >12 months) relapses[13].

The standard second-line chemotherapy for recurrent disease also involves platinum-based treatments, which may include drugs like topotecan, liposomal doxorubicin, oral etoposide, altretamine, and gemcitabine[14]. Among these treatments, platinum-sensitive patients typically achieve a response rate of at least 30%, whereas the response rate for platinum-resistant patients is significantly lower, ranging from 10% to 25%[15].

Platinum resistance in ovarian cancer can result from various factors related to the mechanism of platinum action. These factors encompass platinum uptake into cells, its binding to DNA, the formation of DNA-platinum adducts, the activation of apoptosis due to DNA damage, and cellular processes that indirectly disrupt platinum action[16, 17]. When dealing with platinum-resistant relapse, treatment options include chemotherapy, hormonal therapy, targeted therapy, and immunotherapy[18]

An alternative approach to improve the poor response rate involves the use of targeted therapies. These therapies include agents like bevacizumab, which targets vascular endothelial growth factor (VEGF), cediranib, which inhibits VEGF-dependent tyrosine kinase, and trebananib, which targets angiopoietin 1 and 2[13]. When comparing platinum-based chemotherapy (weekly paclitaxel, pegylated liposomal doxorubicin or topotecan) with the same agents used concurrently with the targeted agent bevacizumab, the latter approach led to a significant increase in the overall response rate, rising from 12.6% to 30.9% [13, 19].

When considering maintenance treatment following recurrence, various factors should be taken into account, including fundamental aspects like the overall response rate, overall survival, risk of heightened neurotoxicity, extended time to progression or recurrence (DFI), as well as the impact on the patient's quality of life[13, 20].

1.1.3 Biophysical parameters of ovarian tissue

Understanding the biophysical characteristics of ovarian tissue is crucial for establishing appropriate *in vitro* models and developing treatment strategies for ovarian cancer

The ovarian ECM primarily consists of two components: the basal lamina, represented by laminin and collagen type IV, and the interstitial matrix, mainly composed of fibrillar collagen (types I and III) and fibronectin[21]. Remodelling of ECM components, such as laminin-γ2[22], collagen I/III peptides[23], and CD44[24], has been linked to poor prognosis in ovarian cancer.

The stiffness of the ovary is age-associated, with the Young's modulus ranging from approximately 3 kPa for reproductive-age ovaries, around 6.5 kPa for prepubertal ovaries, and around 7 kPa for menopausal ovaries[25].

Hypoxia, resulting from oxygen deficiency, promotes angiogenesis and metastasis of tumours[26, 27]. The partial pressure of oxygen variates among different organs and tissues[28]. The oxygen tension is 2-8% in ovarian cortex as estimated by mathematical modelling[29], and it is approximately 5-7% in the fallopian tube[30].

1.2 Minimal residual disease

Despite the extensive research efforts dedicated to ovarian cancer, patient survival rates, especially in advanced stages, continue to be less than optimistic. The low survival rate associated with ovarian cancer can be attributed to various factors, including difficulty in early detection[31], lack of specific biomarkers, non-specific and insidious symptoms[32], the quick progression of ovarian cancer from an early to advanced stage in just one year[1], and a high recurrence rate[12].

In 75% of cases, patients present an advanced stage ovarian cancer upon diagnosis[18]. While over 80% of patients typically respond positively to initial treatment, most of them eventually acquire resistance to chemotherapy, leading to advanced recurrence and, ultimately, mortality[32]. Possible mechanisms for ovarian cancer recurrence involve multidrug resistance, DNA damage repair, cell cycle regulation, metabolic reprogramming, oxidative stress, cancer stem cells (CSC), immune response, and tumour dormancy[12, 33]. These chemotherapy-resistant tumour cells, which linger in a patient following treatment and are undetectable through current medical imaging techniques, are referred to as

minimal residual disease (MRD) (**Figure 1.2**)[34]. Targeting these resistant MRD cells is pivotal role for enhancing cancer patients' survival rates, not only in the context of prevention and early detection strategies, but also in the pursuit of novel therapeutics.

In 2018, the Food and Drug Administration (FDA) first approved the incorporation of MRD assessment in treatment decisions for B-cell precursor acute lymphoblastic leukaemia[35]. Since then, the detection and evaluation of MRD have been well-established and extensively applied in haematological malignancies for predicting or monitoring relapse[36]. Based on biomarkers of circulating tumour cells (CTCs) and circulating cell-free tumour DNA (ctDNA) in the bloodstream[34], MRD can be assessed by using techniques, such as polymerase chain reaction (PCR) and multiparametric flow cytometry[37]. However, applying this practice to solid tumours remains difficult, primarily due to low concentration of CTCs and ctDNA released into the bloodstream from tumour sites[36].

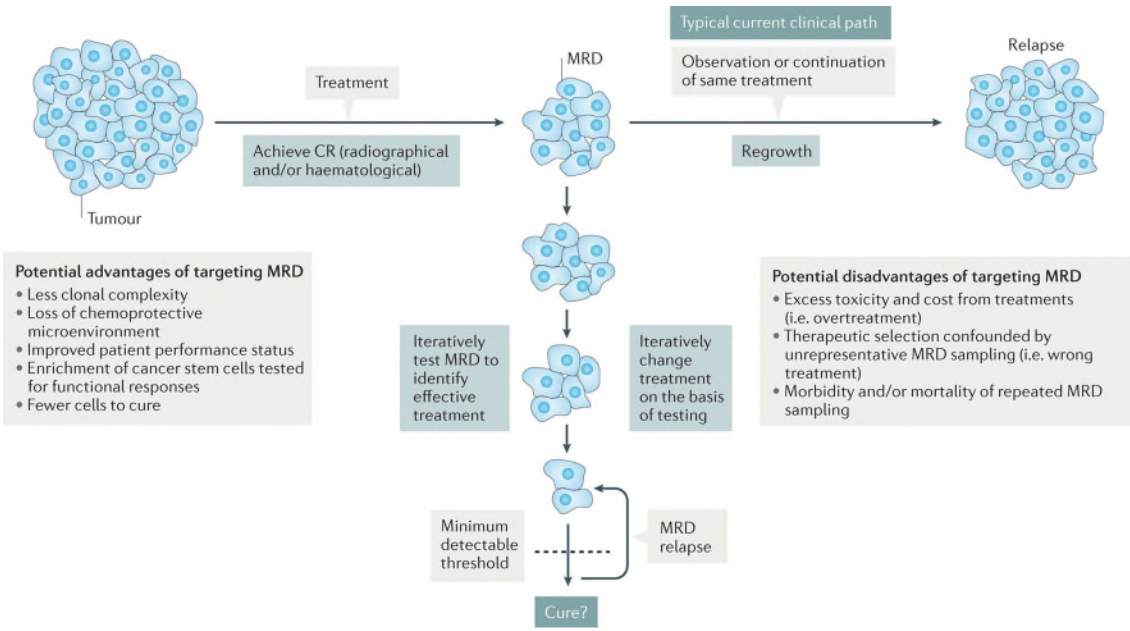


Figure 1.2. The current approach to treat cancer patients, monitor MRD and tumour recurrence. Reprinted from Luskin et al.[38].

The direct isolation and characterisation of MRD cells in patients with solid tumours present significant challenges. Unlike patients with leukaemia, where MRD cells can be extracted from the bone marrows, individuals with solid tumours who have undergone cytoreductive surgery often have MRD cells in uncertain locations. Additionally, invasive biopsy procedure is necessary for sampling sites like the liver, lung, and spleen[38]. Due to these obstacles, our understanding of MRD biology remains limited, and there is a lack of suitable experimental models that can serve as screening platforms for identifying effective compounds.

Ovarian cancer stands out as one of the few solid tumours for which direct characterisation of clinical MRD has been successfully accomplished. In a study by Artibani et al., transcriptomic analysis of biopsies from a cohort of 17 ovarian cancer patients revealed MRD molecular signatures related to tumour-initiating cells (TICs), lipid metabolism, and epithelial-mesenchymal transition (EMT)[39]. Targeting these therapeutic vulnerabilities holds the potential to effectively address and treat MRD, thereby contributing to delaying or preventing relapses.

1.3 Cancer models

In order to advance our comprehension of tumour biology and the progress of tumour therapies, diverse cancer models have been developed and utilised in recent decades. However, high failure rate of over 90% in translating anticancer drugs from preclinical trials to humans has led to disappointing results[85]. More realistic and predictive cancer models are desired to address this challenge.

Broadly speaking, the prevailing models include two-dimensional (2D) monolayer cells, laboratory animals, and 3D culture systems, all of which have different balances of feasibility, accuracy and cost.

Conventional 2D monolayer cells offer a simple, cost-effective, and time-efficient method for pharmaceutical testing. These cells are typically grown on flat surfaces such as glass or polystyrene, making them valuable for identifying inherent vulnerabilities in cancer cells[40]. However, growing realisation has emerged that such monolayer cells are insufficient to present cancer complexity and heterogeneity[41]. Factors like external mechanical factors, unrestricted access to nutrients, oxygen and signal molecules can alter cell phenotypes and behaviours[42, 43]. For instance, monolayer cells in 2D support remodel chromatin structure to adopt a flattened shape, leading to modifications in gene expression[44]. Additionally, limited cell-cell and cell-extracellular matrix (ECM) interactions in 2D cultures induce unnaturally rapid proliferation, poor differentiation, and heightened sensitivity to cytotoxic agents[42, 45]. Failure in recreating tumour microenvironment (TME), which is significant in tumour progression, remains another setback of 2D monolayer system. While it's possible to co-culture tumour cells with stromal cells in 2D, Wang et al. reported the prostate cancer cells exhibited no genetic or behavioural changes when co-cultured with prostate stroma, reflecting the absence of meaningful cancer-microenvironment interactions in monolayer cultures[46]. Therefore, the traditional 2D model may be inadequate in delivering biologically relevant responses to interventions.

Animal models, ranging from rodents to companion animals, have been frequently used in cancer research. In particular, mice have been most widely

exploited due to their small size, short gestation time, relatively low maintenance costs (compared to other animals), and genetic manipulability[47]. Among mouse models, two main types are commonly employed: xenograft mouse models and genetically engineered mouse models (GEMMs). In xenograft models, human tumour cells are injected into immunodeficient mice to develop subcutaneous tumours, which are then used for testing anticancer drugs. On the other hand, GEMMs involve the activation of oncogenes or inactivation of tumour-suppressor genes to mimic the genetic and biological evolution of tumours (**Figure 1.3**)[48].

Mouse models provide valuable insights to unravel complex crosstalk between distant organs and tumours, and to identify potentially systemic risks associated with therapy[49, 50]. These aspects are challenging to replicate in oversimplified 2D tumour cultures. However, mouse models come with their own limitations, including high costs, time-consuming nature, and ethical concerns. Moreover, they often fail to precisely replicate human diseases, accurately predict treatment efficacy, or capture the side effects of therapies, such as liver toxicity[45, 51]. For instance, while mouse models can be used to study metastatic ovarian cancer, they present inherent differences in reproductive physiology[52] and omental anatomy, which is one of the most common sites for MRD[53]. Additionally, mice do not naturally develop ovarian tumours, further limiting their relevance in ovarian cancer research.

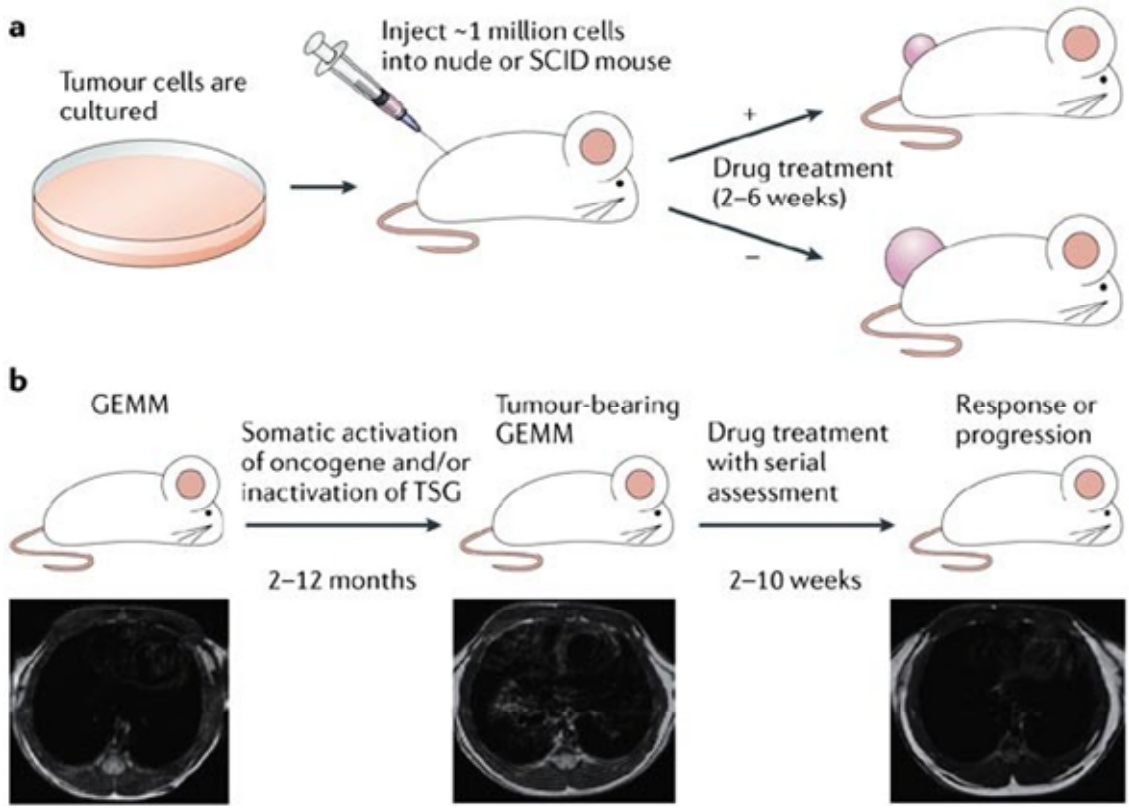


Figure 1.3. Mouse model for cancer research. (a) Xenograft versus (b) genetically engineered mouse model (GEMM). Reprinted from Sharpless and DePinho[48].

Three-dimensional (3D) culture was first reported in 1968. However, the field saw relatively low publication activity, with only around 10 publications per year in the 1990s. This changed dramatically around the year 2000 when there was a rapid increase in interest and research activity in 3D cell cultures. In recent years, there have been approximately 500 publications annually in this field[54, 55], indicating a gaining significance and popularity of 3D cell cultures within the research community.

3D system fills the space between conventional 2D culture and *in vivo* animal model. It recreates complicated structure and microenvironment that closely resemble those found in actual tumours more effectively than 2D model[56]. For example, transcriptomic analysis of 3D spheroids prepared from ovarian cancer ascites has revealed that while 2D monolayers support cell proliferation and

tumour growth pathways, 3D spheroids capture additional characteristics of cholesterol and lipid metabolism[57]. These metabolic features are particularly relevant to metastatic disease[57]. On the other hand, 3D culture derived from human cells outperforms a mouse model in terms of higher physiological relevance, a more precise representation of tumour features and metabolic profiles, as well as enhanced throughput for drug discovery[58, 59]. Considering the above advantages, this thesis concentrates on the use of 3D culture system for investigating ovarian cancer.

1.4 3D cell culture technologies

Representative 3D cell culture models encompass organoids and spheroids, which differ in terms of cellular origins and methods employed for their establishment and maintenance[60].

1.4.1 Organoids

Organoids are self-organising, organotypic 3D structures derived from stem cells *in vitro*[61]. A landmark study by Sato et al. in 2009 established small-intestinal crypt-villus organoids from single stem cells[62], boosting the development of organoids built from various other tissues[63]. Organoids share similar cellular composition and structural features with the tissues they are derived from, making them valuable for a wide range of applications, including translational therapy, genetic disease modelling, and drug discovery[64].

Beyond their initial utility in investigating normal development, organoids have been extended for the study of tumorigenesis. Tumour organoids (or

“tumoroids”), generated from clinical samples, present critical structures, intratumoral heterogeneity, and functional features that closely resemble their *in vivo* counterparts[64, 65], which underpins precision medicine for cancer patients with *in vitro* organoid models.

In particular, ovarian cancer organoids have been generated to enhance our comprehension of the disease. For instance, Kopper et al. developed organoids from patients representing all major subtypes of ovarian cancer to explore both intrapatient and interpatient heterogeneity[66]. Additionally, Lõhmussaar et al. utilized CRISPR genome editing in organoids to access the origins of ovarian cancer[67].

A typical protocol for establishing organoids begins with mechanical fragmentation and enzymatic digestion of primary tissues to dissociate them into single cells or small clusters of cells. These cells are then embedded in an ECM, basement membrane extract (BME) like Matrigel or Geltrex, and supplemented with culture medium (**Figure 1.4**)[68]. Passage of organoids can be accomplished through mechanical dissociation or enzymatic digestion methods[62, 68].

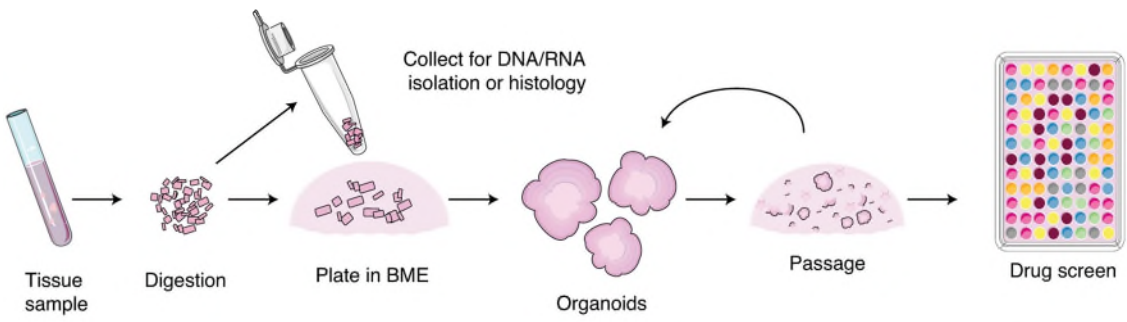


Figure 1.4. Schematic overview of organoid establishment and application for drug screening. Reprinted from Driehuis et al.[68].

Tumour organoids used for drug screening are typically dissociated into single cells or small clumps of cells before therapeutics administration[69].

However, this approach overlooks factors like organoid geometry, drug concentration gradients within each organoid, and the spatial arrangement of different cell types within the organoid. Consequently, the outcomes of these assays reflect the drug responses of a collection of cells, rather than individual organoids. Since organoids exhibit genetic and histological similarities to their parental tumours, improving drug screening methods to address these drawbacks could lead to more reliable results.

1.4.2 Spheroids

Cancer spheroids are self-organising 3D cultures derived from cell lines or primary tumour cells and display prominent intercellular interactions[64]. Spheroids can be categorised into two types depending on the presence of mechanical supports: scaffold-free or scaffold-based.

1.4.2.1. Scaffold-free spheroids

Scaffold-free approaches induce cell aggregation into microspheres under non-adherent conditions. Static technologies, like hanging-drop and forced floating, utilise hydrophobic surfaces to prevent cell attachment to plates. Dynamic flow technologies, like microgravity and stirring tank bioreactors, maintain constant agitation in the solution to keep the cells suspended (**Figure 1.5**)[70]. These methods encourage interactions between cells while suppressing interactions between cells and the substrate, facilitating intercellular adhesion to generate multicellular aggregates[65]. Initially, the cell aggregates are loosely assembled, but over time, they begin to secrete their own ECM and undergo proliferation, ultimately forming compact, solid tumours[71].

Scaffold-free methods offer several advantages, including simplicity, relatively inexpensive culture setup, and easy access to the spheroids[72]. However, they also come with certain drawbacks, such as the need for intensive labour, poor control over cell number or spheroid size, and challenges in generating large-sized tumour spheroids[65], all of which need to be addressed before scaffold-free spheroids can be routinely employed in clinical drug screening applications.

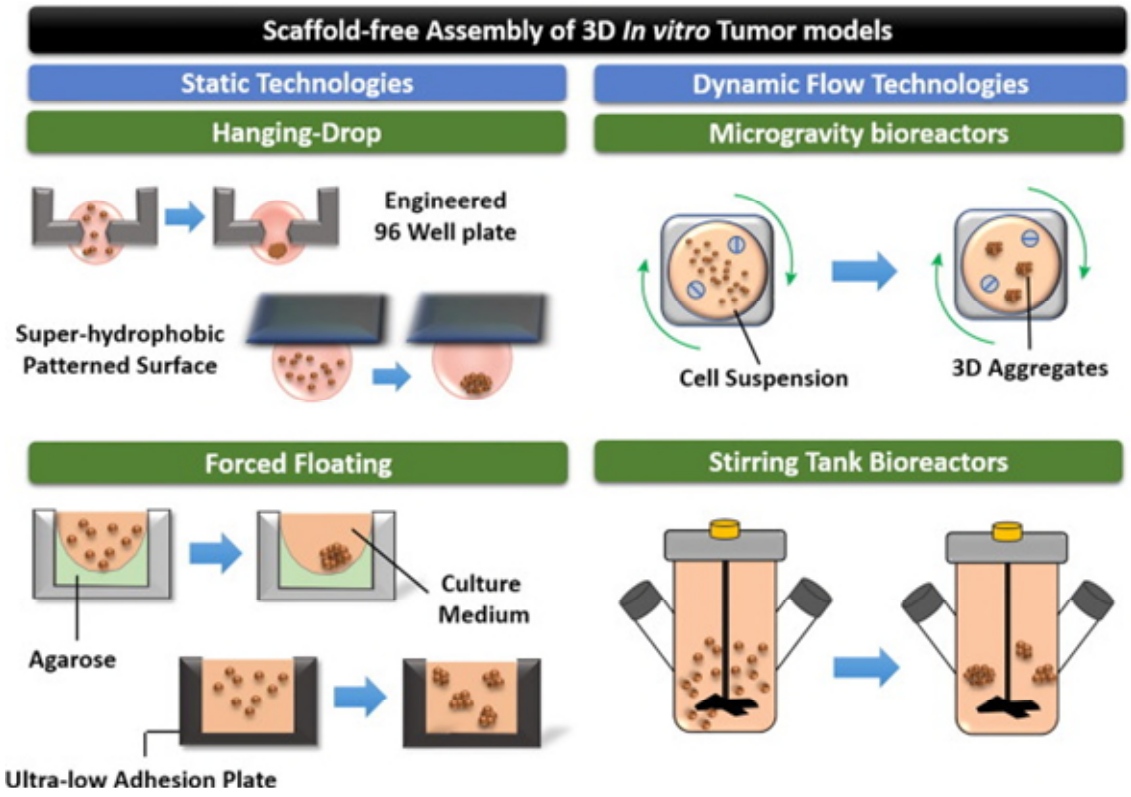


Figure 1.5. Schematic diagram of scaffold-free technologies used for 3D tumour spheroids preparation. Reprinted from Ferreira et al.[70].

1.4.2.2. Scaffold-based spheroids

Scaffold-based systems employ acellular biocompatible materials to provide structural support for cell growth in 3D culture[73]. Within these scaffolds, cells undergo proliferation and establish crucial cell-cell and cell-ECM interactions.

This results in the preservation of natural 3D cellular structures, rather than the flattening that occurs in 2D culture systems[74].

The scaffold material options span from natural hydrogels to synthetic or hybrid polymers, with the goal of providing a milieu that closely mimics TME[70]. When choosing a scaffold for spheroid formation, it is important to carefully consider key material properties like stiffness, biodegradability, and porosity[75]. The selection should be tailored to the specific origin of cells and the research objectives. Natural hydrogels, such as Matrigel, collagen, and hyaluronic acid, and synthetic polymers like polyethylene glycol (PEG), are commonly used for creating 3D tumour spheroids[70]. To be noticed, the synthetic materials lack naturally occurring bioactive cues for cell adhesion. Therefore, the synthetic polymers may require chemical modifications to introduce cell adhesive moieties, such as covalent attachment of arginylglycylaspartic acid (RGD) peptides[75].

Matrigel, extracted from mouse sarcoma, is widely recognised as the gold standard hydrogel for cultivating 3D tumour constructs originating from various organs, including breast cancer, gastrointestinal tumours, and pancreatic cancer[65, 70, 72]. It encompasses all the components typically found in the basement membrane and demonstrates high biological activity. Matrigel has proven to be highly valuable in supporting tumour growth, assessing tumour cell invasiveness, and mirroring a more differentiated phenotype in epithelial cell types[76, 77]. As a result, Matrigel emerges as a strongly recommended scaffold material for conducting 3D cultures of epithelial ovarian cancer, as emphasised in this thesis.

Scaffold-based spheroids can be fabricated using various techniques, including gel embedding, bioprinting, microfluidics and microwell arrays (**Figure**

1.6). In the gel embedding method, cells can be seeded either on top of the hydrogel or within the pre-gel solution, allowing the cells to become embedded within the hydrogel networks as it undergoes polymerisation[78]. The bioprinting approach employs a 3D printer to pattern cells and biomaterials in a spatial manner. Depending on the viscoelastic properties of the pre-gel solutions and the crosslinking mechanisms involved, 3D spheroids can be created using various bioprinting methods, including droplet-based, extrusion-based, and laser-assisted bioprinting[79]. The microfluidic platform allows the formation of 3D spheroids, their on-going culture and subsequent analysis of cellular interactions and drug efficacy within the chambers of specially designed microfluidic chips[80, 81]. Further details about the microfluidic technique are provided in Section 1.5. The microwell arrays method involves manufacturing of tiny wells of miniature dimensions using photolithography technique. Within these microwells, 3D spheroids with precise control over size and shape can be produced in a high-throughput manner[65, 82].

Overall, the scaffold-based approaches offer better control over size of spheroids compared to scaffold-free methods. They enable spheroid culture under optimised conditions tailored to the specific cell types, using scaffold materials with customisable mechanical and chemical properties. Despite some limitations, like reduced cell viability during fabrication, challenges related to retrieving cells without damage, and the ongoing need for cell-hydrogel suspension optimisation, fabrication techniques in this field continue to advance. The choice of which technique to use should be guided by the properties of the scaffold materials being employed.

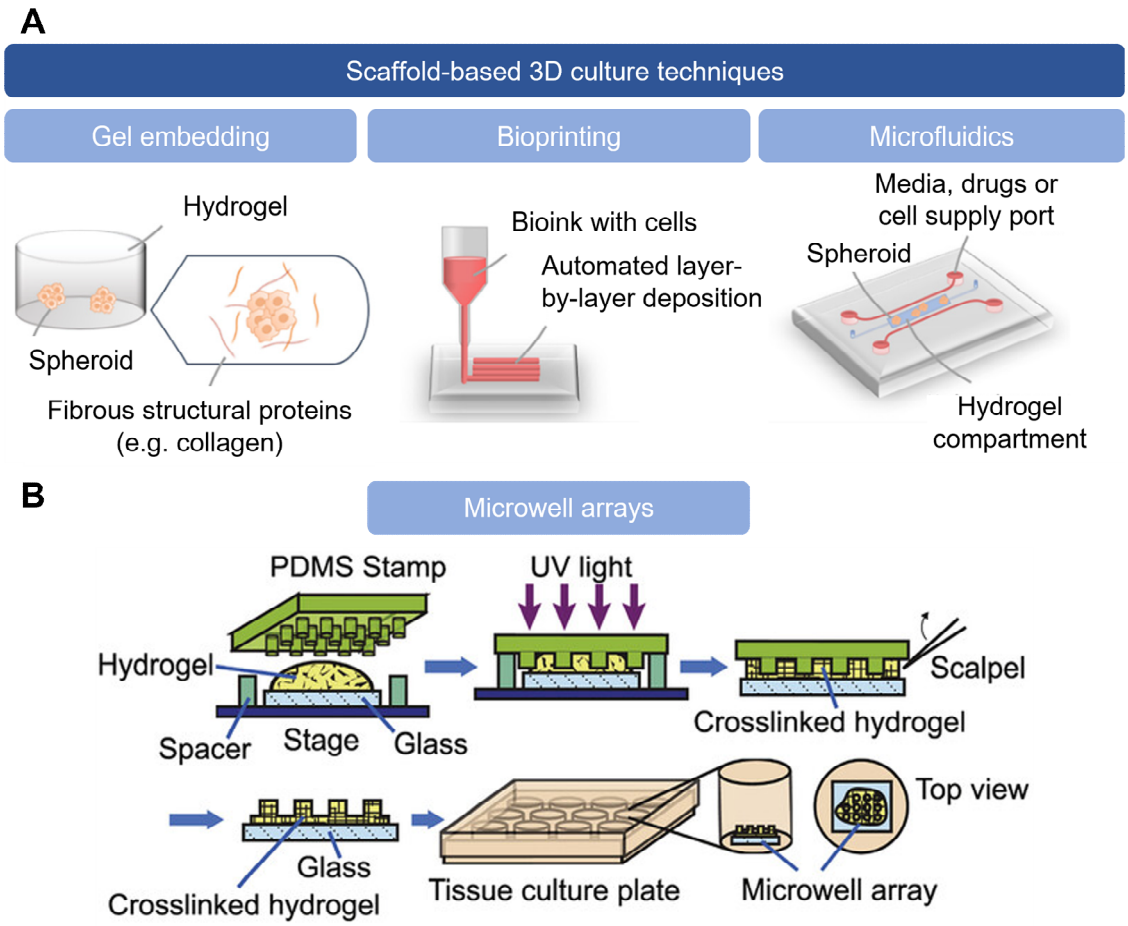


Figure 1.6. Schematic diagram of scaffold-based techniques used for 3D tumour spheroids preparation. (A) Gel embedding, bioprinting and microfluidics techniques illustration reprinted from Barbosa et al.[80]. (B) Schematic diagram of the microwell arrays fabrication process of hydrogel-based 3D tumour culture. Reprinted from Casey et al.[82].

1.4.3 Organoids vs spheroids for drug screening

One of the compelling reasons to employ 3D cell culture for drug screening is the more realistic penetration gradient it offers toward the centre of the 3D structure, as opposed to 2D monolayer cultures[83]. This gradient is an important pharmacokinetic feature that can affect the effectiveness of therapeutics and the rate of drug diffusion[72]. However, organoids are typically dissociated into single cells or small cell clusters before drug treatment[69], which does not accurately replicate the penetration gradient as observed in *in vivo* tumours. Moreover,

individual organoids can vary in size[84] and are difficult to separate from the surrounding matrix without causing damage (**Figure 1.7**A). In contrast, with most spheroid manufacturing techniques, individual 3D tumour spheroids are naturally separated during fabrication (**Figure 1.7**B). This eliminates the need for further dissociation before conducting therapeutic tests. Furthermore, scaffold-based spheroids typically offer superior control over their size. Consequently, spheroids emerge as a more favourable model compared to organoids for evaluating the efficacy of anticancer drugs.

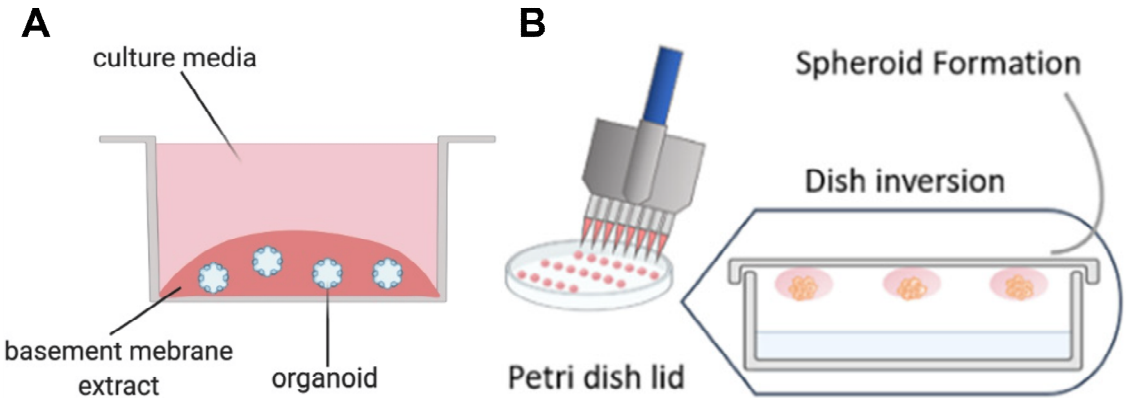


Figure 1.7. Sketch showing difference in the maintenance of organoids and spheroids. (A) Organoids were embedded in BME and submerged in the culture media. Reprinted from Gunti et al.[60]. (B) Spheroids formed by hanging drop method were kept in a humidified chamber. Reprinted from Barbosa et al.[80].

1.5 Microfluidic technique

Microfluidics uses microchannels, typically ranging in size from tens to hundreds of micrometres, to manipulate miniatured volume of fluids, spanning from 10^{-9} to 10^{-18} litres[85]. This technology, which originated from the microelectronics industry, first demonstrated its application in inkjet printing in 1965[86]. Microfluidic devices are predominantly made from polydimethylsiloxane (PDMS), a transparent, soft, hydrophobic and biocompatible elastomer[87]. These

characteristics make PDMS microdevices highly valuable and promising tools in various bio-related research areas, including cell culture, biomarker analysis, and disease diagnosis[88]. As fabrication techniques advance, microfluidic devices can integrate components beyond simple channels, such as valves[89], mixers[90], and pumps[91], to achieve more complex functions.

Following breakthrough developments in around 2005 that addressed previously unmet needs in microfluidics 3D cell culture[92], the technique has thrived in various applications. These applications encompass the fabrication and cultivation of spheroids, the exploration of interactions among different cell types, the evaluation of therapeutics, and investigation into cancer metastasis.

Microfluidics offers unique advantages over other *in vitro* models, primarily due to its significant improvement in physiological relevance. This improvement is achieved through precise control of the cellular, physical, and biochemical microenvironment. Additionally, microfluidics enables the investigation of essential biomechanical processes by allowing control over fluid flows, which is a distinct capability in this technology[93].

3D spheroids can be prepared by a droplet-based microfluidic approach. Wang et al. reported the fabrication of tumour spheroids by single-emulsion (for example, water-in-oil) (**Figure 1.8**). In this process, a mixture of cells and alginate (the aqueous phase) formed droplets when it came into contact with mineral oil at a cross-junction due to their different interfacial properties. These droplets were then polymerised to produce solid spheroids when they were dripped into a bath containing Ca^{2+} ions[94].

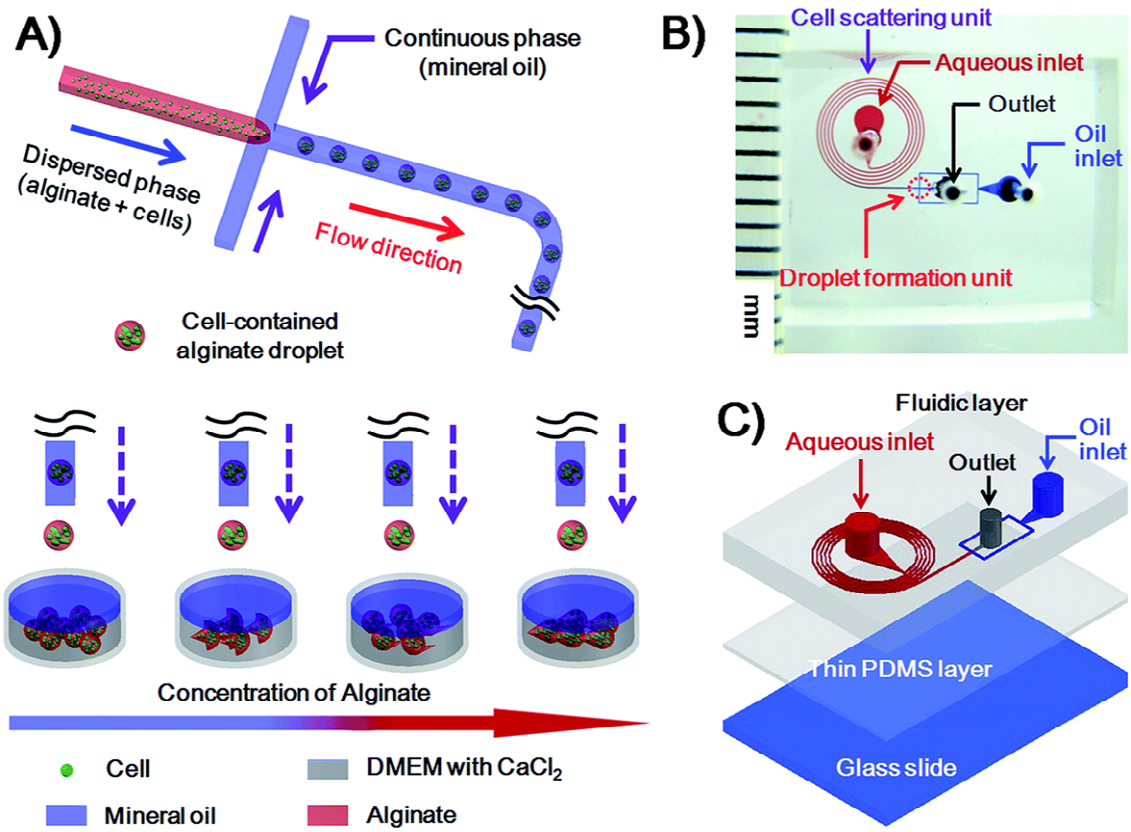


Figure 1.8. Schematic illustration of the fabrication of non-structured spheroids. (A) Single-emulsion 3D spheroids of cells encapsulated in alginate hydrogel were prepared using a droplet-based microfluidic approach. An overview (B) and construction (C) of the microfluidic device. Reprinted from Wang et al.[94].

The microfluidic system is capable of producing complex droplet structures, such as core-shell spheroids. An example of this was demonstrated by Chen et al., who introduced a 3D liver model consisting of hepatocyte cores and fibroblast shells using a double-emulsion process (for example, water-in-water-in-oil) (**Figure 1.9**). Hepatocytes suspended in medium (forming the inner phase) and fibroblasts in alginate aqueous solution (comprising the middle phase) created a laminar flow due to their low Reynolds numbers (below the value of 2000[95]). The Reynold number is defined as

$$Reynold\ number = \frac{\rho u L}{\mu}$$

where ρ is the density of the fluid, u represents the flow speed, L is the characteristic length, and μ is the dynamic viscosity of the fluid. Core-shell droplets were generated when two phases met with a fluorinated carbon oil at a cross-junction. The outermost acidic oil phase crosslinked the alginate, resulting in the formation of core-shell spheroids[96].

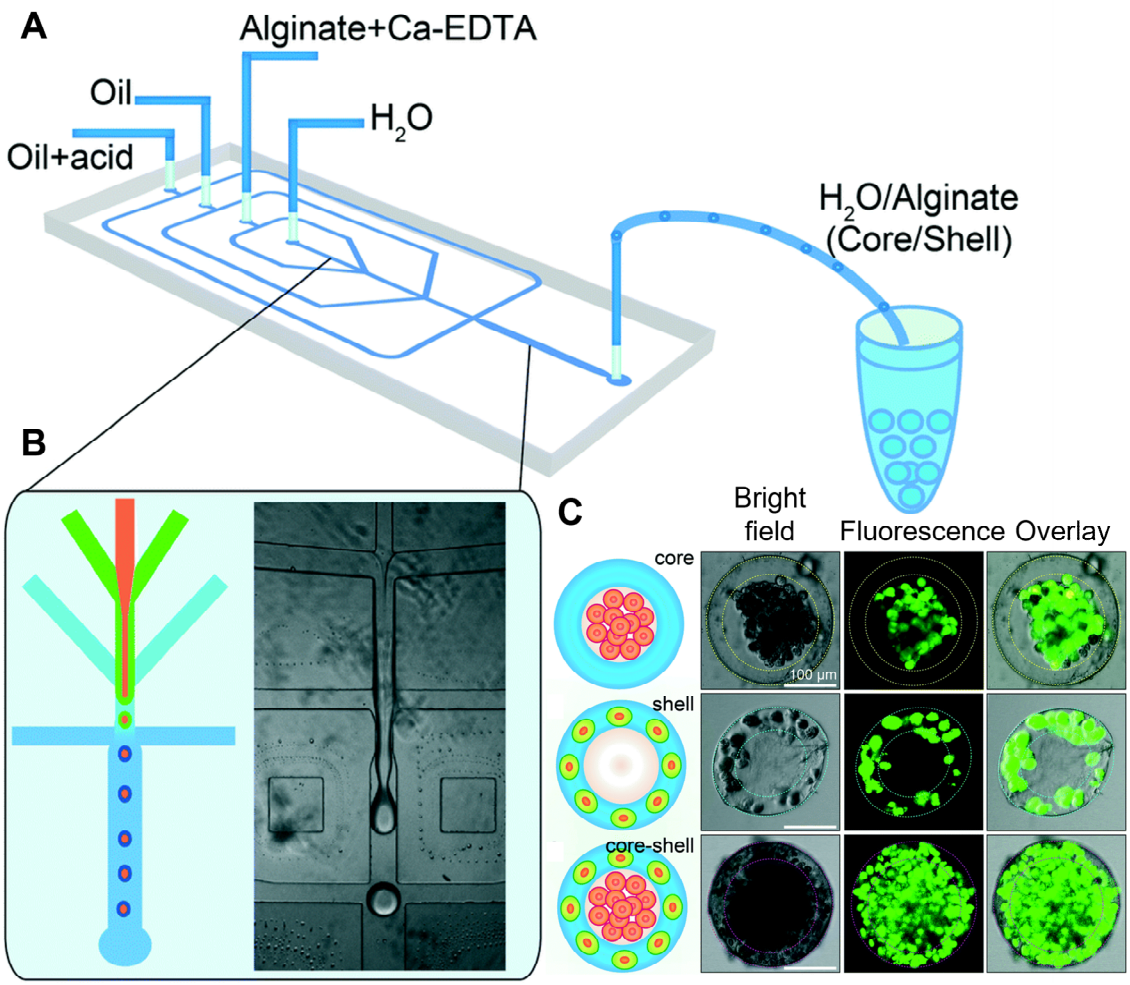


Figure 1.9. Schematic illustration of the fabrication of core-shell structure spheroids. (A) Schematic diagram of the microfluidic device. (B) Fabrication of core-shell spheroids using w/w/o (w: water; o: oil) double emulsions. (C) Spatial assembly of different cells in the 3D core-shell spheroid. The core was composed of HepG2 cells, while the shell was composed of NIH-3T3 fibroblasts. Scale bars = 100 μm. Reprinted from Chen et al.[96].

In addition to generating 3D spheroids, microfluidic systems can also be utilised for therapeutic evaluation. Chen et al. developed a breast-cancer-on-a-

chip model that integrated tumour spheroid formation and drug evaluation within a single device (**Figure 1.10**). They synthesised a drug delivery system based on carbon dots, which was capable of penetrating monolayer endothelium and demonstrated non-toxic to cells. This system allowed for the evaluation of drug delivery effectiveness in situ and in real-time[97].

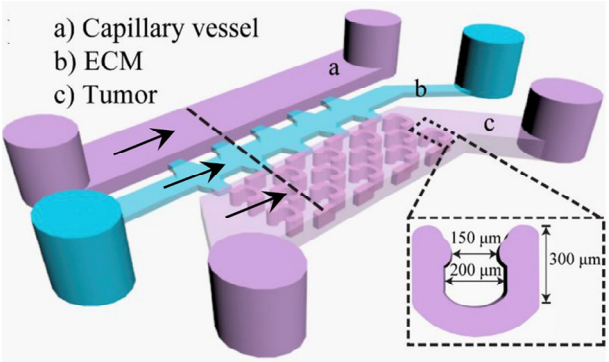


Figure 1.10. Schematic illustration of a microfluidic platform for therapeutic evaluation. The microfluidic platform comprised of three microchannels, representing a capillary vessel for therapeutic delivering, the ECM, and 3D tumour spheroids, respectively. Insert: A U-shaped microchamber for tumour spheroid formation. Reprinted from Chen et al.[97].

Cancer malignancy is always associated with metastasis, a process in which cancer cells disperse from their primary location and develop tumours at distant sites. Microfluidic systems have been adopted to investigate different stages of metastasis, including angiogenesis, migration, intravasation and extravasation[92]. As an example, a three-channel microfluidic chip was designed to study the extravasation of breast cancer cells (**Figure 1.11**). The chambers situated between channels were filled with collagen hydrogel to simulate the ECM, and endothelial cells were introduced into the middle channel to mimic a vessel wall. After one day of seeding breast cancer cells, they were observed to transmigrate across endothelium from the channel into the hydrogel, which also led to an increase in endothelial permeability[98].

Specifically, in the context of ovarian cancer, accumulation of ascites fluid has been proved to be a critical factor associated with patient prognosis[99, 100]. Utilising a microfluidic system enables the emulation of ascites fluid flow, facilitating the investigation of its hydrodynamic effects on ovarian cancer metastasis in the peritoneum[101]. A potential future direction is to integrate multiple organ chips, such as liver, brain, and breast chips, and implement circular fluid flows to explore systemic metastasis comprehensively[102].

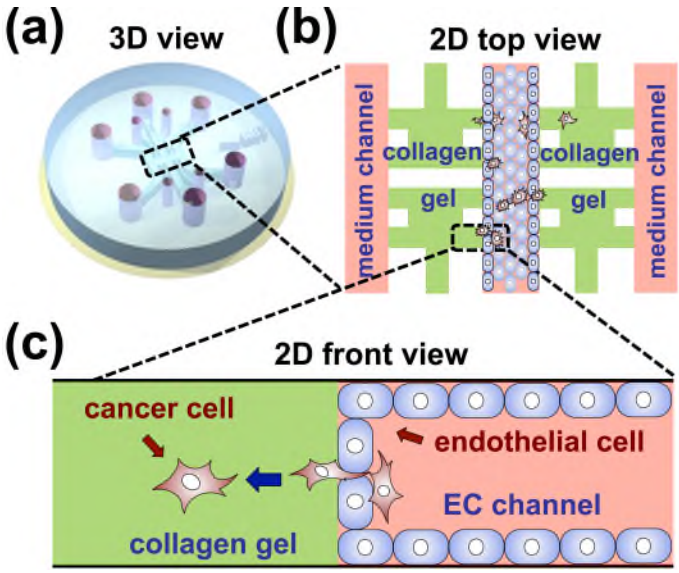


Figure 1.11. Schematic illustration of tumour extravasation modelled by a microfluidic system. General view (a) and inside view (b) of the microfluidic system. (c) Extravasation of cancer cells into collagen hydrogel. Reprinted from Jeon et al.[98].

Collectively, microfluidics represents a promising solution for addressing various unmet needs in the realms of 3D cell culture and cancer research. Microfluidics serves not only as a tool for creating 3D cell models but also as a platform for simulating more *in vivo*-like environments, shedding light on interactions among different organs. The dynamic perfusion within microfluidic systems replicates the bloodstream, a critical factor that is challenging to

reproduce with other techniques[97]. As this technology continues to advance, *in vitro* systems can increasingly resemble *in vivo* tumours, fostering a deeper understanding of the complexity of cancer.

1.6 Summary of thesis work

This thesis aims to (1) implement microfluidic techniques to create scaffold-based 3D microtumours, and (2) utilise these 3D microtumours for modelling ovarian cancer and conducting therapeutics testing.

In Chapter 2, meticulous adjustments were made to the parameters of the microfluidic system to effectively handle viscous pre-gel solutions, resulting in the production of 3D microtumours. Appropriate characterisation methods were examined and optimised for these microtumours. Once the microfluidic platform was fine-tuned, we were able to create 3D microtumours with customisable size, morphology, and hydrogel selection in a high-throughput manner.

In Chapter 3, focusing on ovarian cancer, we characterised these 3D microtumours in terms of key physiological features, including the presence of hypoxic cores, the arrangement of cytoskeletons, and their responses to therapeutic agents.

In Chapter 4, the 3D microtumours were utilised to model ovarian cancer MRD and to identify therapeutics that specifically target MRD without affecting bulk ovarian cancer cells.

Finally, in Chapter 5, we comprehensively summarise the key findings and outcomes presented in this thesis and provide an overview of potential directions for future research, such as technical improvements and medical applications.

2 Microfluidic techniques for 3D microtumours fabrication

2.1 Introduction

The microfluidic technique has gained popularity in diverse applications, including developing organ chips for simulating physiological processes[102], mimicking blood circulation for the study of cancer metastasis[103], and aiding in cancer diagnosis[104] in both 2D and 3D cell cultures. Microfluidics has primarily been used as a platform for culture and analysis of cells, and growing works have reported the direct implementation of microfluidics in the fabrication of 3D cell constructs[105]. Leveraging the advantages of high throughput and the ability to produce uniformly sized microdroplets, we utilised the microfluidic system to efficiently manufacture 3D microtumours with consistent dimensions and compositions. This approach allowed us to generate 3D microtumours by using various cell types and hydrogel options, which overcomes the strict viscosity requirements typically associated with 3D cell spheroids fabricated through bioprinting methods.

Characterizing 3D microtumours poses several challenges, including: (1) the fact that many commercially available cell assays are designed for use with 2D monolayer cultures, potentially leading to difficulties in the penetration of assay molecules into 3D structures; (2) imaging large-sized 3D spheroids can be problematic due to light scattering and the limited light penetrating depth through thick samples. To address these challenges, we explored various cell assays that

might be suitable for use with 3D microtumours, identified those that could be adapted for our system, and optimised the associated protocols accordingly.

Acknowledgement of collaboration

The computer-aided design and 3D printing of the custom-made reverse mould, and preparation of silk fibroin hydrogels were finished with the help of Dr Yujia Zhang from Prof Hagan Bayley laboratory (Department of Chemistry, University of Oxford).

2.2 Fabrication of 3D microtumours by using the microfluidic platform

3D microtumours, tumour cells encapsulated in biocompatible hydrogels, were created using a surfactant-free, droplet-based microfluidic platform, which was improved over work previously reported by our group[106]. The microfluidic platform consists of three main compartments: (1) two syringes controlled separately by microfluidic pumps; (2) a 3-channel PDMS microfluidic chip; and (3) a polytetrafluoroethylene (PTFE) exit tube.

In general, cell-hydrogel suspension and oil were loaded into two separate syringes and pumped into the PDMS microfluidic chip, in which the two immiscible liquids met and produced 3D microtumours separated by oil (**Figure 2.1**). The 3D microtumours were temporarily stored in the PTFE exit tube until complete gelation of the hydrogel, and then transferred to a medium-containing culture plate (more details in Section 6.3).

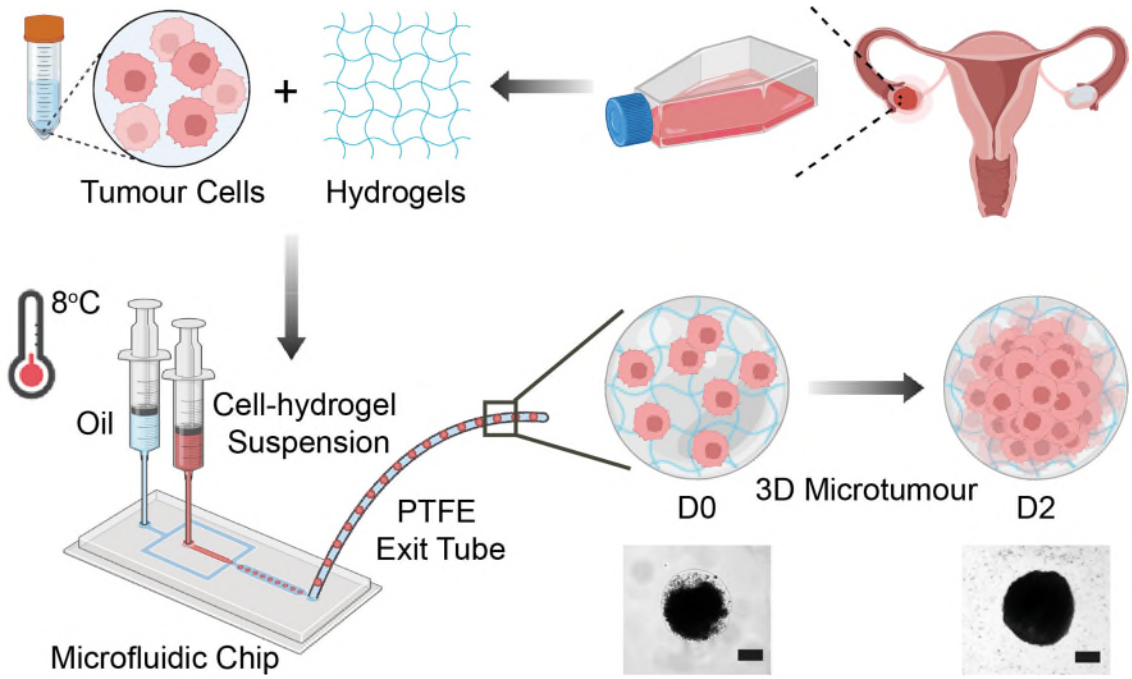


Figure 2.1. Schematic illustration of the fabrication process of 3D microtumours by using the microfluidic platform. 2D monolayer cells were harvested and mixed with hydrogel to form a suspension. The cell-hydrogel suspension and tetradecane oil were pumped into a PDMS microfluidic chip at 8°C by microfluidic pumps. At least one hundred 3D microtumours separated by oil were generated within 3 minutes and temporarily stored in a PTFE exit tube. Upon complete gelation at 37°C, the 3D microtumours were transferred from the PTFE tube to a medium-containing culture plate. Inset: Brightfield microscope images of 3D microtumours composed of OVCAR-5/RFP ovarian cancer cells and Matrigel on D0 and D2 after fabrication. Scale bar = 300 µm. The diagrams were created with BioRender.com.

To successfully produce 3D microtumours, the microfluidic platform, tube inner diameters (ID), material choices, fabrication temperatures, and incubation times needed to be optimised. The following chapter shows the effects of each parameter and the optimal conditions for fabrication.

2.2.1 Hydrogels

The suspension was formed by mixing cell pellets with pre-gel solution of biocompatible hydrogels. Hydrogels are crosslinked polymer networks with high water contents of more than 95%[107]. Their similar biological properties to

extracellular matrix (ECM), and tuneable mechanical and chemical properties guarantee the utilisation of hydrogels as scaffolds for 3D cell culture[108]. Among the broad spectrum of hydrogels, we examined the most commonly used ones derived from biological sources with our microfluidic platform, including Matrigel, collagen, agarose and silk fibroin.

Matrigel, first reported in the mid-1980s, is a solubilized basement membrane proteins derived from a ECM-rich tumour, the Engelbreth-Holm-Swarm (EHS) mouse sarcoma[109]. The major components of Matrigel include laminins, collagen IV, heparan sulfate proteoglycan, and a number of growth factors[110]. Although it has been cautioned that growth factors in Matrigel may affect cellular activity[111], Matrigel is still well-acknowledged to be a powerful substrate for 3D cell culture supporting differentiation, development, drug screening, and disease modelling[109].

Collagen is an abundant and essential biopolymer in ECM[112]. As a natural polymer, it provides excellent cell binding and support of motility[113], and has been applied in cell culture, such as epithelial cells[114], myogenic cells[115] and fibroblasts[116].

Agarose, extracted from red algae, is a natural hydrogel comprised of linear polysaccharides and exhibits a thermo-reversible gelation behaviour[117]. However, it lacks cell adhesiveness and is a commonly used biomaterial to investigate cell adhesion and cell migration[118, 119].

Silk fibroin is a natural fibre primarily produced by spiders and silkworms. It is considered a promising biomaterial with applications in bone regeneration and cardiac tissue regeneration. Additionally, silk fibroin has been shown to support the differentiation of mesenchymal stem cells[120-122].

The OVCAR8 ovarian cancer cells were suspended in pre-gel solutions of these four hydrogels for microfluidic fabrication. 3D microtumours made of Matrigel, collagen, agarose and silk fibroin were successfully fabricated by using our microfluidic platform (**Figure 2.2**).

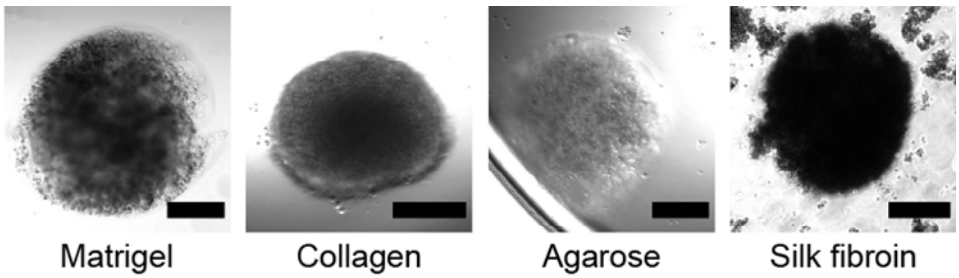


Figure 2.2. 3D microtumours composed of OVCAR8 and different hydrogels. Brightfield microscope images for Matrigel, collagen, agarose and silk fibroin microtumours were taken on D0 after fabrication. Scale bars = 300 μm.

All the four hydrogels used here are thermo-sensitive and polymerise at specific temperature ranges. During microfluidic fabrication, the pre-gel solutions should maintain at liquid format. Temperature fluctuations can trigger premature polymerisation, alter the viscosity of cell-hydrogel suspensions, and consequently impact fluid flow profiles, leading to variations in the formation of 3D microtumours. Therefore, maintaining stable temperature control during microfluidic fabrication is crucial.

For Matrigel, collagen and silk fibroin, the microfluidic fabrication should be conducted at 8°C and the gelation happens at 37°C. To enable low temperature fabrication, the entire microfluidic platform was situated in a fridge. The microfluidic pumps were initiated once the temperature had stabilized, allowing for precise control over the temperature during the microfluidic process.

In the case of agarose, which exhibits different temperature characteristics compared to the other three hydrogels, a unique approach was employed.

Microfluidic fabrication was carried out at 37°C, followed by gelation at 4°C. To achieve this, an infrared heater was utilised to regulate the temperature of the syringes and PTFE tubes, maintaining them at approximately 37°C during the microfluidic fabrication process. Subsequently, the temperature was lowered to around 4°C to facilitate gelation.

The gelation time dependents on the type of hydrogel used, and the optimal time for each hydrogel was assessed and summarised in **Table 2.1**. To be noted, since Matrigel suffers from batch-to-batch variation, the gelation time may variate from 1.5 to 2 hours. With sufficient gelation time, the 3D microtumours maintain their structural integrity, the same shape as they were fabricated and temporarily stored in the PTFE tubes. However, inadequate gelation time can lead to structural damage or even disintegration of 3D microtumours when they are ejected from the PTFE tubes (**Figure 2.3**). Given that Matrigel is strongly recommended for 3D cell culture of epithelial cancer (Section 1.4.2.2), all subsequent experiments were performed using Matrigel as the matrix unless otherwise specified.

Table 2.1. Summary of biocompatible hydrogels and their preparation conditions used in 3D microtumour fabrication.

Hydrogels	Preparation for cell-hydrogel suspension	Microfluidic fabrication temperature	Post-fabrication process temperature	Gelation time
Matrigel	Thaw completely on ice, then mix with cells on ice.	8°C	37°C	2 hours
Collagen	Thaw completely on ice, then mix with cells on ice.	8°C	37°C	1.5 hours
Agarose	Melt at 70°C and cool to 37°C, then mix with cells at 37°C.	37°C	4°C	10 minutes
Silk fibroin	Thaw completely at 4°C, then mix with cells on ice.	8°C	37°C	30 minutes

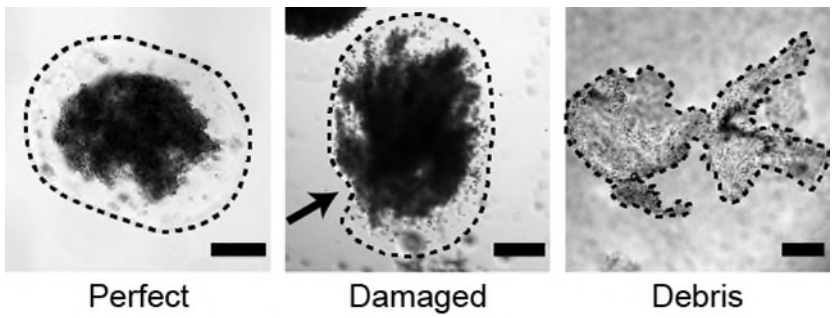


Figure 2.3. Brightfield microscope images of 3D microtumours of various gelation time. The 3D microtumours composed of OVCAR8 and Matrigel. Sufficient gelation time (2 h) resulted in perfect shape of 3D microtumours after ejection from the PTFE tube, while insufficient gelation time (1 hour) resulted in damaged structure or even debris of 3D microtumours. The dashed black lines show the contours of the structures. Scale bar = 300 μm.

2.2.2 Cell types

After confirming the compatibility of various hydrogels with the microfluidic platform, we also assessed whether our platform could be used with different cell types. We successfully fabricated 3D microtumours using a wide range of cell lines, including both cancer cell lines (OVCAR5, OVCAR8, Kuramochi, MDA-MB-231, HeLa) and normal tissue cell lines (fibroblasts, adipocytes, embryonic kidney cells) (**Table 2.2**). These cells proliferated within the 3D structures and

increased in density by D2 (**Figure 2.1**). These results demonstrate the versatility and effectiveness of the microfluidic platform for creating 3D cell constructs, highlighting that it is not limited to specific cell types or hydrogel types.

Table 2.2. Summary of cells used in 3D microtumour fabrication.

Cell line	Classification	Source	Catalogue No.
OVCAR-5/RFP[a]	Ovarian cancer	Human	Cell Biolabs Inc. AKR-254
OVCAR5	Ovarian cancer	Human	ATCC[c]
OVCAR8	Ovarian cancer	Human	ATCC
Kuramochi	Ovarian cancer	Human	JCRB CVCL_1345
MDA-MB-231	Breast cancer	Human	Cell Biolabs Inc. AKR-251
HeLa/GFP[b]	Cervical carcinoma	Human	Cell Biolabs Inc. AKR-213
NIH3T3/GFP	Fibroblast	Mouse	Cell Biolabs Inc. AKR-214
3T3-L1 derived adipocytes	Fat cell	Mouse	ATCC CL-173
HEK293T	Embryonic kidney	Human	ATCC CRL-3216

[a]RFP: red fluorescence protein.
[b]GFP: green fluorescence protein.
[c]ATCC: American Type Culture Collection

2.2.3 Cell density and oil

During our experimentation with different components in cell-hydrogel suspension preparation, we discovered that cell density played a crucial role in two important aspects.

Firstly, the oil that separated the 3D microtumours during microfluidic fabrication needed to be eliminated through phase transfer once the hydrogels had fully gelated. To achieve this, the 3D microtumours were ejected from the PTFE tubes into cell culture medium and subjected to multiple washes to ensure

the thorough removal of the oil. The oil density had a notable impact on the efficiency of this phase separation process.

We conducted experiments with various oils, including undecane, tetradecane, silicone oil, and sunflower oil. While all of these oils could be adapted for use in the microfluidic platform to create 3D microtumours, separating the microtumours from silicone oil or sunflower oil posed challenges due to their similar densities compared to the cell culture medium (**Table 2.3**). In contrast, undecane and tetradecane exhibited a distinct difference in density compared to the cell culture medium. Tetradecane, in particular, with its longer hydrocarbon chain containing 14 carbons, displayed greater hydrophobicity than undecane, which contains 11 carbons in its backbone. This greater hydrophobicity made tetradecane easier to separate from the aqueous phase. Furthermore, it has been reported that cell viability remained above 90% when cells were exposed to tetradecane for up to 6 hours, demonstrating the biocompatibility of tetradecane[123]. Therefore, we chose tetradecane as the preferred oil for the fabrication of 3D microtumours.

Table 2.3. Density of oil or cell culture medium used in phase separation.

Classification	Fluids	Density (g mL^{-1})
Oil	Undecane	0.74
	Tetradecane	0.762
	Silicone oil	1.000-1.020
	Sunflower oil	0.919[124]
Cell culture medium	DMEM[a] (high glucose)	1.000[125]
	DMEM (high glucose) with 20% FBS[b]	1.023[125]

[a]DMEM: Dulbecco's modified Eagle's medium
[b]FBS: Fetal bovine serum

During the phase transfer process, 3D microtumours suspended in tetradecane oil were combined with cell culture medium in a Falcon tube. To ensure the integrity of the microtumours, the mixture was gently pipetted up and down several times. Within a few seconds, a distinct boundary became visible between the tetradecane (upper layer) and the 3D microtumours in the cell culture medium (lower layer). 3D microtumours created from cell-hydrogel suspensions with high cell density quickly settled at the bottom of the Falcon tubes. In contrast, those formed from low cell density cell-hydrogel suspensions remained at the boundary between the tetradecane and cell culture medium, resulting in ineffective separation of the 3D microtumours from the oil.

Secondly, cell density affects cell proliferation within 3D microtumours. Cell-hydrogel suspensions of various cell density (1, 2, and 3×10^7 cells mL^{-1}) were used for 3D microtumours preparation. Brightfield microscope images taken on D1, D2 and D5 allowed us to monitor cell proliferation within these microtumours. In cases of low cell density, limited cell growth was observed in the 3D microtumours, and even on D5 post-fabrication, the cells did not fully occupy the entire structure (**Figure 2.4**). Anoikis, a programmed cell death process, can be induced when cells are distant from each other and lose contact with neighbouring cells[126]. Conversely, higher cell density 3D microtumours (3×10^7 cells mL^{-1}) exhibited more noticeable cell proliferation, with cells filling the entire structure.

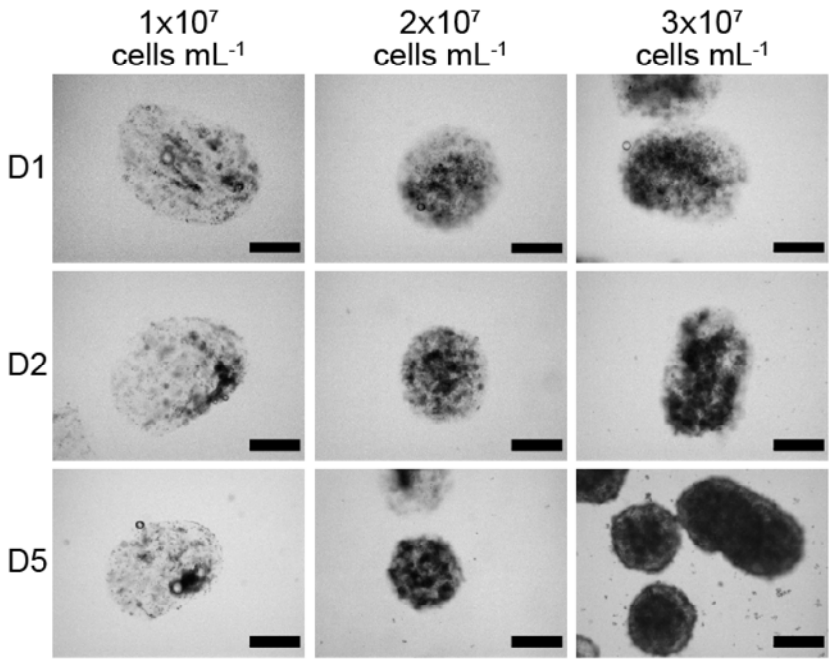


Figure 2.4. 3D microtumours prepared with cell-hydrogel suspensions of various cell densities. Brightfield microscope images were taken on D1, D2 and D5 after fabrication. Area occupied by the cells appeared in black colour. Scale bar = 500 µm.

Therefore, using suspensions with a high cell density is beneficial not only for the extraction of 3D microtumours from the oil after microfluidic fabrication, but also for promoting cell proliferation within the microtumours and preventing anoikis.

2.2.4 Flow rates and shape

Creating 3D microtumours of different shapes has traditionally been challenging using existing fabrication methods like hanging drop, forced aggregation, and spinner culture. However, the microfluidic platform offers the convenience of fabricating 3D microtumours in various shapes, such as spheres, ellipsoids, and rods, by adjusting the flow rate ratios between the cell-hydrogel suspension and oil (**Figure 2.5**). Additionally, we observed that as long as the flow rate ratio remained constant, the shape of the microtumours remained

consistent. For instance, setting the cell-hydrogel suspension:oil flow rates to 1000:3000 and 2000:6000 µL h^{-1} both resulted in spherical shapes.

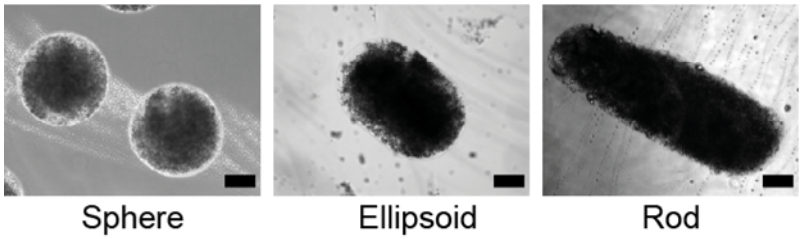


Figure 2.5. 3D microtumours of various shapes. Brightfield microscope images were taken on D0 after fabrication. The shapes of sphere, ellipsoid and rod were achieved by adjusting the cell-hydrogel suspension:oil flow rate ratio to 1000:3000, 1000:1000, and 1000:300 µL h^{-1}, respectively. Scale bar = 300 µm.

2.2.5 Size

The size of in vitro 3D cell culture models is a crucial parameter when aiming to mimic in vivo tumours effectively. Tumours that grow larger than 400-500 µm, often develop hypoxia due to insufficient oxygen and nutrient levels reaching the centre of the tumour[127, 128]. Hypoxia, in turn, activates transcription factors that promote angiogenesis and metastasis of tumours[26, 27]. Therefore, small-sized microtumours are inadequate for replicating these characteristics, making them suboptimal for cancer research.

The microfluidic platform offers flexibility in adjusting the size of 3D microtumours, which is hard to achieve with other fabrication methods. By simply using PTFE exit tubes with different ID and microfluidic chips with matched channel sizes, we managed to fabricate 3D microtumours of small, medium and large size (**Figure 2.6**).

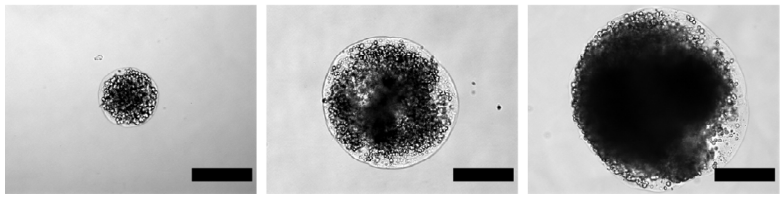


Figure 2.6. 3D microtumours of various sizes. Brightfield microscope images were taken on D0 after fabrication. 3D microtumours were generated with PTFE exit tubes of ID = 300, 650 and 900 µm. Scale bar = 300 µm.

The channel size of microfluidic chips must be compatible with the ID of the PTFE exit tubes to ensure that the 3D microtumours maintain their dimensions when entering the exit tubes (**Figure 2.7**). For instance, spheres formed in a channel with an 800 µm diameter could be reshaped into long rods when squeezed into a PTFE exit tube with an ID of 300 µm. To provide more options for channel sizes compared to the previous method of drilling holes in PDMS blocks to create the T-junction[106], we improved the manufacturing process of PDMS microfluidic chips. These chips were fabricated by casting PDMS on a custom-made reverse mould, which was produced using a 3D printer and clear resin. The channel size is determined by computer-aided design files used for 3D printing, and the printing resolution can reach 25 µm.

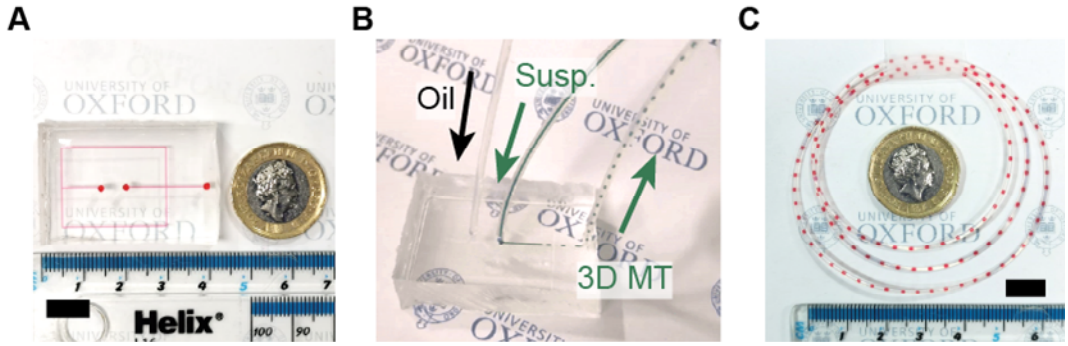


Figure 2.7. Microfluidic chips and 3D microtumours in a PTFE exit tube. (A) Image of a 3-channel PDMS microfluidic chip with channel size of 300 µm. (B) Image showing the microfluidic fabrication process. Cell-hydrogel suspension (Susp.) was stained with green dye. 3D microtumour was labelled as 3D MT. PTFE tube of ID 300 µm were used. (C) Image of 3D microtumours (stained with red dye) in a PTFE exit tube. Scale bars =1 cm.

2.3 Characterisation for 3D microtumours

2.3.1 Cell assays

After optimising the microfluidic platform for 3D microtumours fabrication, the next step was to determine the appropriate characterization methods for the microtumours produced. To assess whether the microfluidic fabrication process caused any damage to the cells, various properties of the 3D microtumours could be measured, including apoptosis, cytotoxicity, and viability. Five commercially available cell assays, which claimed to be suitable for 3D microtissue cultures, were tested to determine their adaptability to the 3D microtumours. These five cell assays included: 1) Caspase-Glo 3/7 Assay; 2) CellTox Green Cytotoxicity Assay; 3) RealTime-Glo MT Cell Viability Assay; 4) CellTiter-Glo 3D Cell Viability Assay; 5) PrestoBlue Cell Viability Assay.

2.3.1.1 Caspase-Glo 3/7 Assay

The Caspase-Glo 3/7 Assay measures the activity of caspase 3/7, which are biomarkers of apoptosis, a programmed cell death process[129]. Caspase cleavage

of a luminogenic substrate generates a luminescence signal, which is proportional to the amount of caspase present.

In this study, 3D microtumours composed of OVCAR-5/RFP ovarian cancer cells were treated with carboplatin (10 µM) for 4 days to induce apoptosis, with the untreated microtumours of identical population of cells serving as the negative control. After the treatment, Caspase-Glo 3/7 Assay reagents were added to the 3D microtumours, and the luminescence signal was recorded. A linear correlation between cell number and luminescence signal was expected, but this was not observed (**Figure 2.8**).

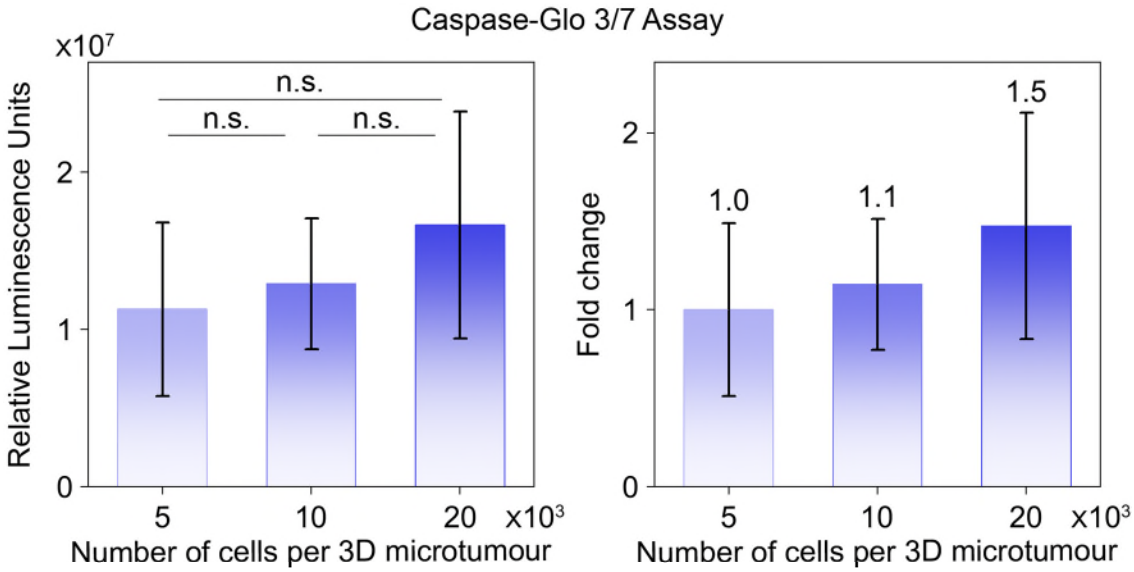


Figure 2.8. Caspase-Glo 3/7 Assay to monitor apoptosis in 3D microtumours. 3D microtumours (diameter 900 µm) made of OVCAR-5/RFP ovarian cancer cells with different cell density were treated with carboplatin (10 µM) for 4 days to induce apoptosis (n = 3). Left: relative luminescence units (RLU) readouts were taken 2 hours after adding assay reagents. Right: fold change of RLU over the 3D microtumours containing 5000 cells. Significance was tested using a Tukey test. n.s.: not significant, P > 0.5.

Unlike in 2D monolayer cultures, where apoptosis can be simultaneously induced in all cells upon drug exposure, the penetration of drugs into 3D microtumours may trigger apoptosis at various times. It is important to note that

caspase degrades rapidly once activated[130]. Consequently, the level of caspase measured at a specific time may not accurately represent the total number of apoptotic cells within 3D microtumours. Hence, the Caspase-Glo 3/7 Assay may not be suitable for use with the 3D microtumours in this work.

2.3.1.2 CellTox Green Cytotoxicity Assay

The CellTox Green Cytotoxicity Assay measures the number of dead cells. A high fluorescence signal is released when the cyanine dye binds to DNA from cells with impaired cell membranes. For viable cells with intact cell membranes, the dye cannot penetrate into the cells, resulting in a low fluorescence signal.

In this study, 3D microtumours composed of OVCAR-5/RFP ovarian cancer cells were treated with carboplatin (10 μM) for 4 days to induce cell death. After the treatment, CellTox Green dye was added to the 3D microtumours, and the fluorescence signal was recorded. A linear correlation between the number of dead cells and fluorescence signal was expected, but this was not observed (**Figure 2.9**).

The failure may derive from the overlap of emission wavelengths of the CellTox Green dye (520-530 nm) with excitation wavelengths of OVCAR-5/RFP cells, which can be excited by laser at 488 nm or 532 nm. As a result, the CellTox Green Cytotoxicity Assay was not suitable for use with the 3D microtumours in this study.

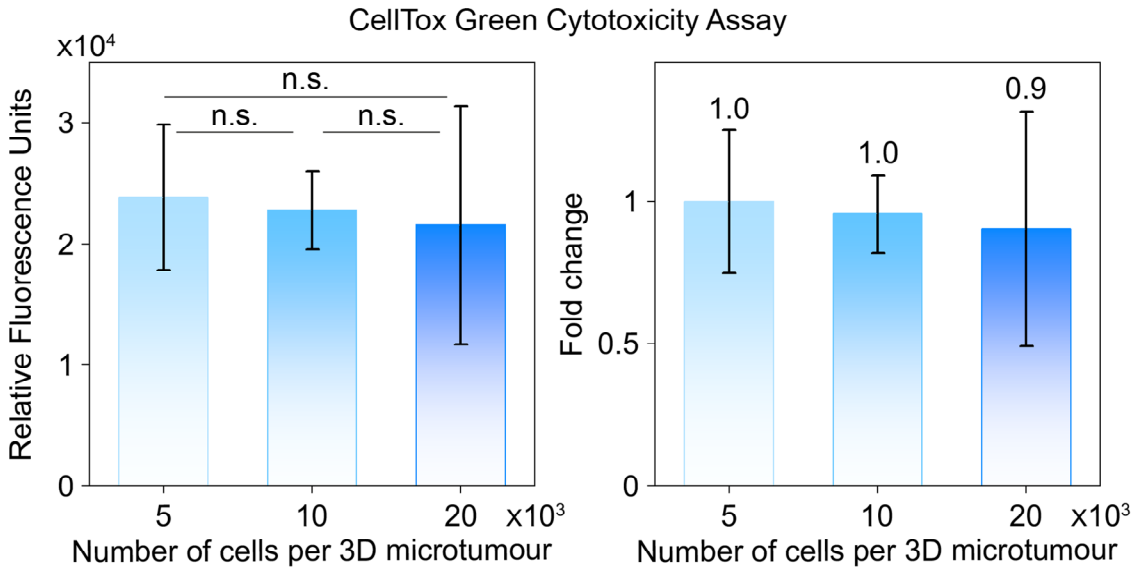


Figure 2.9. CellTox Green Cytotoxicity Assay to quantify dead cells in 3D microtumours. 3D microtumours (diameter 900 µm) made of OVCAR-5/RFP ovarian cancer cells with different cell density were treated with carboplatin (10 µM) for 4 days to induce cell death (n = 3). Left: relative fluorescence units (RFU) readouts were taken 2 hours after adding assay reagents. Right: fold change of RFU over the 3D microtumours containing 5000 cells. Significance was tested using a Tukey test. n.s.: not significant, P > 0.5.

2.3.1.3 RealTime-Glo MT Cell Viability Assay

The RealTime-Glo MT Cell Viability Assay measures the number of viable cells. The metabolism (MT) cell viability substrates can be reduced by viable cells, activating luciferases to produce luminescence signals. In contrast, dead cells, which are metabolically inactive, fail to reduce the substrates, resulting in the absence of luminescence signals.

In this study, RealTime-Glo reagent was added to 3D microtumours composed of OVCAR-5/RFP ovarian cancer cells, and the luminescence signal was recorded. A linear correlation between cell number and luminescence signal was expected, but this was not observed (**Figure 2.10**). Over the time course of 72 hours, the luminescence signal initially increased and then decreased with time, but no proportionality was observed between cell number and luminescence. The penetration of reagents into 3D microtumours may introduce

inaccuracies in assessing viable cell numbers using the assay. Once again, the RealTime-Glo MT Cell Viability Assay may not be suitable for use with the 3D microtumours in this work.

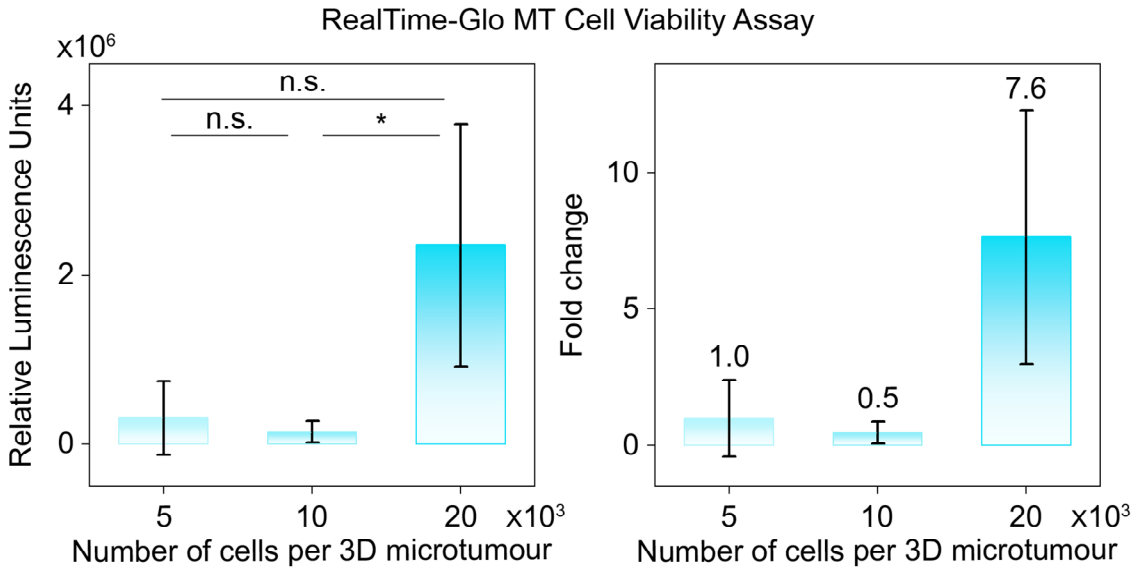


Figure 2.10. RealTime-Glo MT Cell Viability Assay to quantify viable cells in 3D microtumours. 3D microtumours (diameter 900 µm) were made of OVCAR-5/RFP ovarian cancer cells with different cell density (n = 3). Left: RLU readouts were taken 2 hours after adding assay reagents. Right: fold change of RLU over the 3D microtumours containing 5000 cells. Significance was tested using a Tukey test. *P < 0.05, n.s.: not significant, P > 0.5.

2.3.1.4 CellTiter-Glo 3D Cell Viability Assay

The CellTiter-Glo 3D Cell Viability Assay quantifies the viable cells. CellTiter-Glo 3D Reagent can induce cell lysis and release adenosine triphosphate (ATP) from metabolically active cells. The luciferins react with ATP to generate a luminescence signal, which is directly proportional to the number of viable cells[131].

In this study, CellTiter-Glo 3D Reagent was added to 3D microtumours composed of OVCAR-5/RFP ovarian cancer cells, and the luminescence signal was recorded. A linear correlation between cell number and luminescence signal was expected, but this was not observed (**Figure 2.11**). Further, the results

showed large variations among replicates. Although this assay reagent is formulated for 3D cell culture, the penetration of the reagent into the centre of 3D cell constructs, which depends on the size and compactness of the construct, is a significant factor that can affect assay performance. The assay results provided by the manufacturer for 3D cell culture were based on spheroids with a diameter of 350 µm or less. In this study, 3D microtumours with a diameter above 900 µm were used. Less effective reagent penetration may be the reason for the failure of the CellTiter-Glo 3D Reagent in this context.

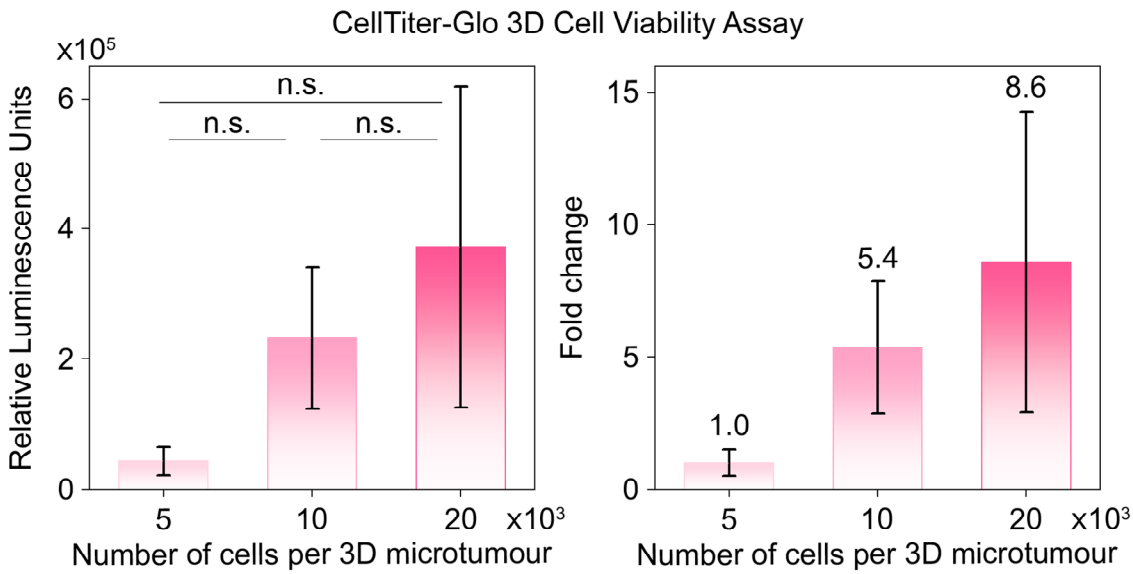


Figure 2.11. CellTiter-Glo 3D Cell Viability Assay to quantify viable cells in 3D microtumours. 3D microtumours (diameter 900 µm) were made of OVCAR-5/RFP ovarian cancer cells with different cell density (n = 3). Left: RLU readouts were taken 1 hour after adding assay reagents. Right: fold change of RLU over the value for 3D microtumours containing 5000 cells. Significance was tested using a Tukey test. n.s.: not significant, P > 0.5.

2.3.1.5 PrestoBlue Cell Viability Assay

The PrestoBlue Cell Viability Assay quantifies viable cells. PrestoBlue reagent is a cell-permeant dye based on resazurin. It can be reduced by viable

cells, resulting in a colour change from blue to red and generating a high fluorescence signal, which is directly proportional to the number of viable cells[132].

In this study, PrestoBlue Reagent was added to 3D microtumours composed of OVCAR-5/RFP ovarian cancer cells, and the fluorescence signal was recorded. Consistent with expectation, a linear correlation between cell number and fluorescence signal was observed (**Figure 2.12**). When the cell number doubled, the fluorescence also increased twice in intensity.

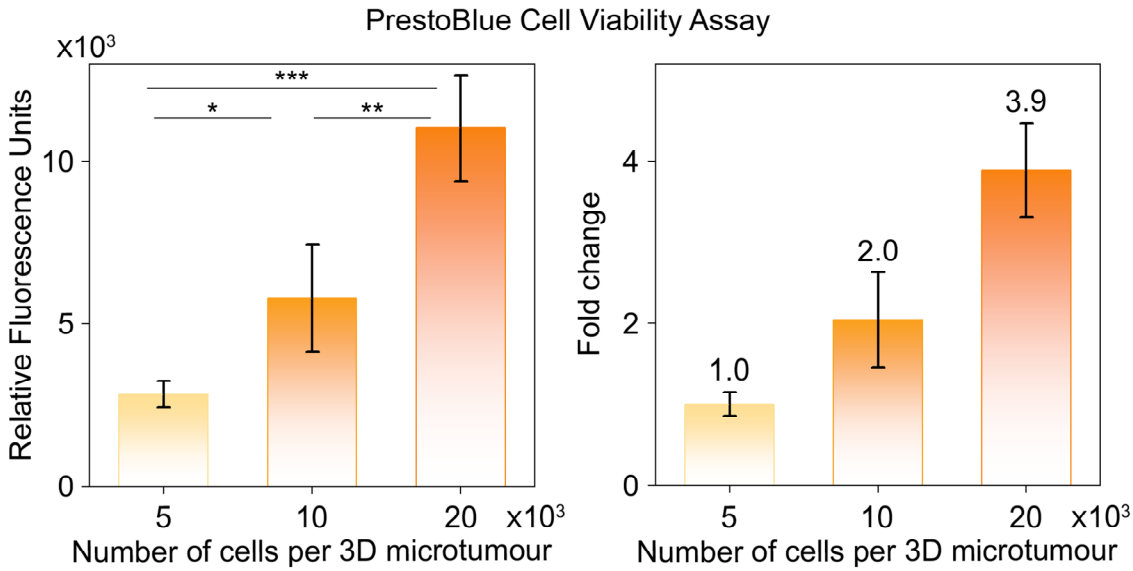


Figure 2.12. PrestoBlue Cell Viability Assay to quantify viable cells in 3D microtumours. 3D microtumours (diameter 900 µm) were made of OVCAR-5/RFP ovarian cancer cells with different cell density (n = 3). Left: RFU readouts were taken 2 hours after adding assay reagents. Right: fold change of RFU over the 3D microtumours containing 5000 cells. Significance was tested using a Tukey test. ***P < 0.001, **P < 0.01, *P < 0.05.

Further experiments were conducted to confirm the range of linear correlation between RFU and cell number. OVCAR-5/RFP cells with cell number from 0 to 32,000 per 3D microtumour or per well in 2D monolayer were incubated with PrestoBlue Reagent for 1 hour. The results confirmed a linear correlation

between fluorescence and cell number within the range of 0-32,000 cell for both 3D (R^2 = 0.96) and 2D cultures (R^2 = 0.94) (**Figure 2.13**).

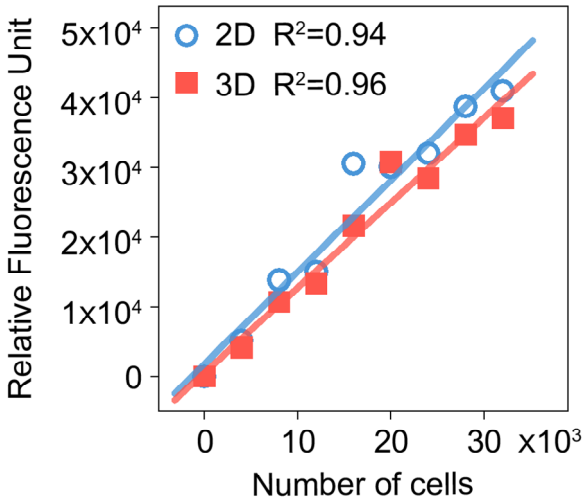


Figure 2.13. Range of linear correlation between fluorescence and cell number for PrestoBlue Cell Viability Assay. OVCAR-5/RFP cells with cell number from 0 to 32,000 in the format of either 3D microtumour or 2D monolayer were incubated with PrestoBlue Reagent at 37°C and 5% CO_2 for 1 hour.

Finally, we identified an assay that can be effectively adapted to the 3D microtumours in this work. The PrestoBlue Reagent is used to evaluate viability for the remaining of this thesis.

2.3.2 Cell viability during microfluidic fabrication

To determine whether the microfluidic fabrication process had any detrimental effects on the cells, a viability assay was conducted at three stages of microfluidic fabrication: 2D cells harvested from culture flasks, cell-hydrogel suspensions, and 3D microtumours after microfluidic fabrication. Cells are delicate, and their viability can be compromised either by apoptosis or mechanical damage when subjected to intense hydrodynamic forces[133, 134]. High cell viability was consistently maintained with various cell types (**Figure 2.14A**)

and different hydrogels (**Figure 2.14B**, **Table 2.4**). Cell viabilities of over 90% were consistently achieved, with no significant differences observed among all the three stages, demonstrating that the microfluidic fabrication process does not harm the cells.

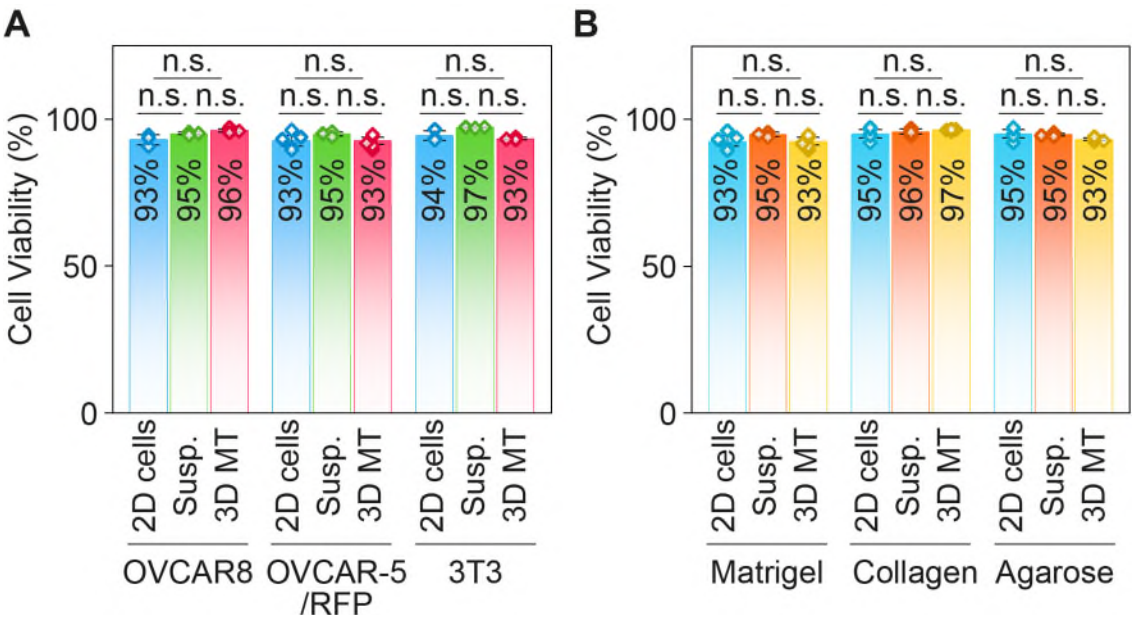


Figure 2.14. Cell viability at three stages of microfluidic fabrication. The three stages are: 2D cells harvested from flasks, cell-hydrogel suspension (Susp.), and 3D microtumours after microfluidic fabrication (3D MT). Top: Matrigel with three cell lines, OVCAR8, OVCAR-5/RFP and 3T3 fibroblasts. Bottom: OVCAR8 cells with three hydrogels, Matrigel, collagen and agarose. n = 3 to 6. Significance was tested using a Tukey test. n.s.: not significant, P > 0.05.

Table 2.4. Cell viability data at three stages of the microfluidic fabrication. 3D microtumours were made from various cells and hydrogels (n = 3 to 6).

Cell	Hydrogel	Cell viability		
		2D cells*	Cell-hydrogel suspension	3D microtumours
OVCAR8	Matrigel	93% ± 2.0%	95% ± 0.58%	96% ± 0.74%
OVCAR-5/RFP	Matrigel	93% ± 2.7%	95% ± 0.85%	93% ± 2.1%
3T3	Matrigel	94% ± 1.9%	97% ± 0.15%	93% ± 0.45%
OVCAR8	Agarose	95% ± 2.0%	95% ± 0.59%	93% ± 0.68%
OVCAR8	Collagen	95% ± 2.0%	96% ± 1.1%	97% ± 0.34%

*2D cells were harvested from culture flasks.

2.3.3 Long term culture

Prolonged cultivation of 3D cell models, facilitating cellular adjustment, proliferation, maturation, and the establishment of stable markers[135], is indispensable across various disciplines, including cancer invasion studies[136], biomaterial scaffold remodelling[135], and investigations into chronic disease mechanisms[137]. Currently the duration of 3D culture for tumours, such as breast, colon, and liver, typically spans from 1 to 25 days[137]. Challenges associated with extending cultivation time encompass cell dedifferentiation, loss of contact inhibition, and decreased cell viability[138, 139]. In this work, we have achieved the extended culture period for our 3D microtumours up to 63 days (9 weeks) without significant morphological alterations (**Figure 2.15**).

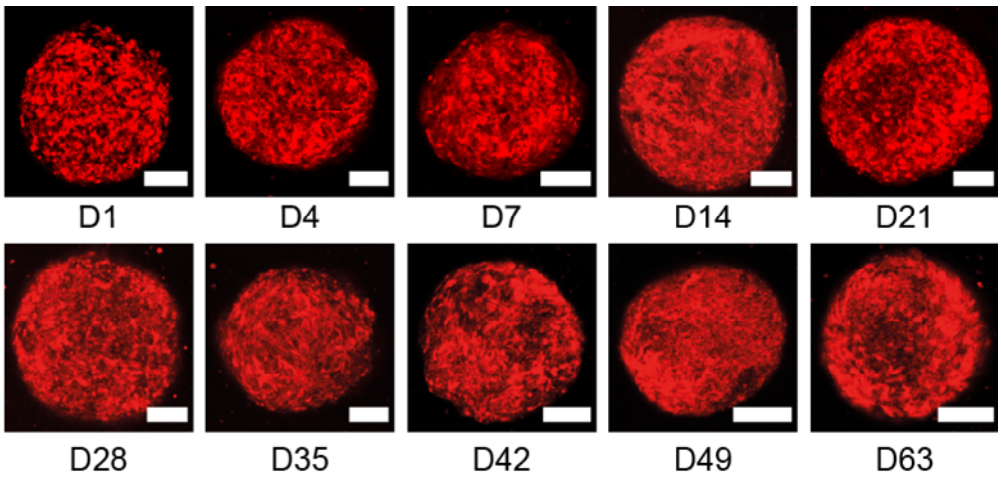


Figure 2.15. Long-term culture of 3D microtumours. The 3D microtumours were composed of OVCAR-5/RFP (red) and Matrigel. Confocal microscope images were taken from D0 to D63 after fabrication. Scale bar = 200 µm.

Live/Dead staining of 3D microtumours was conducted over a timeframe of 14 days (2 weeks). From D1 to D14, viable cells constituted the majority of the cell population (**Figure 2.16**). Cell proliferation was evident, with a noticeable

increase in cell density observed on D4. While the number of dead cells increased over time, they remained a minor portion of the population.

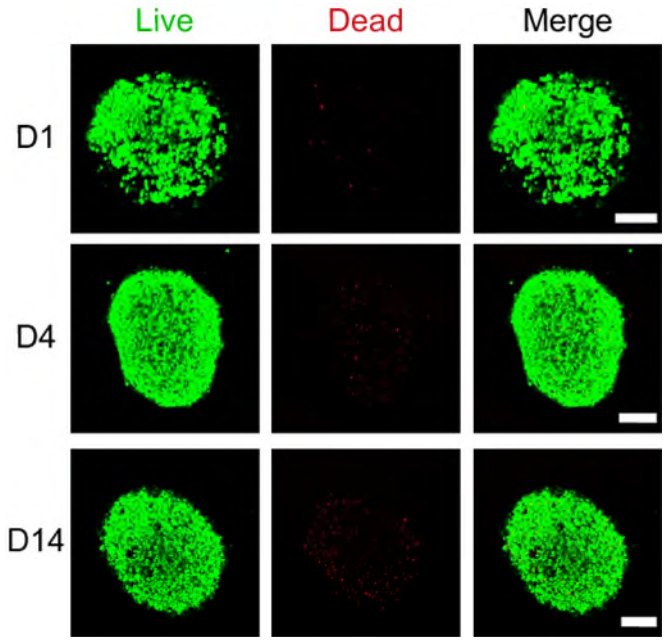


Figure 2.16. Live/Dead staining of 3D microtumours on different days. The 3D microtumours were composed of OVCAR8 and Matrigel. Confocal microscope images were taken on D1, D4 and D14 after fabrication. Scale bar = 200 µm.

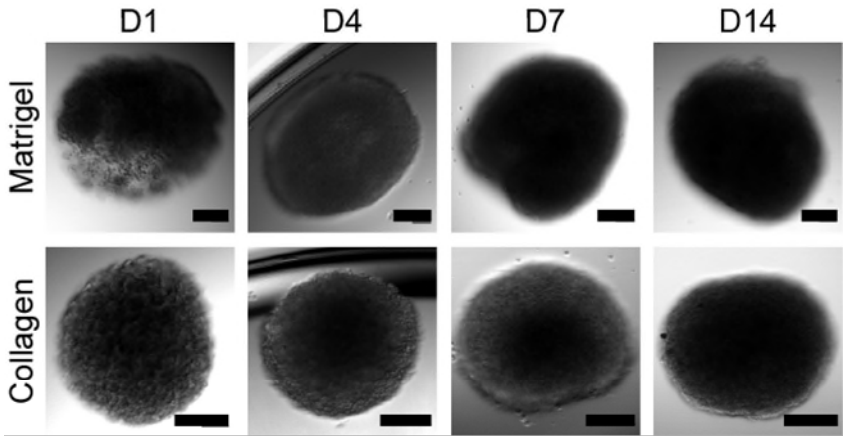


Figure 2.17. 3D microtumours composed various hydrogels on different days. The 3D microtumours were composed of OVCAR8 cells and Matrigel or collagen. Brightfield microscope images were taken on D1, D4, D7 and D14 after fabrication. Microtumours shown on different days were from the same batch, but not the identical ones. Scale bar = 200 µm.

Further, 3D microtumours composed of OVCAR8 ovarian cancer cells and different hydrogels were imaged and compared over a time period of 14 days. The growth in cell density over time was evident for 3D microtumours made with both Matrigel and collagen (**Figure 2.17**). Moreover, there were no significant changes in the size of OVCAR8 microtumours made with either Matrigel or collagen over the timeframe of 14 days (**Figure 2.18**).

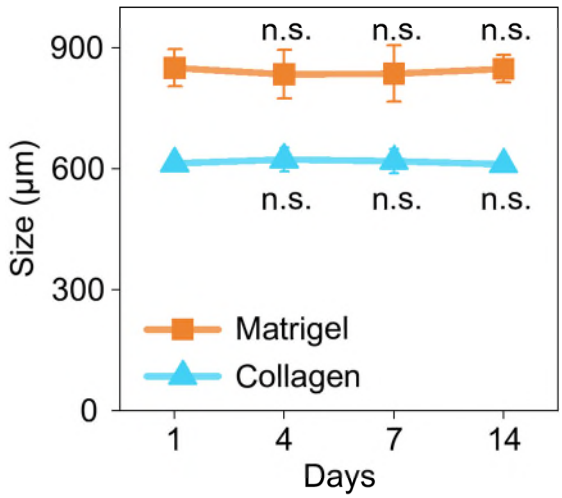


Figure 2.18. Size of 3D microtumours on different days. The 3D microtumours were composed of OVCAR8 cells and Matrigel or collagen (n = 3). Significance was tested using a Tukey test. n.s.: not significant, P > 0.05.

2.4 Summary

The microfluidic platform has been optimised for the fabrication of 3D microtumours. To achieve optimal results, we used Matrigel to prepare cell-hydrogel suspensions with a cell density above 3×10^7 cells mL^{-1} as the aqueous phase and tetradecane as the oil phase. These 3D microtumours, with a size ~900 µm, were fabricated using a cell-hydrogel suspension:oil flow rate ratio of 1000:3000 µL h^{-1} at 8°C. The microfluidic fabrication process only took 3 minutes

to produce 100 microtumours (pre-gel state), followed by a gelation time of 2 hours at 37°C (solidified microtumours).

The PrestoBlue Cell Viability Assay has been verified as a suitable method for assessing the viability of these 3D microtumours. High cell viability (>90%) was maintained throughout the microfluidic fabrication process. Moreover, these 3D microtumours can be cultured for an extended period, up to 9 weeks, and they begin to display hypoxic characteristics within just 1 day of culture.

3 Anticancer drug responses of 3D microtumours

3.1 Introduction

3D culture of tumour is an attractive model for drug screening, since it is more physiologically relevant to *in vivo* tumour, and outcompetes 2D culture composed of monolayer cells[140]. However, several technical challenges associated with 3D culture, such as the control of size and cell number, efficiency and reproducibility of fabrication, and capability to scale up production, must be addressed to enhance the reliability and predictive power of these models[141]. The physiological relevance of our microtumours was confirmed through transcriptomic analysis and immunofluorescence staining. The 3D microtumours developed in this thesis meet these technical criteria and demonstrate improved physiological relevance. As a result, they can be readily utilized for therapeutics testing, making them a valuable tool for drug screening and research.

In our therapeutics testing, we focused on ovarian cancer and created 3D microtumours using OVCAR-5/RFP cells. Recognizing that the TME provides significant components that extensively interact with tumour cells, we incorporated fibroblasts (a type of stromal cell) in the microtumours. For comparison, we also prepared 3D constructs composed solely of fibroblasts. We first characterised the 3D microtumours with transcriptomic analysis and microscopic imaging (immunofluorescence staining of biomarkers) to validate the biological relevance of the *in vitro* models. Then we applied first-line

chemotherapeutics and contrasted the response differences between the 3D microtumours and 2D cultures.

In this study, we evaluated the effectiveness of two well-established anticancer drugs, carboplatin and paclitaxel. These drugs have been widely recognized as the standard of care for cancer treatment for more than 20 years[142]. Endeavours to add a third anticancer agent failed to balance between treatment efficacy and patient survival[143].

Carboplatin is a platinum-based antitumour drug derived from cisplatin. Since being approved by FDA in 1980s, carboplatin has been used to treat multiple types of cancer, including ovary, lung, neck and testis cancer[144]. Similar to cisplatin and other platinum compounds, carboplatin works by binding DNA to form adducts. These carboplatin-DNA covalent binds are irreversible and can take the form of mono-adducts or di-adducts (intra- or interchain)[145]. These adducts inhibit cell functions, such as replication and transcription, eventually leading to cell death[146]. Among the adducts, interchain cross-linking is the most cytotoxic, since it connects different strands of DNA, causing errors in replication. Cells are then arrested in the G2/M phase of the cell cycle and induce apoptosis[147].

Paclitaxel, approved by FDA in 1992, has been a significant chemotherapeutics used to trea various types of cancer, such as ovarian cancer and breast cancer[148]. In 1963, crude extract of paclitaxel was first isolated from the bark of Taxus brevifolia, a Pacific yew tree[149]. Paclitaxel induces apoptosis in tumour cells by targeting microtubules, which constitute a major component of cytoskeleton and contribute to chromosome segregation during mitosis[150]. Paclitaxel stabilised microtubules by binding to β tubulin, a subunit of

microtubules. By preventing microtubule disassembly, paclitaxel causes tumour cells to become arrested in the G2/M phase of the cell cycle, resulting in termination of mitosis and ultimately cell death[149]. Additionally, paclitaxel can function through other pathways to eliminate tumour cells, for instance, inducing anti-tumour immunity, triggering tumour suppressor genes, and generating reactive oxygen species[151]. Paclitaxel's multifaceted mechanisms of action make it a potent anticancer agent.

Acknowledgement of collaboration

RNA-Sequencing (RNA-Seq) libraries preparation and analysis, cytoskeleton staining and confocal image processing in this chapter were finished by the author together with Dr Mara Artibani from Prof Ahmed Ahmed laboratory (Weatherall Institute of Molecular Medicine, University of Oxford).

3.2 Key physiological features recapitulated by 3D microtumours

2D monolayer cells and animal models have been used as a standard for drug testing for long. However, there are significant limitations to these models. 2D monolayer cells, exposed to an oversimplified microenvironment, change their phenotypes, metabolism and other bioactivities compared to tumours *in vivo*[152]. Physiological differences between humans and animals cause 94% of animal tests fail to give correct predictions in human responses[153]. These sub-optimal models used in drug screening, which fail to recapitulate certain physical and biochemical characteristics of tumours in patients, eventually lead to

disappointing results for almost 95% of drugs that enter clinical trials[153]. Among these critical features, we find 3D microtumours are capable of recapitulating hypoxia and cytoskeleton organisation *in vitro*.

3.2.1 Hypoxia

Hypoxic cores are formed due to the deficient oxygen and nutrient levels towards the centre of tumours[127, 128]. They contribute to reshaping of the tumour microenvironment and the development of immunosuppression and chemoresistance[154]. However, 2D monolayer cells lack the gradients of oxygen required to produce hypoxia.

Hypoxia is commonly observed in tumours with diameters larger than 400-500 μm. Nevertheless, tumour spheroids prepared by prevailing methods usually own the initial size within the range of 100-300 μm[72, 155], which may not exhibit hypoxia as they are relatively small. In this work, 3D microtumours with larger initial sizes can be conveniently produced. We prepared large, medium and small 3D microtumours (size = 820, 420, 270 μm) with OVCAR-5/RFP cancer cells and Matrigel. Significantly, hypoxic cores were observed in large 3D microtumours just 1 day after fabrication, while they were absent in medium and small size microtumours (**Figure 3.1**), which is consistent with the published literature[127, 128].

It is important to note that the hypoxia reagent employed in this study demonstrated fluorescence in conditions where the oxygen level was below 5%, whereas the oxygen tension in the human ovary is estimated to range from 2-8%[29]. To further confirm the presence of physiologically relevant hypoxic cores, immunofluorescence staining of hypoxia markers was conducted.

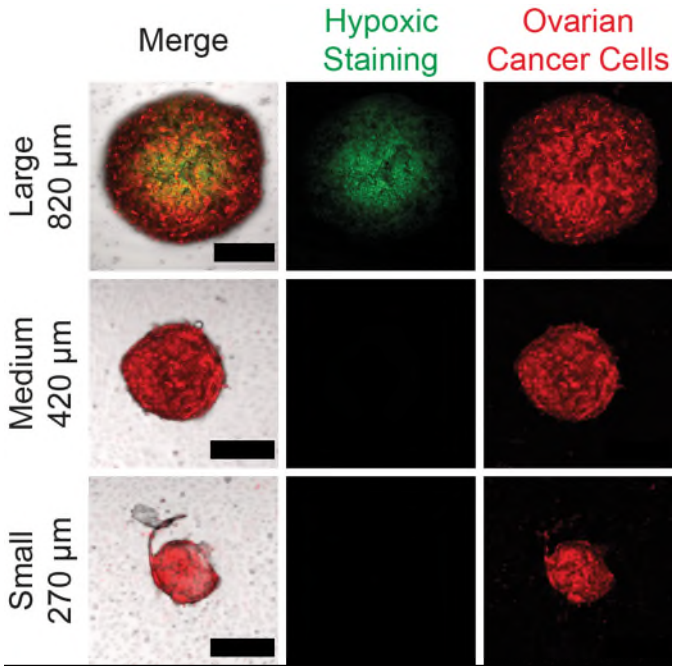


Figure 3.1. Hypoxic core staining for 3D microtumours of various size. Confocal microscope images of hypoxia staining (green) for large, medium and small 3D microtumours composed of OVCAR-5/RFP ovarian cancer cells (red) and Matrigel. Images were taken on D1 after fabrication. Scale bar = 300 µm.

The expression of key hypoxia genes was confirmed through immunofluorescence staining in more mature microtumours (**Figure 3.2**). By D10 after fabrication, the hypoxic regions had expanded, with the expression of P4HA1, VEGF and NDRG1 observed very strongly in the middle of the structure and, more faintly, in some cells closer to the edges.

In contrast, 3D spheroids prepared using alternative approaches, such as the forced aggregation method, required considerably longer time frames, ranging from 11 to 21 days, to reach a comparable size (>800 µm) and generate hypoxic cores, as reported in previous studies[128, 156].

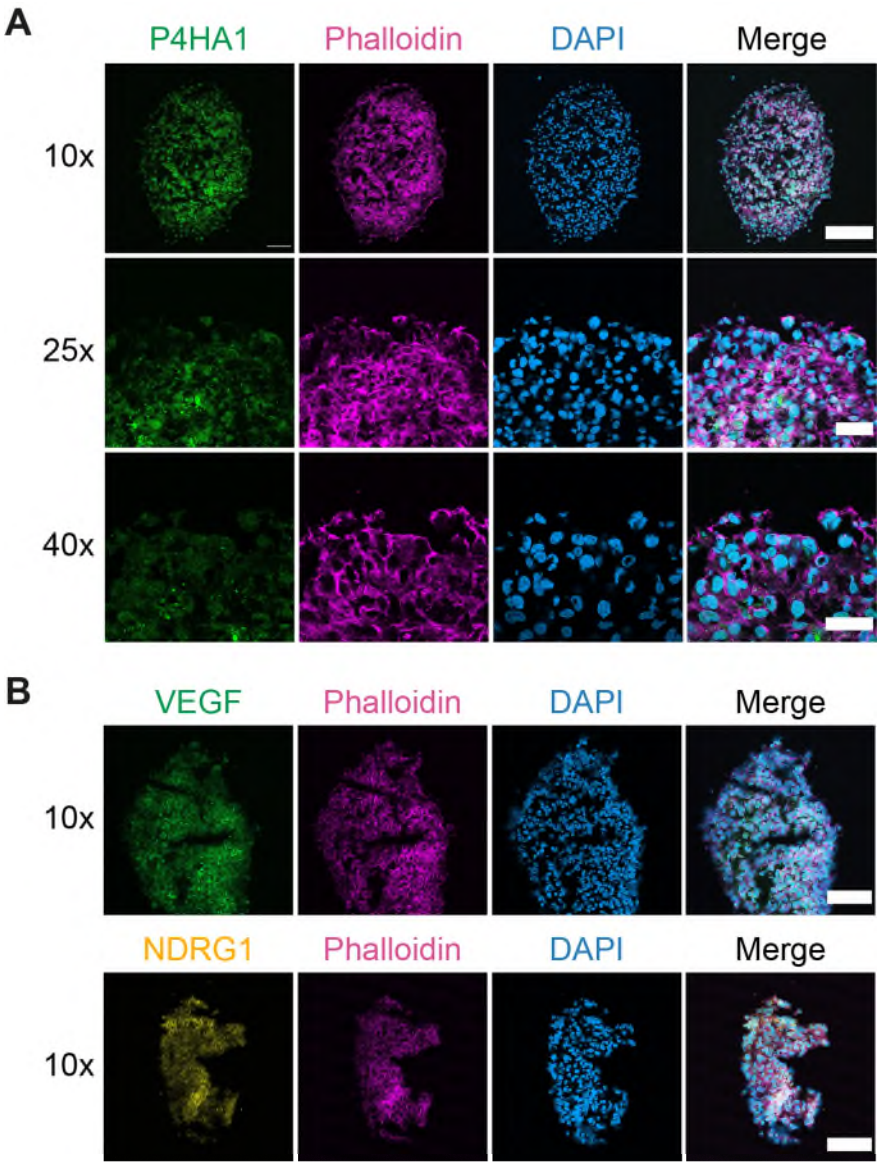


Figure 3.2. Immunofluorescence staining of hypoxia proteins for 3D microtumours. (A) Confocal images of 3D microtumours composed of OVCAR5 ovarian cancer cells and Matrigel at D10 stained with P4HA1 (green), phalloidin (pink), 4′,6-diamidino-2-phenylindole (DAPI, blue). Scale bar = 200 µm for 10x, 50 µm for 25x, 40 µm for 40x magnification. (B) Confocal images of 3D microtumours composed of OVCAR5 ovarian cancer cells and Matrigel at D10 stained with VEGF (green), NDRG1 (yellow), phalloidin (pink), DAPI (blue). Scale bar = 150 µm.

RNA-Seq analysis was performed on both 2D cultures and 3D microtumours to complement the results obtained from staining experiments. Baker et al. documented the upregulation of a panel of nine genes, which includes vascular endothelial growth factor A (VEGFA), glucose transporter 1 (SLC2A1),

phosphoglycerate mutase 1 (PGAM1), lactate dehydrogenase A (LDHA), prolyl 4-hydroxylase (P4HA1), adrenomedullin (ADM), N-myc downstream regulated 1 (NDRG1), aldolase A (ALDOA), and carbonic anhydrase 9 (CA9), in ovarian cancer cell lines cultured under hypoxic conditions (1% oxygen)[157]. We analysed the expression of this nine-gene ovarian cancer-specific hypoxic signature with samples from three ovarian cancer cell lines: OVCAR5, OVCAR8 and OVCAR-5/RFP, all of which fall under the classification of HGSOC. The analysis revealed that 3D microtumours composed of OVCAR5 and OVCAR-5/RFP were found to upregulate almost all these hypoxic signature genes (**Figure 3.3**); while for OVCAR8, only VEGFA and NDRG1 were upregulated.

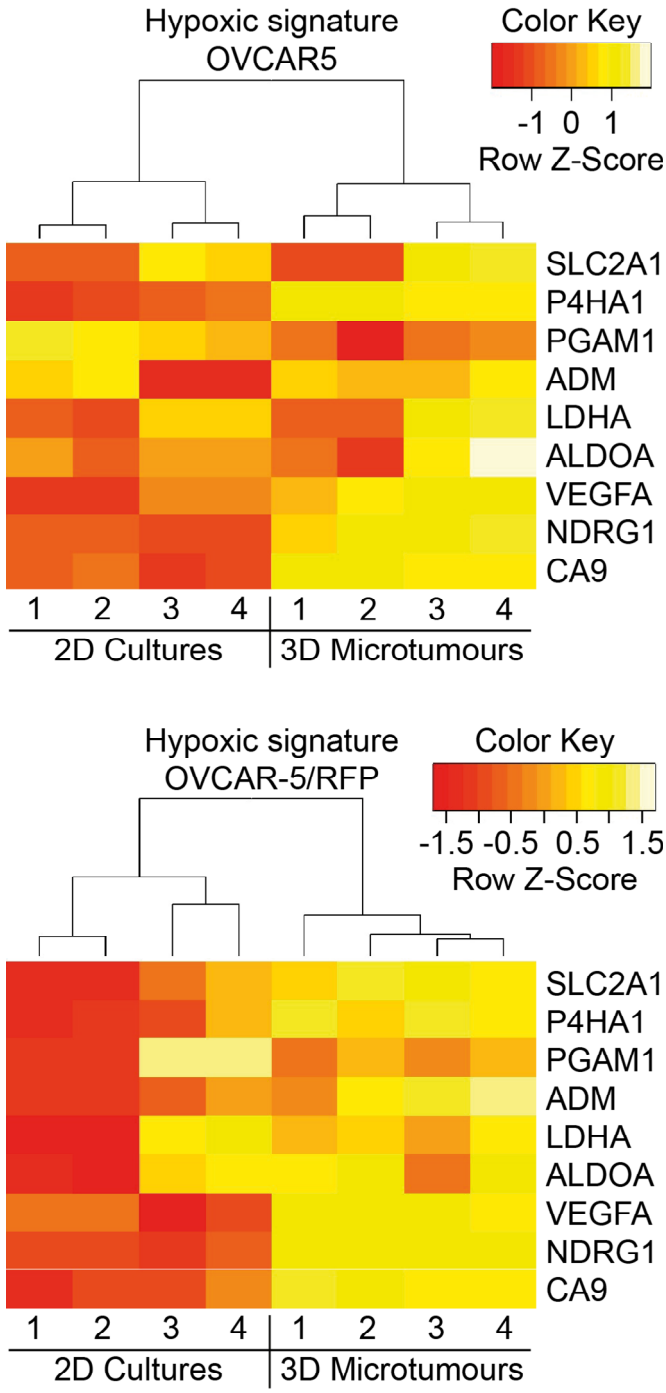


Figure 3.3. Heatmaps showing the expression of hypoxic signature. A nine-gene ovarian cancer specific hypoxic signature was analysed for 2D cultures and 3D microtumours made of OVCAR5 (top) and OVCAR-5/RFP (bottom).

Further, we conducted gene ontology (GO) enrichment analysis, which focused on gene sets rather than individual genes. When performing GO enrichment analysis on the genes that were upregulated in 3D microtumours, there was enrichment of gene ontology biological processes (GOBP) related to

hypoxia and cell motility in 3D microtumours when compared to 2D cultures, regardless of the cell line used (**Figure 3.4**). For example, one of the hypoxia related GOBPs, the positive regulation of VEGF production, was enriched 16-fold in 3D microtumours.

On the other side, 2D cultures upregulated genes related to Cell Cycle, Mitotic reactome pathways (ID 1269763) (**Figure 3.5**) and enriched in GOBP related to cell cycle (**Figure 3.6**), consistent with the fact that unlimited supply of oxygen and nutrients promote faster cell division.

These results, spanning from the transcriptomic level to protein expression, clearly demonstrated the successful recapitulation of hypoxia in 3D microtumours. Notably, the microfluidic platform enabled the rapid establishment of hypoxic characteristics in just one-tenth of the time compared to traditional methods.

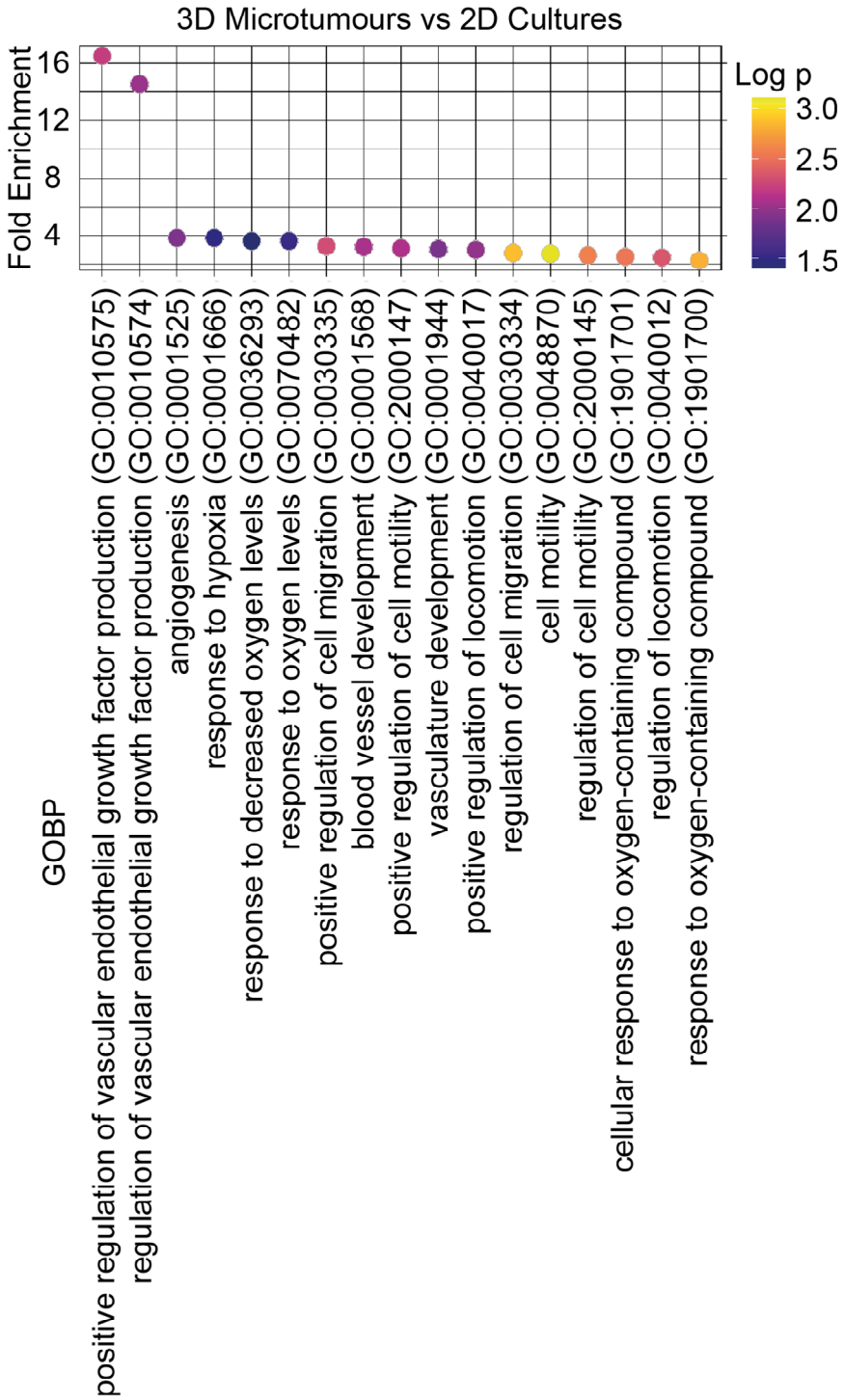


Figure 3.4. Dot plots showing the main gene ontology biological processes (GOBP) enriched in 3D microtumours. The 3D microtumours and 2D cultures were produced from OVCAR5, OVCAR8 and OVCAR-5/RFP cells.

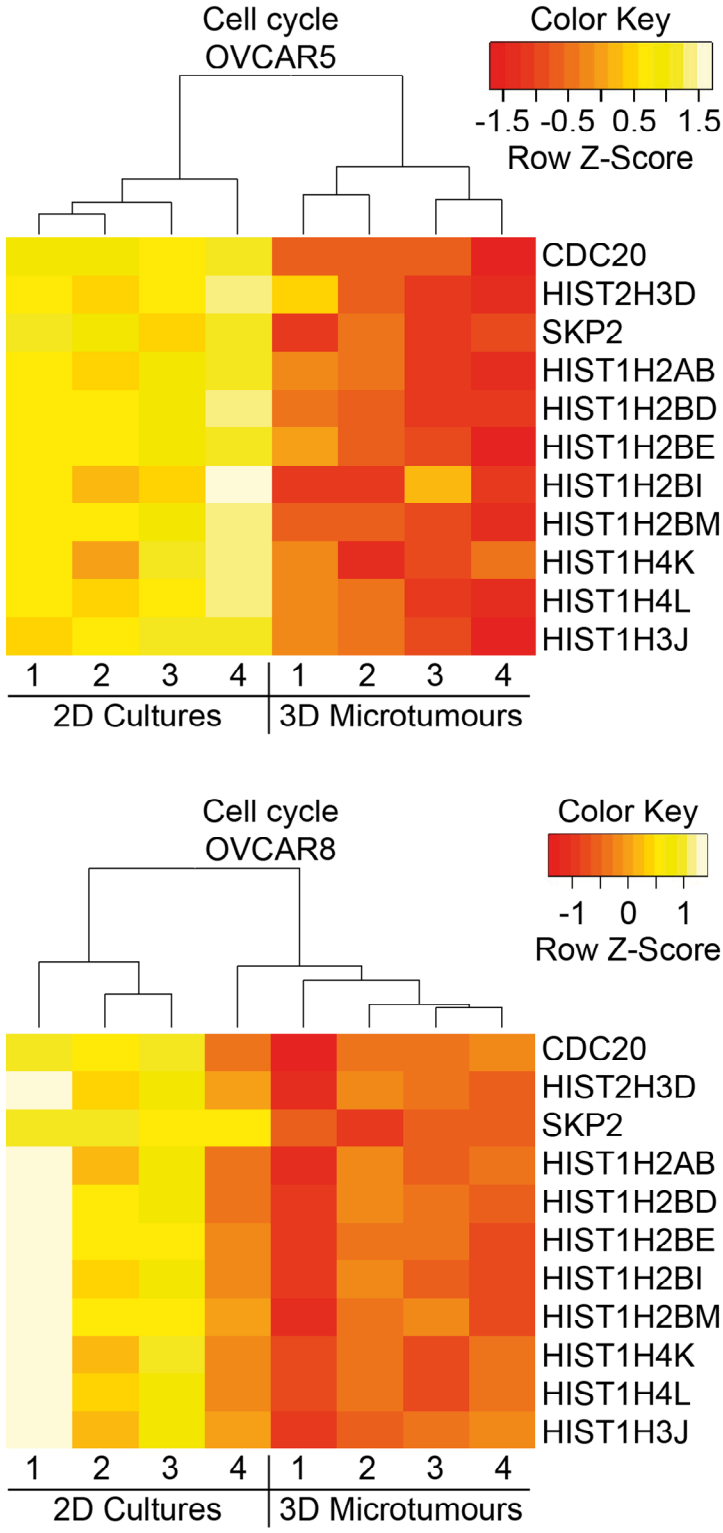


Figure 3.5. Heatmaps showing the expression of cell cycle related genes. 2D cultures and 3D microtumours made of OVCAR5 (top) and OVCAR8 (bottom) were shown.

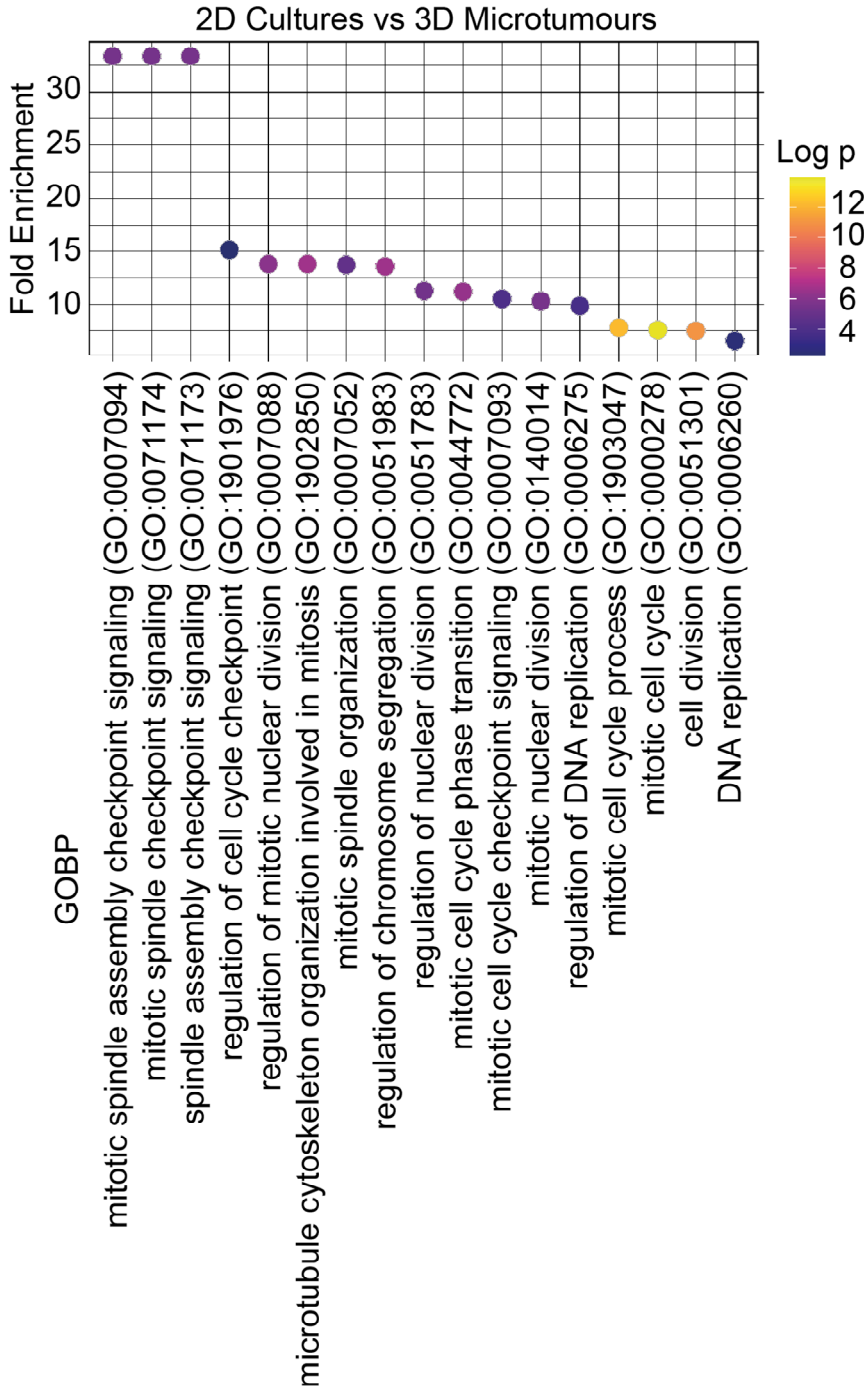


Figure 3.6. Dot plots showing the main GOBP enriched in 2D cultures. The 3D microtumours and 2D cultures were produced from OVCAR5, OVCAR8 and OVCAR-5/RFP cells. GOBPs related to cell cycles were found to be enriched in 2D cultures compared to 3D microtumours.

3.2.2 Cytoskeleton organisation

Cytoskeleton organisation, which is essential in cell motility, affects tumour invasion and metastasis. Actin filament is one of the three types of protein fibres

in the cytoskeleton. They function at different levels, from forming networks to connect to plasma membrane, providing mechanical supports to give cell shape and structure, to participating in crucial activities, such as mitosis and cell motility, all of which are altered in cancer[158].

Filamentous actin structures, such as lamellipodia and stress fibres, are prominently found when cells are cultured on flat and rigid 2D surfaces, yet they are rarely observed *in vivo*[159]. To explore whether our 3D microtumours could recapitulate the actin architectures observed *in vivo*, we stained filamentous actin with phalloidin and compared across 2D cultures, 3D microtumours and clinical pre-chemotherapy biopsies samples from patients with HGSOC. In 2D cultures, we observed the formation of thin, linear and parallel arrays of actin filaments, named filopodia, extending from the cells. In contrast, both 3D microtumours and clinical samples exhibited complex networks with branched and thick actin bundles (**Figure 3.7**).

As demonstrated by the results above, 3D microtumours recapitulate key physiological characteristics of tumours in patients, which are essential for reliable drug response prediction.

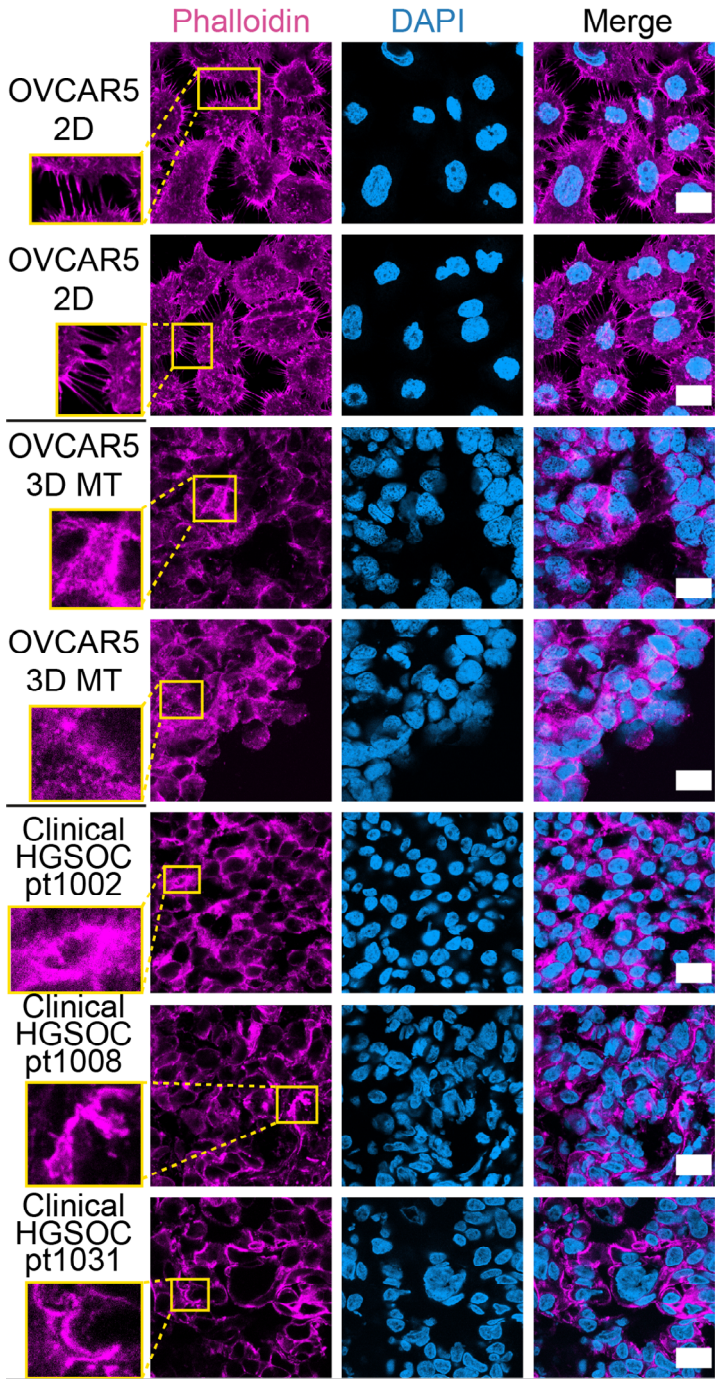


Figure 3.7. Cytoskeleton organisations of *in vitro* and clinical samples. Confocal images of 2D cultures (OVCAR5), 3D microtumours (3D MT, OVCAR5) at D10 after fabrication, and clinical samples of HGSOC stained with phalloidin (pink), DAPI (blue). Scale bar = 20 µm. Inset: zoom-in images for regions of interest stained with phalloidin.

3.3 Size distribution of 3D microtumours

One of the popular applications of 3D microtumours is drug screening. To make the drug screening experiments reliable and reproducible, the cell content and cell population within each 3D microtumour must be consistent. When using the microfluidic platform to prepare 3D microtumours, the suspensions were well-mixed to ensure homogeneity. Control over the size of microtumours is essential.

We fabricated 3D microtumours of different sizes simply by using PTFE exit tubes with different IDs. For each batch of fabrication, the 3D microtumours showed a narrow size distribution with coefficient of variation (CV) of 2 to 6% (**Figure 3.8**). The CV value is much smaller compared to tumour spheroids formed by hanging-drop[160], micro-sieve[161], or scaffold methods[162], whose CV values fall in the range of 10 to 60%. The mean and median values of the microtumour dimension were approximate (**Table 3.1**), further supported the mono-dispersity of size for 3D microtumours from a single batch of fabrication, regardless of cell contents and tube IDs. The narrow size distribution and thus the uniform cell population within each microtumour technically underpinned the application in drug screening.

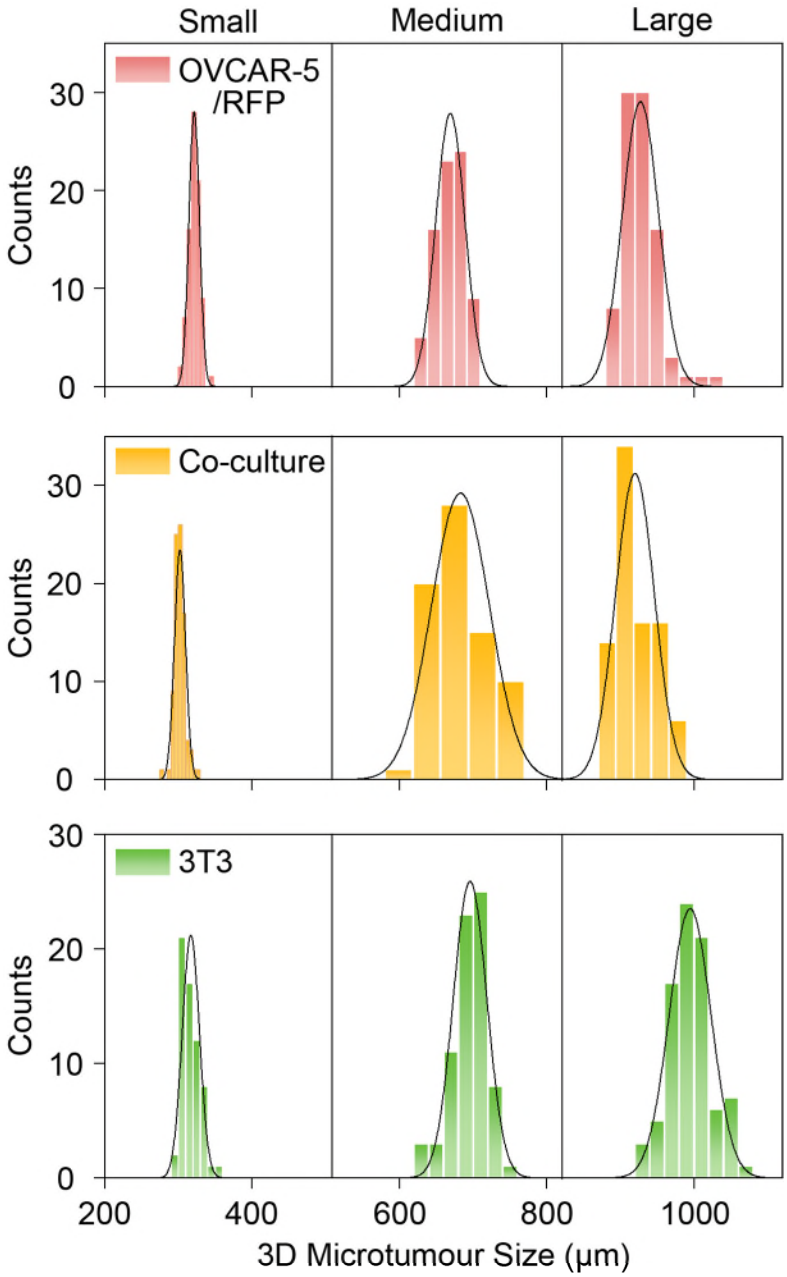


Figure 3.8. Size distributions of 3D microtumours. 3D microtumours of three cell compositions encapsulated in Matrigel were prepared: OVCAR-5/RFP tumour cells, co-culture (50: 50 mixture of OVCAR-5/RFP and 3T3 cells) and 3T3 fibroblast cells (n = 62 to 90). For each composition, the microtumours were generated with PTFE exit tubes of ID = 300, 650 and 900 μm, respectively. Size was measured on D0 after fabrication.

Table 3.1. Dimensions of 3D microtumours of various size groups and compositions. 3D microtumours were formed by Matrigel and three cell compositions: OVCAR-5/RFP tumour cells, co-culture (50: 50 mixture of OVCAR-5/RFP and 3T3 cells), and 3T3 fibroblast cells. Size was measured on D0 after fabrication.

Cell	Size group	3D microtumour size (μm)			
		N total	Median	Mean ± SD[a]	CV[b]
OVCAR-5/RFP	Small	84	320	320 ± 7.2	2.3%
OVCAR-5/RFP	Medium	77	670	670 ± 20	3.0%
OVCAR-5/RFP	Large	90	920	930 ± 25	2.7%
Co-culture	Small	88	300	300 ± 7.5	2.5%
Co-culture	Medium	76	680	680 ± 40	5.9%
Co-culture	Large	86	910	920 ± 26	2.8%
3T3	Small	62	310	320 ± 12	3.8%
3T3	Medium	74	700	700 ± 23	3.3%
3T3	Large	84	990	990 ± 28	2.8%

[a]SD: standard deviation.
[b]CV: coefficient of variation. CV = SD/Mean.

3.4 Anticancer drug dose-responsive curve

3.4.1 Workflow design for drug screening

The drug screening experiments were conducted using 3D microtumours produced with the microfluidic platform, characterized by narrow size distributions. Large microtumours (size around 900 μm) were used for these experiments due to their ability to replicate hypoxic characteristics and their higher biological relevance. Three types of 3D constructs were used in the drug screening: (1) ovarian cancer cells; (2) co-culture of ovarian cancer cells and fibroblasts – to explore how stromal cells affected drug responses of tumour cells; and (3) fibroblasts – as a negative control.

On D0, both freshly prepared 3D microtumours and 2D cultures (used for comparison), were dispensed into 96-well plates. They were cultured for 2 days to allow for cell proliferation and to generate cell-cell interactions. After this, they

were exposed to serial dilutions of carboplatin or paclitaxel. Since both drugs target rapidly dividing cells, the treatment duration was designed to match the cell doubling time. At the end of the 4-day drug treatment, cell viabilities were measured and normalised to the corresponding untreated vehicle control groups (**Figure 3.9**). The IC_{50} values were derived from dose-responsive curves using non-linear fitting.

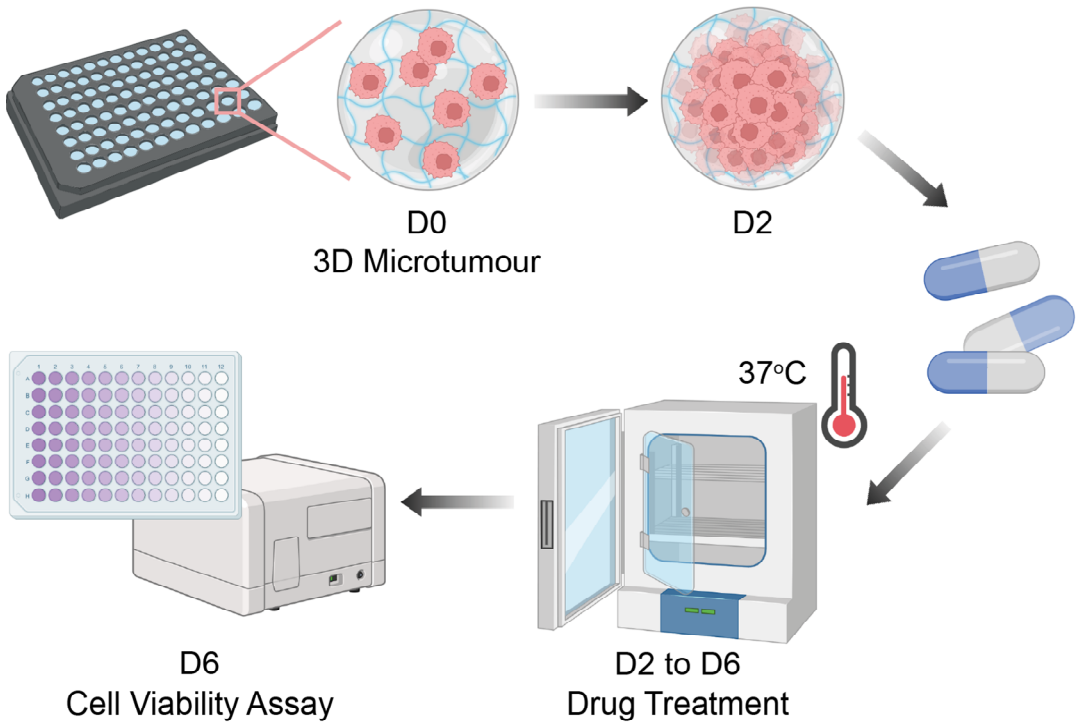


Figure 3.9. Schematic diagram showing the evaluation of chemotherapeutic responses with 3D microtumours. Each 3D microtumour was seeded to one well of a 96-well plate on D0 of fabrication and kept at 37°C, 5% CO_2 for 2 days. On D2, serial dilutions of chemotherapeutics were applied and the microtumours were cultured at 37°C, 5% CO_2 for 4 days. On D6, a cell viability assay was performed for each 3D microtumour. The diagrams were created with BioRender.com.

In Section 2.3.1, we established that the PrestoBlue Cell Viability Assay is suitable for quantify viable cells in 3D microtumours. Additionally, we recognised the importance of optimising the incubation time for the assay based on the size and compactness of the microtumours. To achieve this, we obtained readouts at

various time points to determine the optimal performance of the assay under our specific experimental conditions.

To investigate the optimal incubation time for the PrestoBlue assay, we subjected 3D microtumours, prepared with PTFE exit tubes of ID = 900 µm, to varying durations of incubation with PrestoBlue reagent at 37°C, following a 4-day treatment with serial dilutions of carboplatin. We observed that longer incubation times led to higher fluorescence, resulting in increased sensitivity of detection (**Figure 3.10**A). When we normalised cell viabilities to the untreated vehicle control, we found that the dose-response curves nearly overlapped with each other for incubation times ranging from 30 to 60 minutes (**Figure 3.10**B). Furthermore, longer incubation times (30 to 60 minutes) were associated with narrower error bars compared to a 15-minute incubation.

Therefore, balancing between the assay sensitivity of detection and efficiency, we chose an incubation time of 30 minutes for the PrestoBlue Cell Viability Assay.

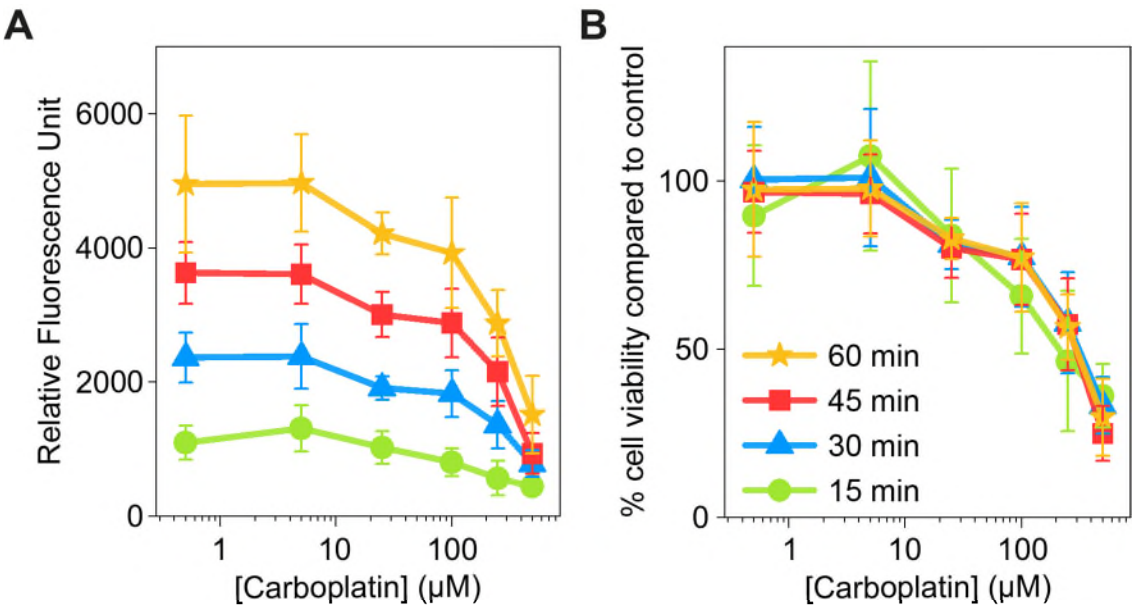


Figure 3.10. Optimisation of assay reagent incubation time for 3D microtumours. The drug responses of large 3D microtumours (size around 900 µm) were evaluated with PrestoBlue Cell Viability Assay.

3.4.2 Ovarian cancer 3D microtumours

3D microtumours composed of OVCAR-5/RFP ovarian cancer cells were tested with carboplatin and paclitaxel of various concentrations. Dose-dependent effects were observed for both drugs, allowing for the calculation of IC_{50} values from the concentration-response curves (**Figure 3.11**). Specifically, the ovarian cancer 3D microtumours exhibited IC_{50} values of 100 ± 12 µM for carboplatin and 5.3 ± 2.0 nM for paclitaxel. These values were notably higher than those observed for 2D cultures, which had IC_{50} values of 60 ± 6.1 µM for carboplatin and 2.7 ± 0.9 nM for paclitaxel.

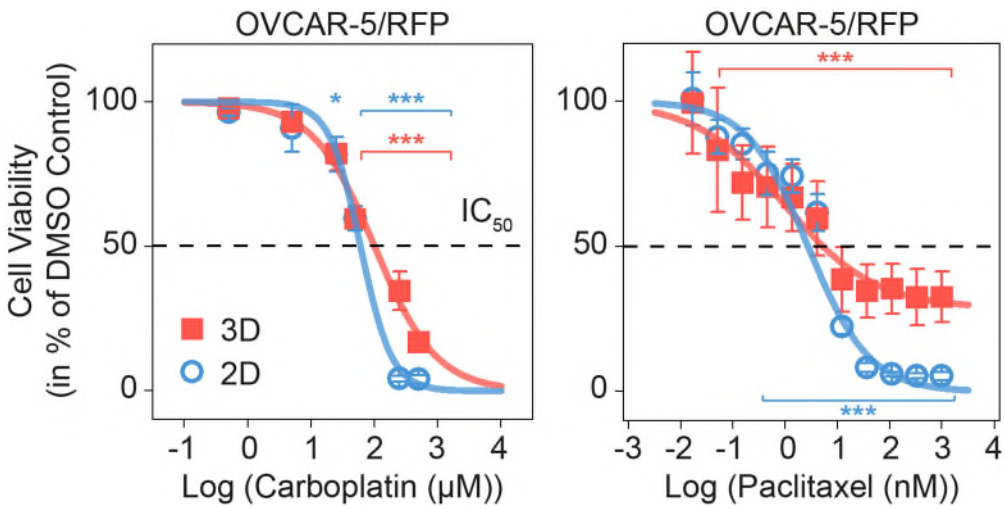


Figure 3.11. Chemotherapeutics responses of OVCAR-5/RFP tumour cells. Serial dilutions of carboplatin (left) and paclitaxel (right) were applied to 3D microtumours (n =15 to 20) and 2D cultures (n = 12 to 14). Significance compared to drug-free control group was tested using a Tukey test. ***P < 0.001, **P < 0.01, *P < 0.05.

In the case of carboplatin treatment, there was a sharp decrease in cell viability in 2D cultures, dropping from 60% at a treatment concentration of 50 µM to only 5% at 250 µM. However, in 3D microtumours, no such abrupt change in viability was observed.

Interestingly, in the case of paclitaxel treatment, we observed that ovarian cancer cells could not be completely eliminated even at high concentrations, especially for 3D microtumours. A plateau was reached, and no further reduction in cell viability was observed. Approximately 33% of the cells in 3D microtumours survived at 1000 nM, whereas in 2D cultures, only 5% of the cells remained viable.

Next, we compared the IC_{50} values derived from the *in vitro* models with the theoretical maximum plasma concentration (C_{max}), which serves as an indicator of drug absorption rate in patients[163].

Patients typically receive intravenous infusions of carboplatin and paclitaxel as cycles of treatment. Each cycle lasts for three weeks and 3 to 8 cycles are administered depending on cancer stage[164]. During each treatment cycle, drug concentrations in the patient's plasma can be monitored using high-performance liquid chromatography (HPLC) at certain discrete time points, allowing the creation of a time-concentration curve. From this curve, the area under curve (AUC) is derived to represent the total drug exposure over time[165]. The C_{max} can be calculated from the AUC through Calvert formula[166].

For a typical carboplatin dosage with the AUC of 5 mg min mL^{-1}, a theoretical C_{max} was estimated to be 280 µM (calculations in **Table 3.2**), though the C_{max} derived from a cohort of 11 ovarian cancer patients was 105 µM[165]. CA125, a useful biomarker to evaluate treatment responses and to monitor ovarian cancer relapse, was found to be reduced to one-half in serum concentration *in vivo* after each cycle of neoadjuvant chemotherapy[167]. The carboplatin IC_{50} value of 3D microtumours (100 ± 12.3 µM) aligns to the C_{max} (105 µM) that causes 50% reduction of cancer biomarker levels. In contrast, the 2D cultures are around twice as sensitive.

Table 3.2. Calculations for theoretical carboplatin C_{max} and the *in vitro* equivalent dose.

Theoretical carboplatin plasma C_{max}	First, Cockcroft-Gault formula was used to estimate glomerular filtration rate (GFR): $\mathrm{GFR(mL\ min^{-1})} = \frac{(140 - \mathrm{age}) \times \mathrm{weight(kg)}}{72 \times \mathrm{Serum\ creatinine\ (mg\ dL^{-1})}} \times 0.85$ Consider the average epithelial ovarian cancer patient parameters of age 63[168], weight 69 kg[169], serum creatinine 0.85 mg dL^{-1} and female gender[170]. $\mathrm{GFR} = 74\ \mathrm{mL\ min^{-1}}$. Next, the Calvert formula was used to calculate carboplatin dose: $\mathrm{Dose(mg)} = \mathrm{AUC(mg\ min\ mL^{-1})} \times [\mathrm{GFR(mL\ min^{-1})} + 25\mathrm{(mL\ min^{-1})}]$ For an AUC of 5 mg min mL^{-1}, $\mathrm{Dose} = 490\mathrm{mg}$. Assume no excretion and serum-only distribution during the 30-minute infusion window, with a typical blood volume of 4.7 L, to yield the theoretical $C_{max} = 280\ \mu\mathrm{M}$.
Equivalent *in vitro* dose for carboplatin AUC	Drug concentration (C) at time t can be calculated as: $C = C_0 \cdot e^{kt}$ where C_0 is the initial drug concentration, and k is the elimination rate constant. *In vitro*, we assumed no distribution phase, and a prolonged half-life of 24 hours (i.e., 1440 minutes). With $C/C_0 = 1/2$, $t_{1/2} = 1440$, we obtained $k = \ln 2/1440$. AUC can be derived by integrating $C = C_0 \cdot e^{kt}$ from 0 to ∞: $\mathrm{AUC} = C_0/k$ For an AUC of 5 mg min mL^{-1}, $C_0 = 5k = 0.0024\ \mathrm{mg\ mL^{-1}} = 6.5\mu\mathrm{M}.$

Additionally, we calculated the *in vitro* carboplatin dose required to achieve bioequivalent AUC *in vivo* (**Table 3.2**). The calculated concentration (6.5 µM) is significantly lower than clinical results, highlighting the difficulty of recapitulating pharmacokinetics *in vitro*.

3.4.3 Co-culture 3D microtumours

Uncontrolled proliferation of tumour cells involves, but cannot be solely explained by the alterations in signalling pathways related to oncogenes and tumour suppressor genes[171]. TME, which comprises of non-cancerous components, including stromal cells and ECMs, has been found to extensively interact with tumour cells and contribute to tumour development and chemotherapy resistance[172].

Fibroblasts, a crucial population of stromal cells in TME, are referred to as cancer-associated fibroblasts (CAFs) when they are present in the tumour milieu. CAFs are found to regulate tumour progression, increase platinum resistance, and imply poor prognosis[173]. For example, the overexpression of fibroblast activation protein α (FAP), a protein expressed by CAFs, were found to associate with platinum resistance and shorter recurrence[174].

To move one step closer to mimicking the *in vivo* TME, we incorporated fibroblasts into the 3D microtumours of ovarian cancer. This co-culture consisted of an equal mix of OVCAR-5/RFP cancer cells and 3T3 fibroblasts, aiming to provide a microenvironment that is more physiologically relevant.

We treated the co-culture, and 3T3 fibroblasts for comparison, with the same chemotherapeutic scheme as applied to ovarian cancer 3D microtumours. Dose-

dependent responses to both drugs were observed in co-culture (**Figure 3.12**) and 3T3 fibroblasts (**Figure 3.13**), in both 3D microtumours and 2D cultures.

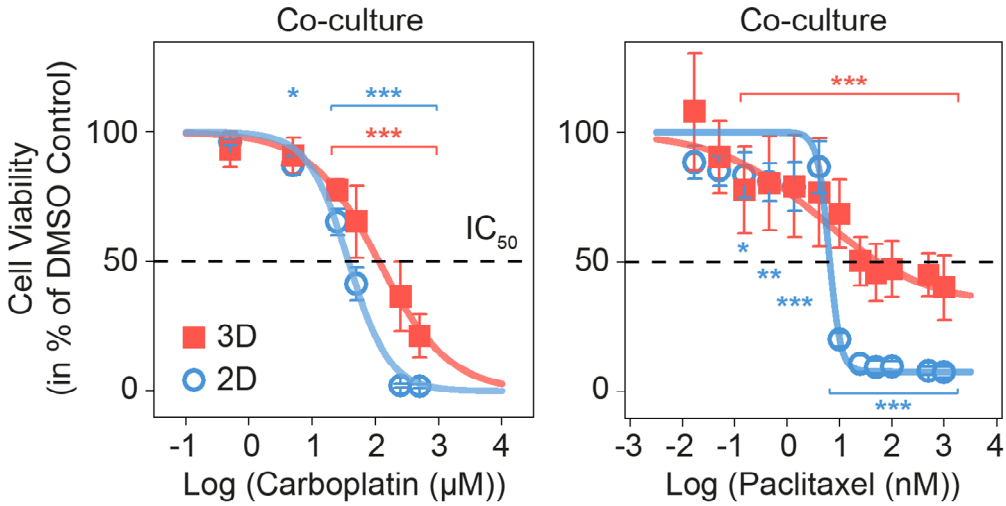


Figure 3.12. Chemotherapeutics responses of co-culture (50: 50 mixture of OVCAR-5/RFP tumour cells and 3T3 fibroblast cells). Serial dilutions of carboplatin (left) and paclitaxel (right) were applied to 3D microtumours (n =16 to 18) and 2D cultures (n = 14). Significance compared to drug-free control group was tested using a Tukey test. ***P < 0.001, **P < 0.01, *P < 0.05.

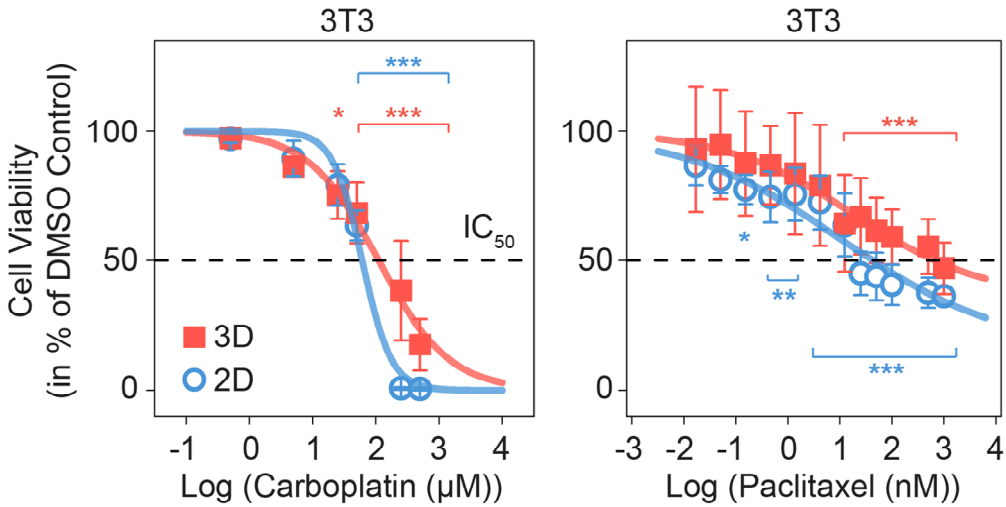


Figure 3.13. Chemotherapeutics responses of 3T3 fibroblast cells. Serial dilutions of carboplatin (left) and paclitaxel (right) were applied to 3D microtumours (n =16 to 20) and 2D cultures (n = 14). Significance compared to drug-free control group was tested using a Tukey test. ***P < 0.001, **P < 0.01, *P < 0.05.

In the case of carboplatin treatment, significant decrease in cell viability was observed in 2D cultures as the treatment concentration increased from 50 µM to 250 µM. For the co-culture, cell viability dropped from 41% to 2%, and for 3T3 fibroblasts, it decreased from 64% to 1%. However, no abrupt changes in viability were found in the co-culture or 3T3 fibroblast 3D microtumours, consistent with the results from the OVCAR-5/RFP 3D microtumours.

In the case of paclitaxel treatment, a similar phenomenon was observed where the cells in co-culture could not be completely eliminated even at high concentrations, consistent with the responses observed in ovarian cancer cells. Approximately 37% of cells remained viable in 3D microtumours at a concentration of 1000 nM, while only 7% of cells were viable in 2D cultures.

However, the response of 3T3 fibroblasts to paclitaxel treatment showed a different pattern. At a high concentration of 1000 nM, approximately 46% of cells remained viable in 3D microtumours, and about 34% of cells were viable in 2D cultures. Several studies have demonstrated that paclitaxel selectively induces apoptosis in tumour cells, but exhibits lower side effects on normal cells[175-177]. The differential cytotoxicity of paclitaxel towards cancerous and normal cells can be explained by the mitotic arrest in different phases of the cell cycle[175]. Trielli et al. reported that normal cells are primarily arrested in G1 phase by paclitaxel and can recover normally and proliferate upon release. However, paclitaxel-treated T antigen (an oncoprotein derived from the polyomavirus SV40) transformed REF-52 rat primary fibroblast cells can bypass G1 and G2/M arrest, leading to inappropriate mitotic exit, the formation of aneuploid daughter cells, and ultimately cell death upon release[178].

The IC_{50} values were calculated based on the dose-response curves and compared across the three composition groups: OVCAR-5/RFP ovarian cancer only, co-culture, and 3T3 fibroblasts only (**Figure 3.14**, **Table 3.3**). In general, 3D microtumours exhibited higher IC_{50} values compared to 2D cultures, which is consistent with literature[179, 180]. The enhanced drug resistance in 3D microtumours can be attributed to drug penetration, complex structure and up- or down-regulation of signalling pathways[181].

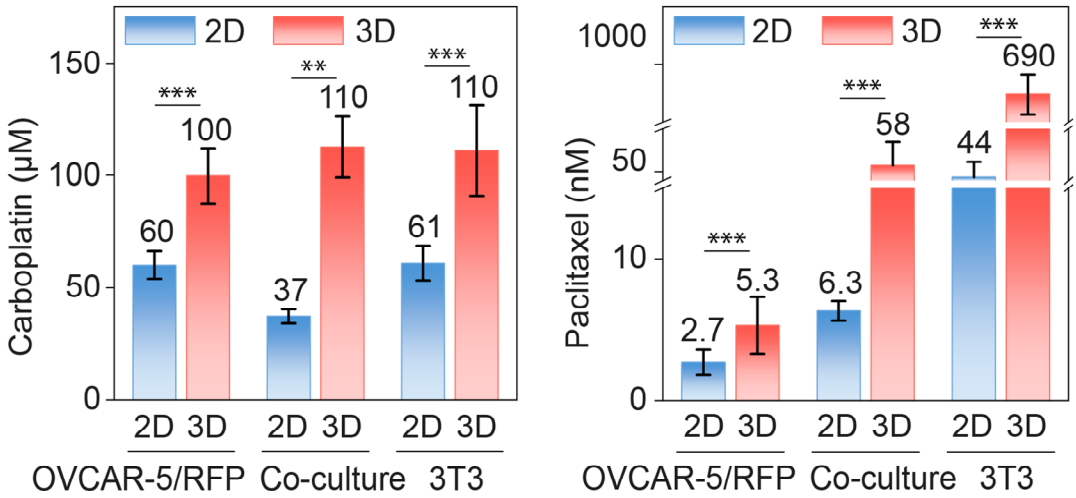


Figure 3.14. IC_{50} values for 3D microtumours and 2D cultures. Bar graphs of IC_{50} values calculated from the dose-response curves for carboplatin (left) and paclitaxel (right). Significance was tested using a Tukey test. ***P < 0.001, **P < 0.01, *P < 0.05.

Table 3.3. IC_{50} values calculated from carboplatin and paclitaxel dose-response curves.

Composition	IC_{50}	2D	3D
OVCAR-5/RFP	Carboplatin (μM)	60 ± 6.1	100 ± 12
	Paclitaxel (nM)	2.7 ± 0.9	5.3 ± 2.0
Co-culture	Carboplatin (μM)	37 ± 3.1	110 ± 14
	Paclitaxel (nM)	6.3 ± 0.7	58 ± 27
3T3	Carboplatin (μM)	61 ± 7.6	110 ± 20
	Paclitaxel (nM)	44 ± 18	690 ± 210

Further, we compared the IC_{50} values between ovarian cancer cells cultured alone and co-culture in different culture formats (3D or 2D), to examine how the presence of stromal cells affected drug responses. For paclitaxel treatment, IC_{50} value of 3D microtumours in co-culture was 11-fold higher than that of OVCAR-5/RFP cells alone. In contrast, for 2D cultures, the IC_{50} was only 2.3-fold higher in co-culture compared to tumour cells alone (**Table 3.4**). These results suggest that the incorporation of stromal cells in tumour cells would contribute to the development of drug resistance, regardless of the culture format. Additionally, the increased complexity of spatial arrangements of cells in 3D microtumours may induce differences in crosstalk between fibroblasts and tumour cells, which could contribute to therapeutic failure.

Table 3.4. Comparison of paclitaxel IC_{50} values in co-culture over OVCAR-5/RFP.

Paclitaxel IC_{50} (nM)	Co-culture	OVCAR-5/RFP tumour cells only	Fold change for IC_{50} value of Co-culture over OVCAR-5/RFP
3D	58 ± 27	5.3 ± 2.0	11
2D	6.3 ± 0.7	2.7 ± 0.9	2.3

3.5 Cell migration in co-culture 3D microtumours

Intriguingly, the co-culture 3D microtumours exhibited distinct migration patterns over time. On D0 upon microfluidic fabrication, both ovarian cancer cells and 3T3 fibroblasts were homogeneously dispersed throughout the entire 3D microtumour. Ovarian cancer cells maintained this even distribution within the structure from D0 to D4. On the contrary, 3T3 fibroblasts were observed migrating toward the periphery of the microtumours from D2, and by D4, they had accumulated distinctly at the edges (**Figure 3.15**A). The fluorescence intensity

distribution, which is proportional to the number of cells, confirmed that more 3T3 fibroblasts were located at the rim rather than in the centre of 3D microtumour (**Figure 3.15**B).

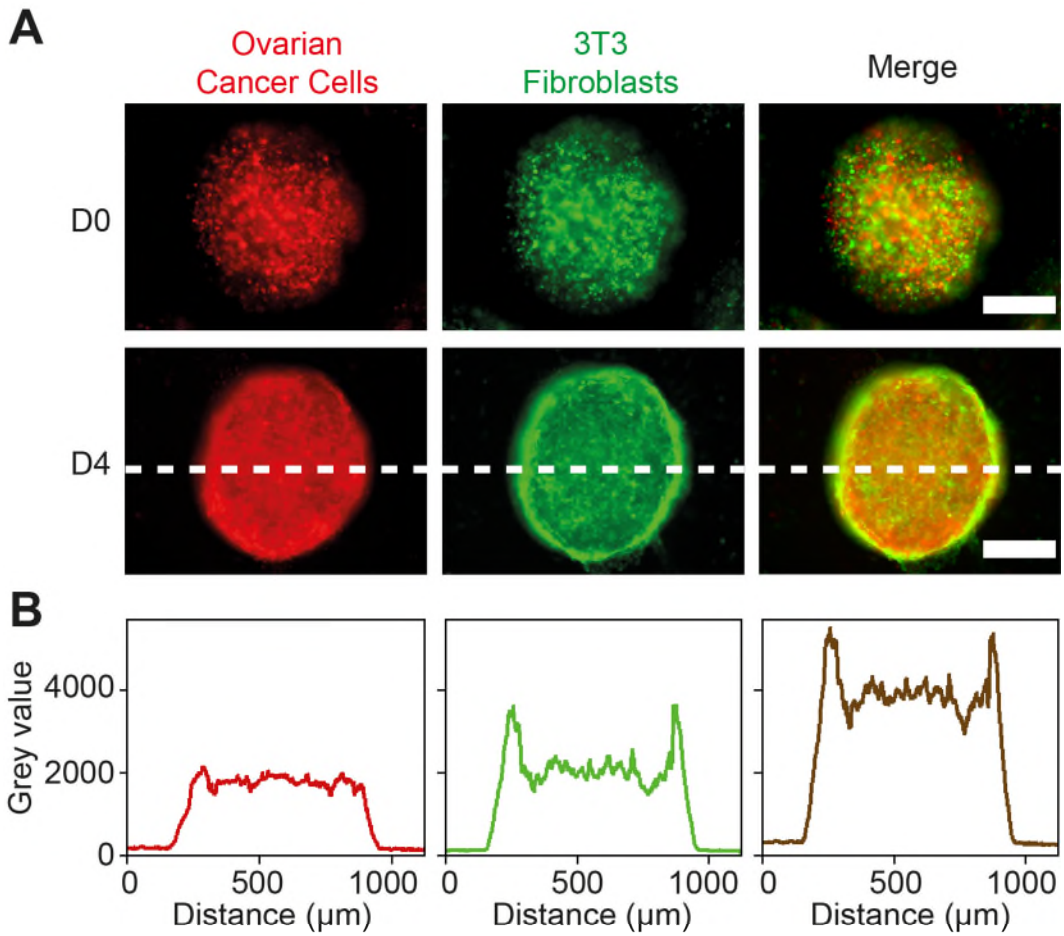


Figure 3.15. Core-shell structure formed by distinct cell migration patterns in co-culture 3D microtumours. (A) Representative epifluorescence images of co-culture 3D microtumours (50: 50 mixture of OVCAR-5/RFP and 3T3 fibroblasts) on D0 and D4 after fabrication. More than 15 co-culture 3D microtumours were imaged. Scale bar = 300 μm. (B) Fluorescence intensity profiles along the white dashed line across a co-culture 3D microtumour on D4. Left for OVCAR-5/RFP (red), middle for 3T3 fibroblasts (green), and right for merge (brown).

The spontaneous generated tumour core-fibroblast shell structure showed biological relevance to metastatic ovarian cancer. Zhang et al. reported that in patients with advanced-stage ovarian cancer, tumour cells that metastasised to omentum were surrounded by abundant fibroblasts[182]. Additionally, in

subcutaneous mouse models, fibroblasts injected intraperitoneally were specifically recruited by tumours and situated at the rims of ovarian tumours[183]. The successful recapitulation of *in vivo* spatial arrangements between tumour cells and fibroblasts emphasises the utility of 3D microtumour model for investigating how TME influences tumour progression.

3.6 Summary

In this chapter, we demonstrated the characteristics of 3D microtumours that enable them an ideal platform for drug screening. These microtumours can faithfully recapitulate key physiological features of tumours, for example, hypoxia and cytoskeleton arrangements, which have profound impacts on therapeutics responsiveness. This makes 3D microtumours outperform 2D cultures for applications like drug testing. Technically, the 3D microtumours produced by the microfluidic platform are uniform in size and composition, and they can be fabricated in large quantities, facilitating comparison among technical repeats. All these advantages together, allow 3D microtumour as an excellent model for screening potential therapeutics.

4 Modelling ovarian cancer minimal residual disease using 3D microtumours

4.1 Introduction

Several models, such as 2D monolayer cultures, 3D systems, and animals, have been used in disease modelling to investigate disease development, potential therapeutic regimens and interactions between tissues or organs[83, 184]. All of these models have their balances of feasibility, biological relevance to human and cost, which has been discussed in Section 1.3.

In this chapter, we used 3D microtumours to model ovarian cancer MRD, which represents the small number of tumour cells that survive chemotherapy treatment in patients (even in very responsiveness) and are able to re-initiate tumours. Due to the low number and scattered individual tumour cells[185], establishing *ex vivo* model of MRD directly from patients is extremely challenging. Considering the high recurrent rate of ovarian cancer and the difficulty in obtaining *ex vivo* models of MRD, an alternative *in vitro* model that can recapitulate key MRD features and be used for drug screening is clearly needed.

We first characterised our 3D microtumours to assess their feasibility as an MRD model. Key MRD features involve lipid metabolism, cancer cell stemness, and non-genetic heterogeneity (Section 1.2). A metabolically shift of energy source from glucose to fatty acid has been found in drug resistant tumour cells,

leading to upregulation of genes involved in lipid synthesis and metabolism[186, 187]. More specifically, MRD cells distinguish from naïve cells by upregulating fatty acid oxidation (FAO) related genes[39]. To assess whether our 3D microtumours could recapitulate these key MRD features, we performed transcriptomic analysis on both MRD and naïve 3D microtumours, aiming to validate these characteristics within our model.

Next, we tested two FAO inhibitors, etomoxir and perhexiline, on 3D microtumours to determine whether these compounds could specifically target MRD cells.

Etomoxir was originally used as a diabetic agent and then extended to an antianginal agent[188]. By irreversibly inhibiting carnitine palmitoyl transferase (CPT1), a mitochondrial enzyme, etomoxir impedes transport of fatty acids into mitochondria and subsequent β-oxidation[189]. In a study involving bladder cancer, etomoxir was demonstrated to suppress cell growth by arresting proliferative cells at G0/G1 phase and by altering the expression of genes related to fatty acids metabolism[190].

Perhexiline was first designed as an antianginal agent in 1970s for the treatment of cardiovascular diseases[191]. As a potent inhibitor of CPT1 and CPT2, perhexiline blocks the import of long-chain fatty acids into mitochondria, and thus reduces FAO[192]. In a study involving gastrointestinal cancer, perhexiline inhibited cell growth and induced apoptosis through decreasing FAO and the reduced form of nicotinamide adenine dinucleotide phosphate (NADPH). These effects led to an oxidising microenvironment and impaired the integrity of the mitochondria membrane[193].

Finally, we conducted transcriptomic analysis on the cells that survived FAO inhibitor treatments to gain an insight about possible targets to eradicate also these resistant cells.

Acknowledgement of collaboration

FAO inhibitor treatment, RNA-Seq libraries preparation and analysis, immunofluorescence staining and confocal microscope image processing in this chapter were finished by the author together with Dr Mara Artibani from Prof Ahmed Ahmed laboratory (Weatherall Institute of Molecular Medicine, University of Oxford).

4.2 Preparation of MRD-mimicking cells

For ovarian cancer patients, the standard clinical management procedures were shown in **Figure 4.1**. Diagnosed patients are administered the first-line treatment, which includes chemotherapy and/or debulking surgery. Due to the high recurrent rate – around 70-80% for epithelial ovarian cancer[194], extra attention should be paid to monitor relapses, which were driven by the MRD cells that are able to survive the first-line treatment.

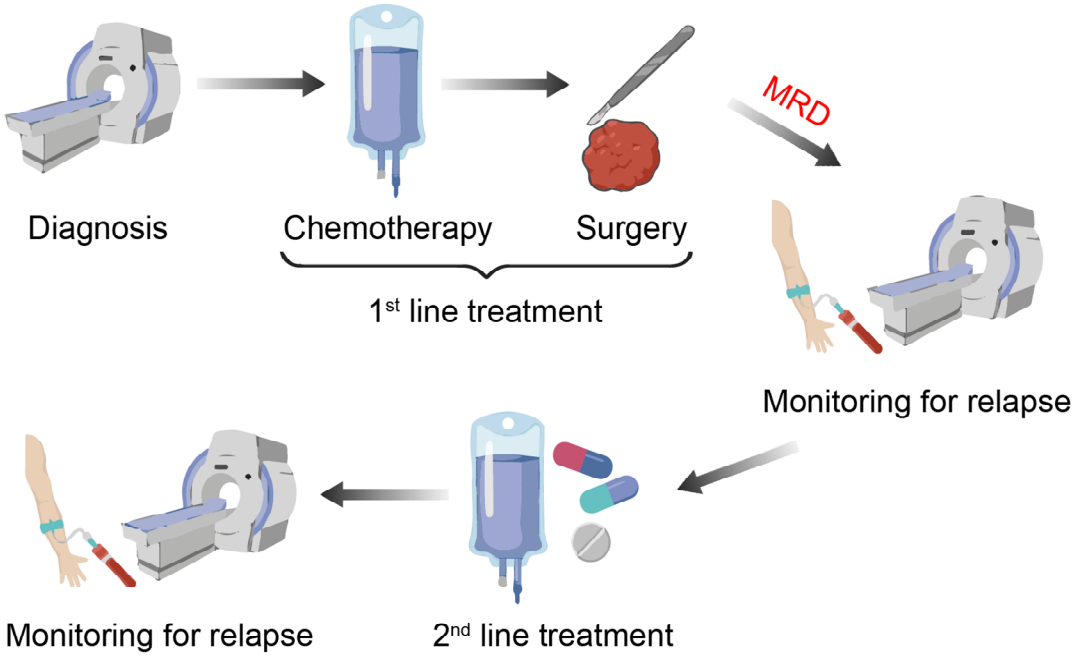


Figure 4.1. Schematic diagram of the standard clinical management of patients with ovarian cancer.

To mimic these drug resistant MRD cells *in vitro*, we administered carboplatin, a first-line chemotherapeutic commonly used for ovarian cancer patients[195], to treatment-naïve tumour cells to achieve 90% cell death. The surviving cells were reported to show MRD characteristics, such as upregulation in genes related to lipid metabolism, cancer stemness, and mesenchymal features[39]. Hence, these drug resistant cells were expanded to create a population of MRD-mimicking cells.

In this work, three ovarian cancer cell lines – OVCAR-5/RFP, OVCAR8 and OVCAR5 – were used to prepare the MRD-mimicking cells. It was necessary to optimise the carboplatin concentrations for each cell line individually. Specifically, the ovarian cancer cells were treated with either one or two doses of serial diluted carboplatin for two weeks. At the end of the treatment, the cells were quantified and normalised to the corresponding control groups (carboplatin concentration = 0). Based on the cell killing curves (**Figure 4.2**), we determined the optimised

concentration required to achieve 90% cell death for the preparation of MRD-mimicking cells.

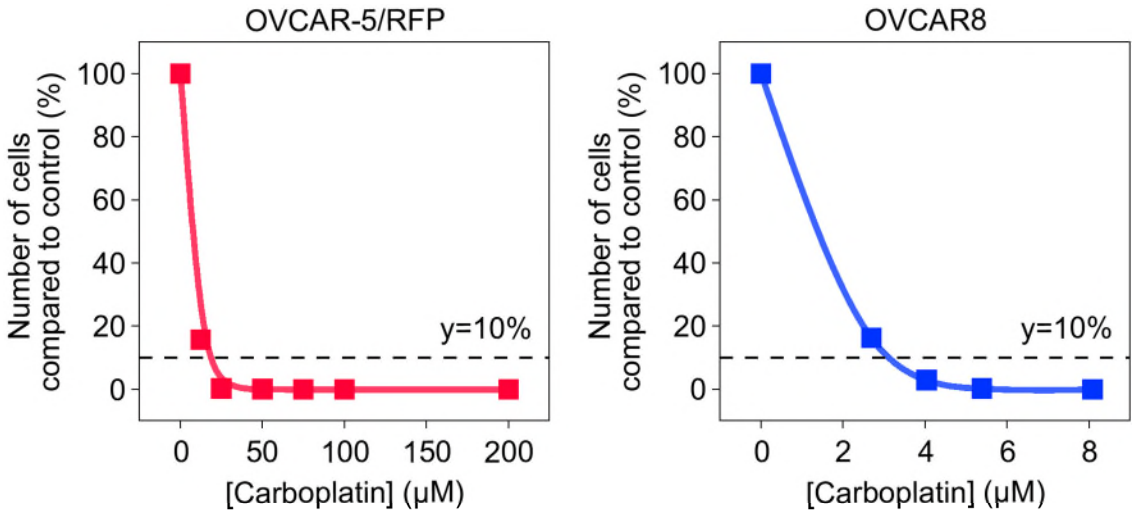


Figure 4.2. Killing curves for preparing MRD-mimicking cells. Normalised cell number of OVCAR-5/RFP (left) and OVCAR8 (right) cells after treated with serial dilutions of carboplatin for two weeks. Number of cells was normalised to corresponding control group with carboplatin concentration = 0.

Table 4.1. Optimised conditions for preparing MRD-mimicking cells.

Day	OVCAR-5/RFP	OVCAR8	OVCAR5
D0	14,000 cells per T-75 culture flask in drug-free medium	3,400 cells per T-75 culture flask in drug-free medium	14,000 cells per T-75 culture flask in drug-free medium
D1	25 μM carboplatin-containing medium	5.4 μM carboplatin-containing medium	8.1 μM carboplatin-containing medium
D7	25 μM carboplatin-containing medium	5.4 μM carboplatin-containing medium	-
D14	Remaining cells were collected and expanded for 2-14 days.		

The cell plating density, carboplatin concentration and drug doses used for each cell line are summarised in **Table 4.1**. Interestingly, even though the OVCAR-5/RFP and OVCAR5 cell lines only differ in the insertion of the

fluorescent protein, they showed dissimilar sensitivity to carboplatin. To obtain a 10% of viable cells left after 2 weeks of treatment, OVCAR-5/RFP required two doses of carboplatin, each at 25 μM; while OVCAR5 only needed one dose of carboplatin at 8.1 μM.

4.3 MRD characteristics in 3D microtumours

The MRD-mimicking and treatment-naïve cells were used for 3D microtumours preparation.

In this thesis, we first prepared the MRD-mimicking cells from treatment-naïve cells in 2D culture, and then used the MRD 2D cells to manufacture MRD 3D microtumours. An alternative approach would involve first preparing treatment-naïve 3D microtumours and then administering carboplatin to induce MRD within the 3D microtumour environment.

Nonetheless, employing the second method led to a substantial reduction in cell density within each microtumour. This reduction could impact cell proliferation and potentially trigger anoikis, as detailed in Section 2.2.3. Furthermore, this approach introduced variations in cell numbers within each MRD 3D microtumour, making it challenging to perform meaningful comparisons between the naïve and MRD microtumours.

To be noticed, minimising the time between the removal of carboplatin and the initiation of experiments involving these cells was suggested. While the upregulation of genes associated with lipid metabolism pathways persisted after carboplatin removal, the degree of increased expression tended to diminish over time[39]. Therefore, in order to maintain a relatively brief period of cell expansion

following the withdrawal of carboplatin, we prepared MRD 3D microtumours using MRD 2D cells, rather than starting from naïve 3D microtumours.

Transcriptomic analysis was performed to assess whether the 3D microtumours can recapitulate the MRD characteristics. We also compared the expression difference between clinical samples and *in vitro* models (2D and 3D).

4.3.1 Transcriptomic analysis

Transcriptomic analysis was performed on our *in vitro* models (2D cultures and 3D microtumours) for both naïve and MRD cells. Three cell lines, OVCAR-5/RFP, OVCAR8 and OVCAR5, were used for preparing *in vitro* models. We compared the RNA-Seq data from the *in vitro* models with the previously published libraries of clinical samples from patients with MRD.

Principal component analysis (PCA) (**Figure 4.3**) showed that the greatest differences among the samples primarily originated from various cell lines, which was entirely expected. By comparing the data from each individual cell line to the clinical samples, we found that generally naïve 2D cultures differed the most from clinical samples, while the MRD 3D microtumour exhibited the closest resemblance to clinical samples, regardless of the cell line used.

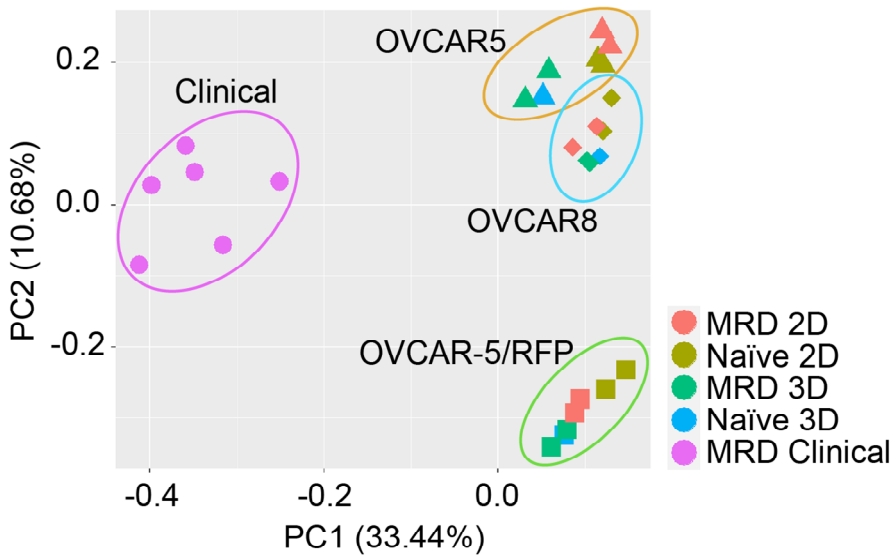


Figure 4.3. Principal component analysis (PCA) plot of RNA-Seq data from *in vitro* models and clinical samples. The PCA plot showed 2D cultures, 3D microtumours and the previously published libraries obtained from patients with MRD. Three cell lines, OVCAR-5/RFP, OVCAR8 and OVCAR5, were used for preparing *in vitro* models.

Differential expression analysis further supports the PCA results. Differentially expressed genes (DEGs) were identified between MRD *in vitro* models (2D or 3D) and MRD clinical samples. We observed that there were 14% fewer DEGs between MRD 3D microtumours and MRD clinical samples compared to the number of DEGs between MRD 2D cultures and MRD clinical samples (**Figure 4.4**A). Around 61% of the DEGs were shared between the two comparisons – 67% for upregulations and 49% for downregulations (**Figure 4.4**B, **Table 4.2**).

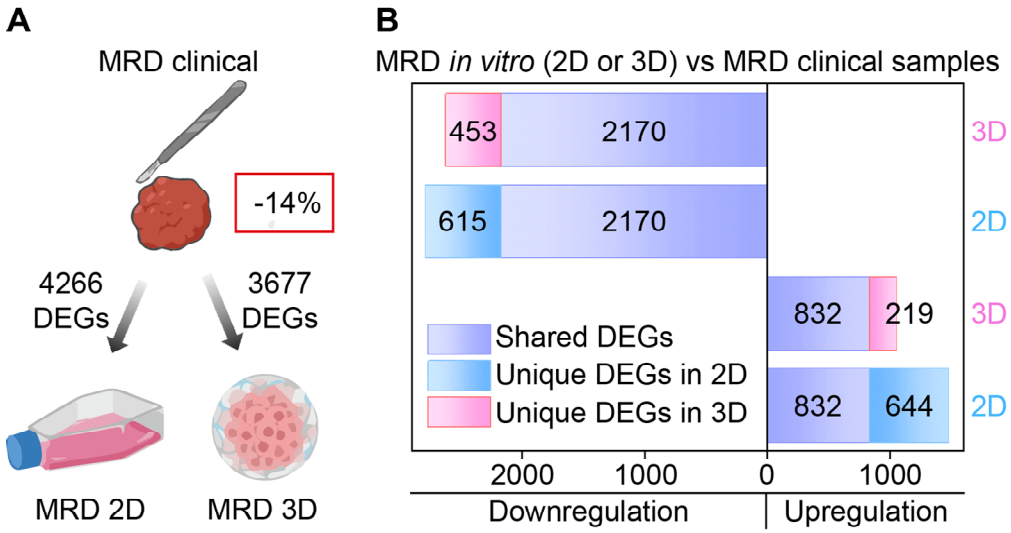


Figure 4.4. DEGs of MRD *in vitro* models compared to clinical samples. (A) Number of DEGs between MRD 2D cultures or MRD 3D microtumours compared to clinical samples. (B) Overlap of DEGs in MRD 2D cultures or MRD 3D microtumours compared to clinical samples for genes that were upregulated and downregulated *in vitro*.

Table 4.2. Summary of DEGs number of MRD *in vitro* models compared to clinical samples.

Number	Unique DEGs in MRD 3D	Unique DEGs in MRD 2D	Shared DEGs	Total DEGs
Upregulation	453	615	2170	3238
Downregulation	219	644	832	1695
Total	672	1259	3002	4933
Percentage	**Unique DEGs in MRD 3D**	**Unique DEGs in MRD 2D**	**Shared DEGs**	**Total DEGs**
Upregulation	14%	19%	67%	100%
Downregulation	13%	38%	49%	100%
Total	14%	26%	61%	100%

Pathway enrichment analysis was performed on the DEGs, with a specific focus on the upregulated DEGs unique to MRD 2D. These genes were enriched in pathways related to cell cycle and division (**Figure 4.5**). This discovery aligns with our earlier observations in Section 3.2.1, where we compared the transcriptomes of naïve ovarian cancer cells in 2D cultures and those in 3D microtumours (**Figure 3.5**, **Figure 3.6**).

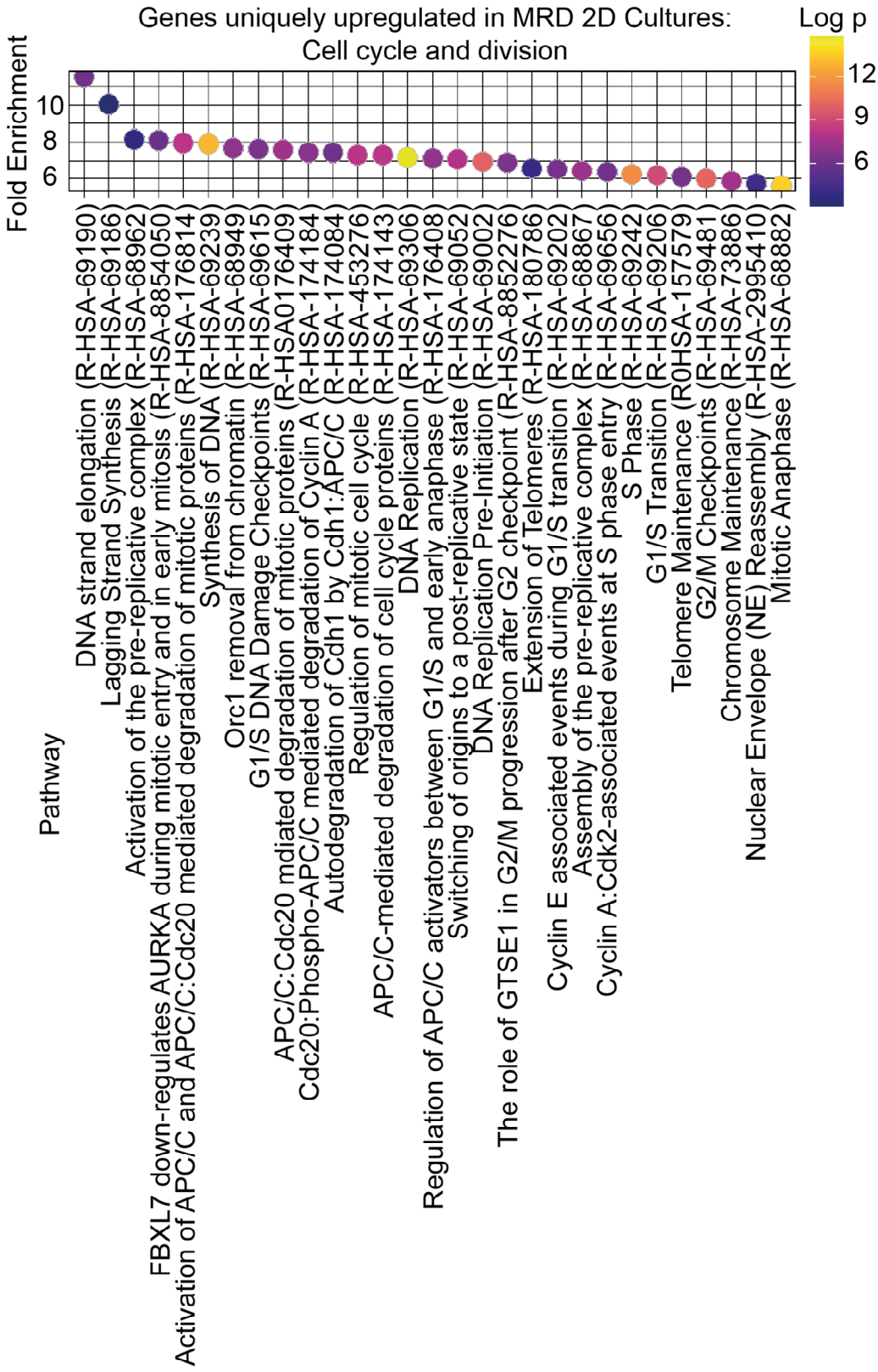


Figure 4.5. Pathway enrichment in MRD 2D: cell cycle and division. Dot plots showing pathways related to cell cycle and division were enriched among genes uniquely upregulated in MRD 2D compared to clinical samples.

4.3.2 Lipid transport and metabolism

When examining the DEGs that were uniquely upregulated in MRD 2D cultures compared to MRD clinical samples, we also found an enrichment of pathways related to metabolism based on carbohydrates and amino acids (**Figure 4.6**), which seems to suggest a different metabolic strategy from clinical samples.

Next, we directly compared transcriptomes between MRD 2D cultures and MRD 3D microtumours for the metabolism strategy. Genes related to lipid transport and metabolism (TOPPFUN Biological processes, GO:0033993) were significantly upregulated in 3D microtumours compared to 2D cultures (**Figure 4.7**). The upregulation of genes in MRD 3D microtumours is similar to the results originally found in MRD patients, regardless of cell line used.

Correlation analysis was performed to confirm the relationship of gene upregulation between 3D microtumours and clinical samples. With a focus on the genes involved in lipid metabolism, which were originally found in MRD patients, the expression level in MRD 3D microtumours correlated significantly with those in MRD patients (**Figure 4.8**). The Pearson's correlation coefficient was 0.99 with a p value smaller than 0.05 for both individual patient sample and pooled patient samples, indicating a strong and statistically significant correlation.

The results obtained from pathway enrichment analysis, gene expression levels and correlation analysis between 3D microtumours and clinical samples, collectively demonstrate that 3D microtumours exhibit an upregulation of genes involved in metabolism strategies similar to those seen in clinical samples. Therefore, the 3D microtumours outperform the 2D cultures as an *in vitro* model to mimic lipid transport and metabolism in MRD patients.

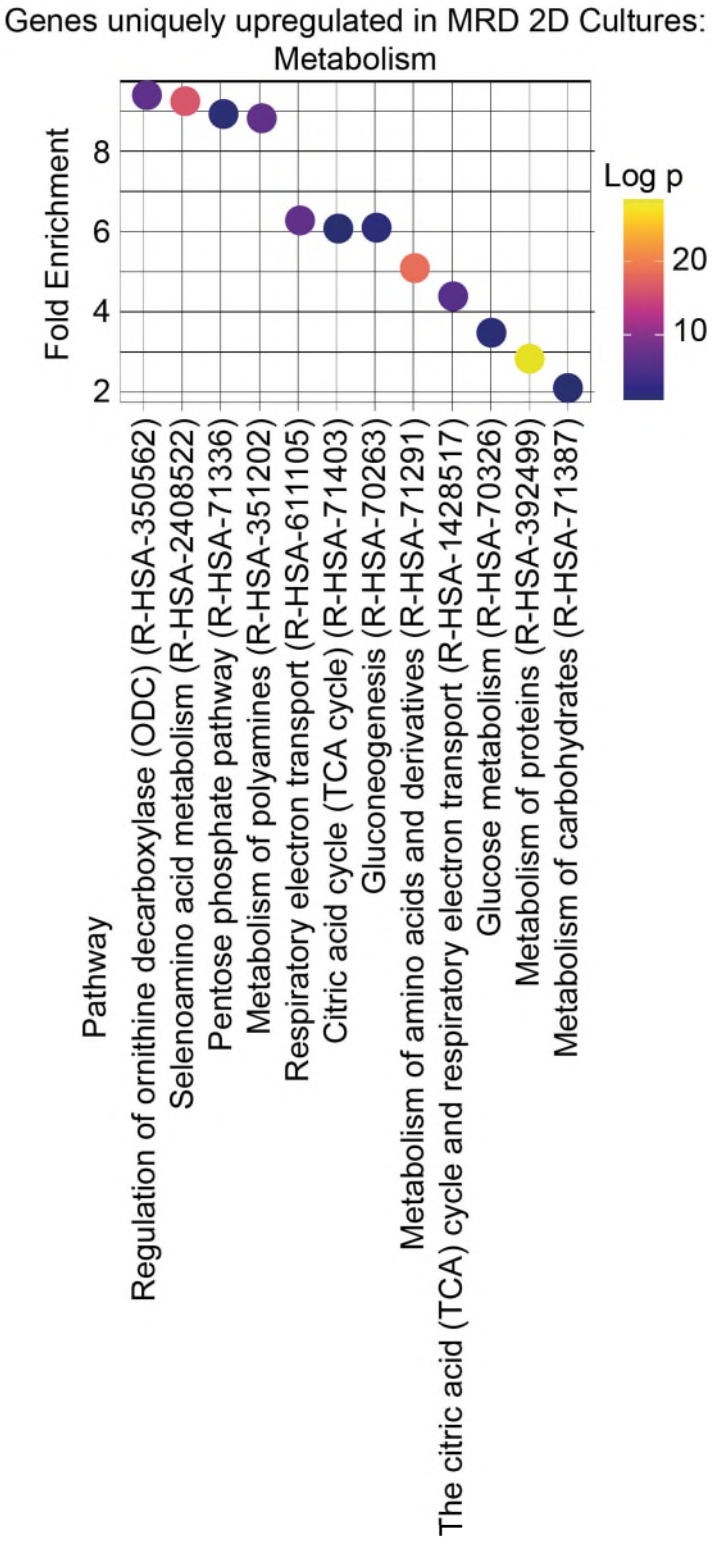


Figure 4.6. Pathway enrichment in MRD 2D: metabolism. Dot plots showing pathways related to metabolism were enriched among genes uniquely upregulated in MRD 2D compared to clinical samples.

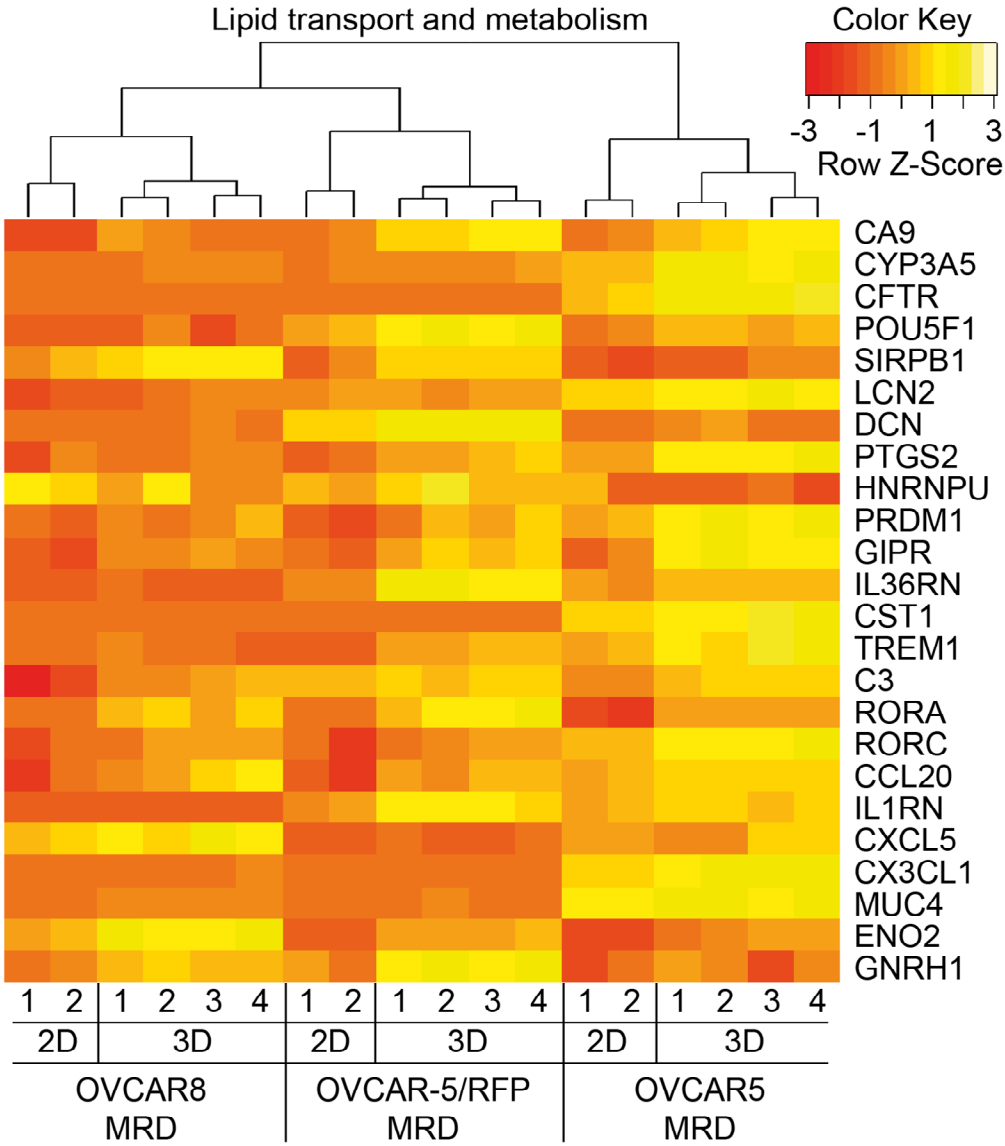


Figure 4.7. Heatmap showing the expression of genes in 3D microtumours and 2D cultures involved in lipid transport and metabolism. The gene list was derived from TOPPFUN Biological processes, response to lipid, GO:0033993.

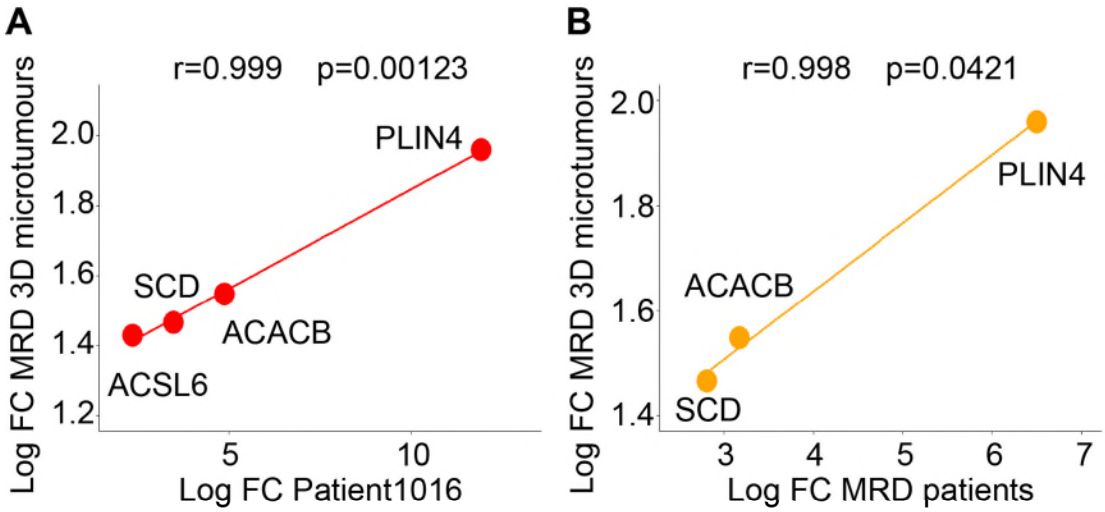


Figure 4.8. Scatterplots showing the $\log_2$ fold change (log FC) of genes involved in lipid metabolism. A positive correlation is observed between their upregulation in the MRD 3D microtumours (3D/2D expression ratios) compared to (A) the MRD patient 1016 or (B) the pooled MRD exceptional responders (post/pre chemo expression ratios). Pearson's correlation coefficient = r.

4.3.3 ABC transporters and TIC/CSC markers

The ATP-binding cassette (ABC) transporters belong to the family of membrane proteins, which have been revealed to be associated with the development of multidrug resistance in cancers[196, 197]. These transporters are responsible for increasing the efflux of chemotherapeutic drugs from tumour cells, which ultimately reduces the effectiveness of these drugs[198]. Tumour initiating cell (TIC)/cancer stem cell (CSC), a population of cells showing stem cell-like properties, contribute to tumour malignancies and recurrences[199, 200]. These cells are characterised by the ability to self-renew, maintain in undifferentiated states, develop drug resistance, and repopulate the bulk tumour[201].

The increased expression of ABC transporters and TIC/CSC markers has been identified as features of MRD[39]. These features are observed in post-chemotherapy tumour cells[202], and contribute to the relapse of ovarian cancer. A gene list associated with ABC/TIC/CSC, previously identified in MRD ovarian

patients, showed significantly higher expression of ABC transporters (ABCA12, ABCB5, ABCA9, ABCA6, ABCA10, ABCA8) and TICs markers (ALDH1L1, ALDH1A1, ALDH2)[39]. This gene signature was found to be overexpressed in MRD 3D microtumours compared to MRD 2D cultures (**Figure 4.9**).

We also confirmed the overexpression of the marker, aldehyde dehydrogenase ALDH3A1, in 3D microtumours by immunofluorescence staining. ALDH3A1 is of interests not only because it is a known TIC/CSC marker, but also because it participates in FAO to supply energy to tumour cells[203]. In a study of gastric cancer, ALDH3A1 contributed to the production for around 40% of reduced form of nicotinamide adenine dinucleotide (NADH), which was used to generate ATP for conversion of fatty aldehydes to fatty acids and downstream FAO in cancer cells[204]. The expression of ALDH3A1 is found specifically in MRD 3D microtumours, but not in naïve 3D microtumours (**Figure 4.10**).

Therefore, the TIC/CSC feature was exclusively represented by MRD 3D microtumours, but not by naïve 3D microtumours.

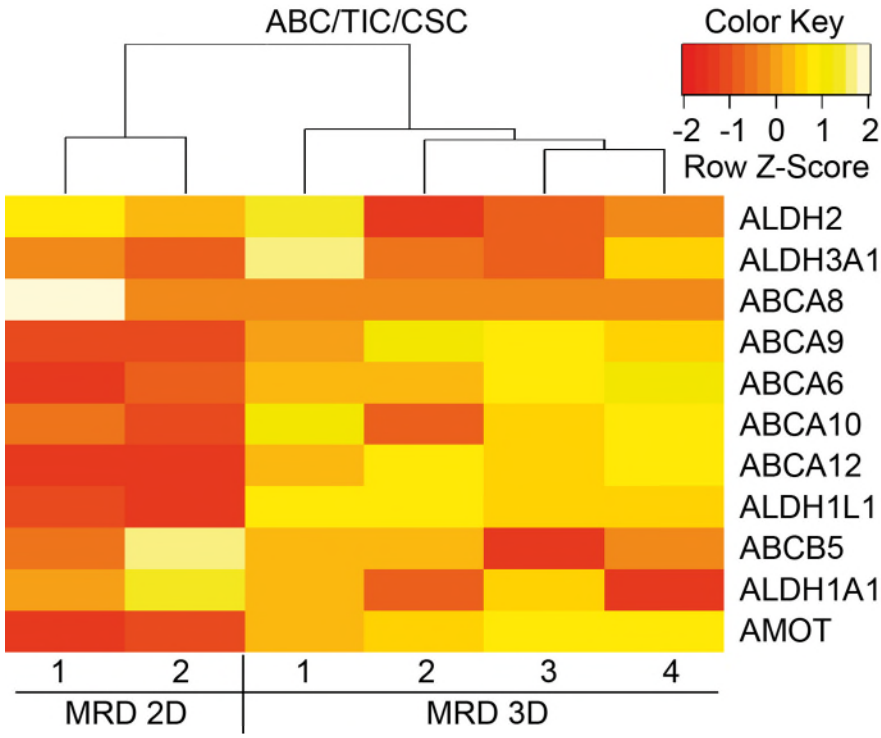


Figure 4.9. Heatmap showing the expression of genes in 3D microtumours and 2D cultures encoding ABC transporters and TIC/CSC markers.

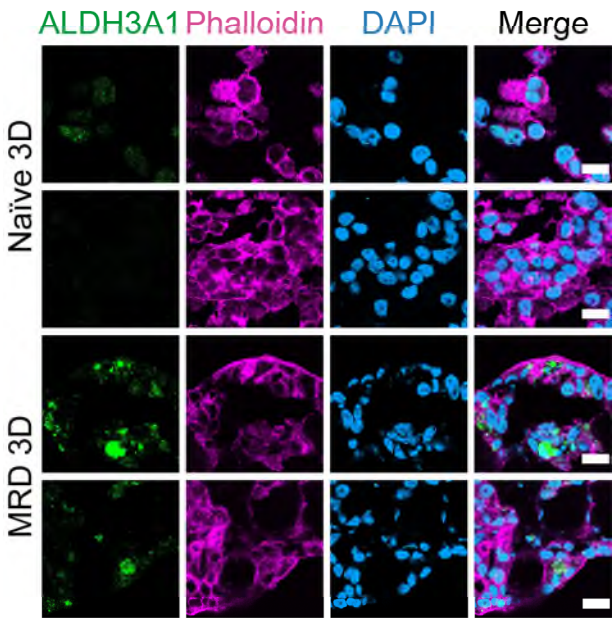


Figure 4.10. 3D microtumours stained with TIC/CSC marker: ALDH3A1. Confocal images of 3D microtumours at D10 stained with the TIC/CSC marker ALDH3A1 (green). The cells were also stained with phalloidin (pink) and DAPI (blue). Scale bar = 20 µm.

4.3.4 Non-genetic heterogeneity

Heterogeneity describes the variation regarding one or more specific traits among cell populations, rather than among individual cells[205]. It can be classified as genetic heterogeneity and non-genetic heterogeneity. In cancer biology, genetic heterogeneity refers to the genome sequence differences, which are promoted by genomic instability of the tumour cells[206]. Non-genetic heterogeneity, also known as phenotypic heterogeneity, refers to the cells share the same genome, but display phenotypic variability[205]. These phenotypic variations, which arise from gene expression noise, are enduring, often inheritable, and are suggested to contribute to somatic evolution[207]. As a result, the non-genetic heterogeneity can influence metastasis, drug resistance and tumour progression[207, 208]. To be noticed, the term “epigenetic” needs to be distinguished from “non-genetic”: “epigenetic” emphasises on covalent modifications of DNA and chromatin[207]; while “non-genetic” focuses on phenotypic variants from isogenic populations[205].

Hu et al. previously reported a measure of non-genetic heterogeneity for ovarian cancer. They surveyed single cell transcriptomes of healthy fallopian tube epithelium cells (the cell of origin of ovarian cancer) and analysed their molecular signatures. Based on the molecular signatures from normal fallopian tube epithelium cells, they identified five different cell states to represent non-genetic heterogeneity, and used them to predict cancer behaviour accurately. The five cell states are: cell cycle (enriched in three pathways: cell cycle, DNA repair, and chromatin remodelling), EMT (enriched in extracellular matrix pathway and high expression of a regulator of G protein signalling), KRT17 (upregulation of major histocompatibility complex class II genes, cytokeratins

(KRT17 and KRT23), aldehyde dehydrogenases, and CDKN1A), differentiated (enriched in RNA synthesis and transport pathways) and ciliated (high expression of secretory cell marker KRT7 and ciliated cell marker CAPS)[209].

Among these cell states, EMT is of most interest since it is correlated with cancer relapse and poor prognosis significantly[210, 211]. Phenotypic changes from epithelial to mesenchymal attributes enable cells to be motile and invasive[212]. Twist, a key EMT inducer, increases expression of CSC markers, such as Bmi1, and thus promotes tumour progression[213].

The RNA-Seq datasets for our 3D microtumours and 2D cultures were used for deconvolution analysis to measure the non-genetic heterogeneity. The results (**Figure 4.11**) showed that all the five cell states identified from clinical samples of fallopian tube epithelium cells can be found in 3D microtumours. On the other hand, only one to three cell states appear in 2D cultures, depending on the cell line. The most abundant cell state in 2D cultures falls into the cluster related to cell cycle, which is consistent with the results from DEGs (**Figure 3.5**) and pathway enrichment analysis (**Figure 4.5**). The EMT cell state is observed more frequently in MRD 3D microtumours than in naïve 3D microtumours, reflecting the drug-resistant state of MRD and their involvement in cancer relapse.

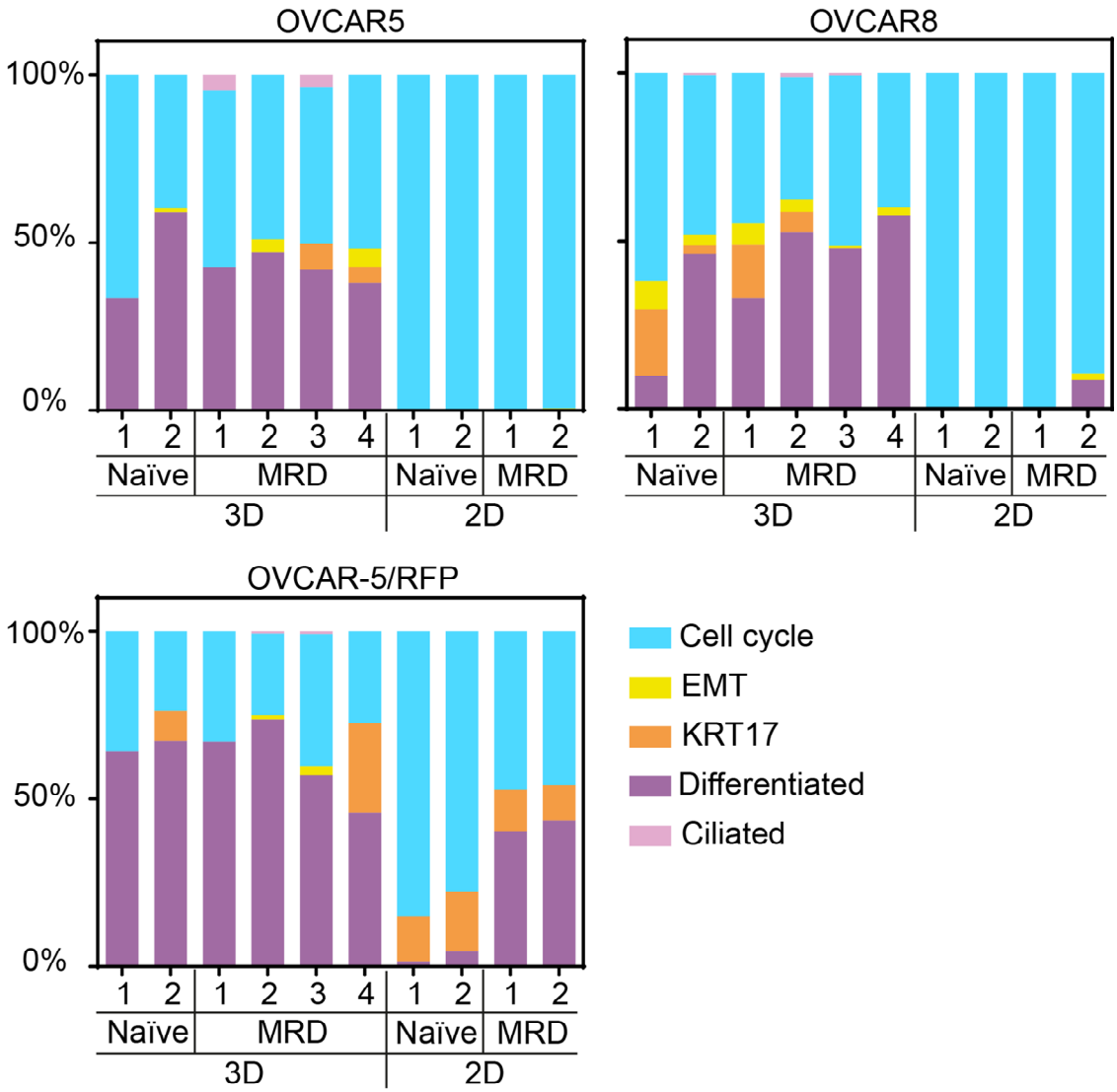


Figure 4.11. Deconvolution analysis for 3D microtumours. Stacked bar plots visualizing the deconvolution results of 3D microtumours and 2D cultures produced from OVCAR5, OVCAR8 and OVCAR-5/RFP. The y axis represents the percentage of each cell state in a given sample. Colours of the bars denote the 5 cell states as shown in the legend.

We also performed the deconvolution analysis on a published dataset, which consists of ovarian cancer cell lines grown in 2D cultures[214]. Out of the 37 samples, 14 cell lines were derived from primary solid tumours, 7 were generated from tumour source of ascites fluid, 4 were established from mouse xenografts, and the remaining 12 were standard ovarian cancer cell lines[214]. The standard cell lines generally display cell cycle as the only cell state they possess. Those

cell lines derived from primary solid tumours, ascites fluid and xenograft, display one to three cell states, with cell cycle as the predominant one.

Although cell lines from primary tumours display more cell states than the standard cell lines, these 2D cultures are still dominated by the cell cycle state. Failing to recapitulate the essential features of chemotherapy resistant cells remains a ubiquitous disadvantage of 2D cultures.

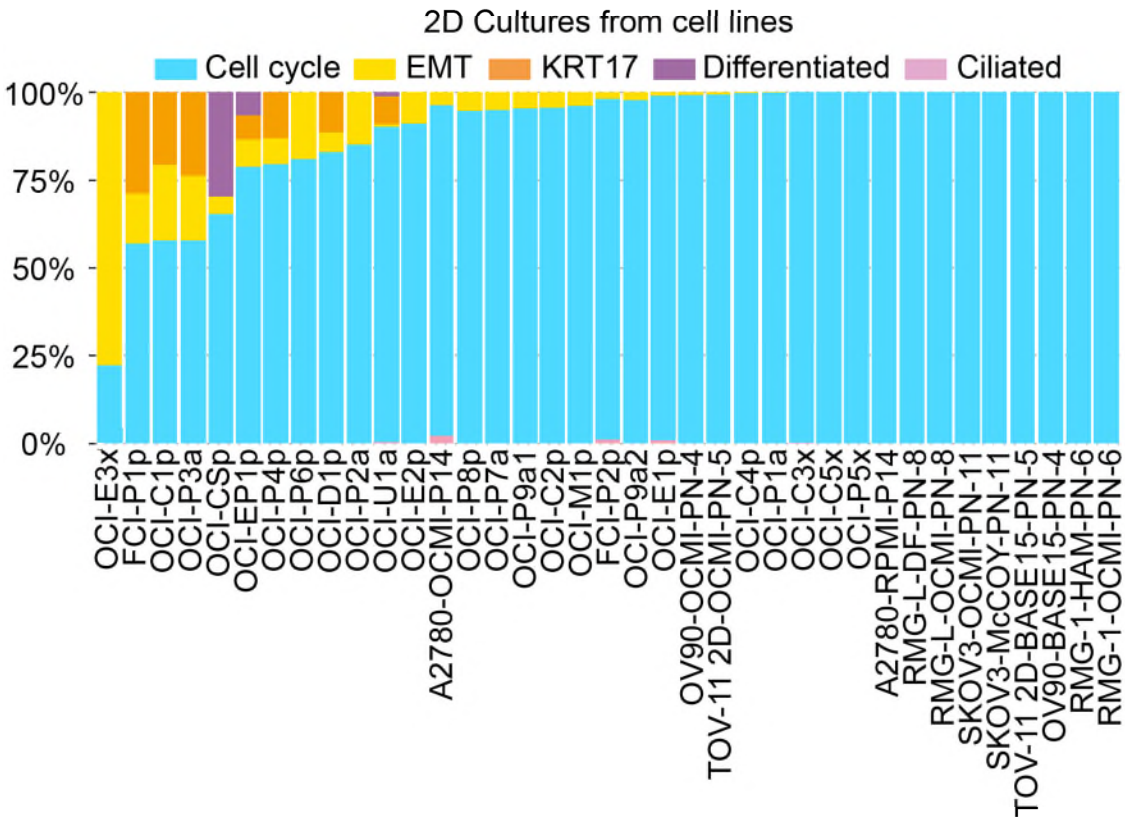


Figure 4.12. Deconvolution analysis for 2D cultures from literature. Stacked bar plots visualizing the deconvolution results of a publicly available dataset of 37 additional ovarian cancer cell lines grown in 2D cultures. The y axis represents the percentage of each cell state in a given sample. Colours of the bars denote the 5 cell states as shown in the legend.

In addition to 2D cultures of ovarian cancer cell lines, we also performed deconvolution analysis on a published dataset of 18 patient-derived organoids from HGSOC tissues[66]. On average, the organoids exhibit more cell states than

2D cultures, with a higher proportion of differentiated cluster and lower fraction of cell cycle. Occasional sample exhibits cell cycle as the only cell state and little representation of the ciliated molecular signature.

3D microtumours made from cell lines present similar deconvolution analysis results to organoids derived from patient samples, and are more representative for the non-genetic heterogeneity of ovarian cancer than 2D cultures.

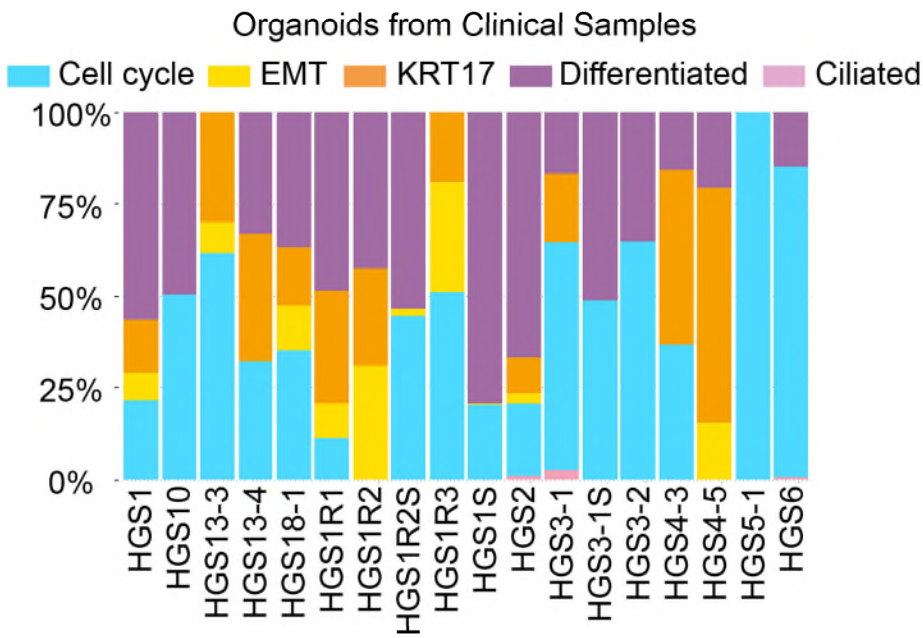


Figure 4.13. Deconvolution analysis for organoids from literature. Stacked bar plots visualizing the deconvolution results of a publicly available dataset of organoids established from clinical samples of HGSOC. The y axis represents the percentage of each cell state in a given sample. Colours of the bars denote the 5 cell states as shown in the legend.

Considered collectively, these data showed that the 3D microtumours successfully recapitulate all the key MRD features (including lipid transport and metabolism, CSC/TIC, and non-genetic heterogeneity, especially EMT), supporting the utilisation of 3D microtumour as a pragmatic model for ovarian cancer MRD.

4.4 FAO inhibitor responses

In the last section, transcriptomics and protein expression analysis confirmed that the 3D microtumours can faithfully recapitulate MRD characteristics of ovarian cancer. For the next step, we would like to find therapeutics that specifically target and eliminate MRD cells using the 3D microtumours.

Previous work by Artibani et al. showed that the pathways upregulated in MRD cells can be used as the therapeutic targets[39]. For instance, inhibiting the CPT1, an outer mitochondrial membrane enzyme, which transports long-chain fatty acids into the mitochondria, could specifically target cancer cells with a high FAO metabolism[215]. When treated with CPT1 inhibitors, etomoxir and perhexiline, MRD ovarian cancer cells in 2D cultures were found to experience more cell death (20 to 30%) than naïve cells[39].

To investigate the responses of MRD 3D models to FAO inhibitors and compare to the previous data of 2D cultures, we fabricated 3D microtumours with naïve and MRD cells from three ovarian cancer cell lines (OVCAR-5/RFP, OVCAR5 and OVCAR8). The preparation procedure of MRD cells was optimised in Section 4.2. The CPT1 inhibitors, etomoxir and perhexiline, were applied to 3D microtumours for a window of 10 days. Cell viability assay and bulk RNA-Seq were performed on the 3D microtumours at the end of the treatment (**Figure 4.14**).

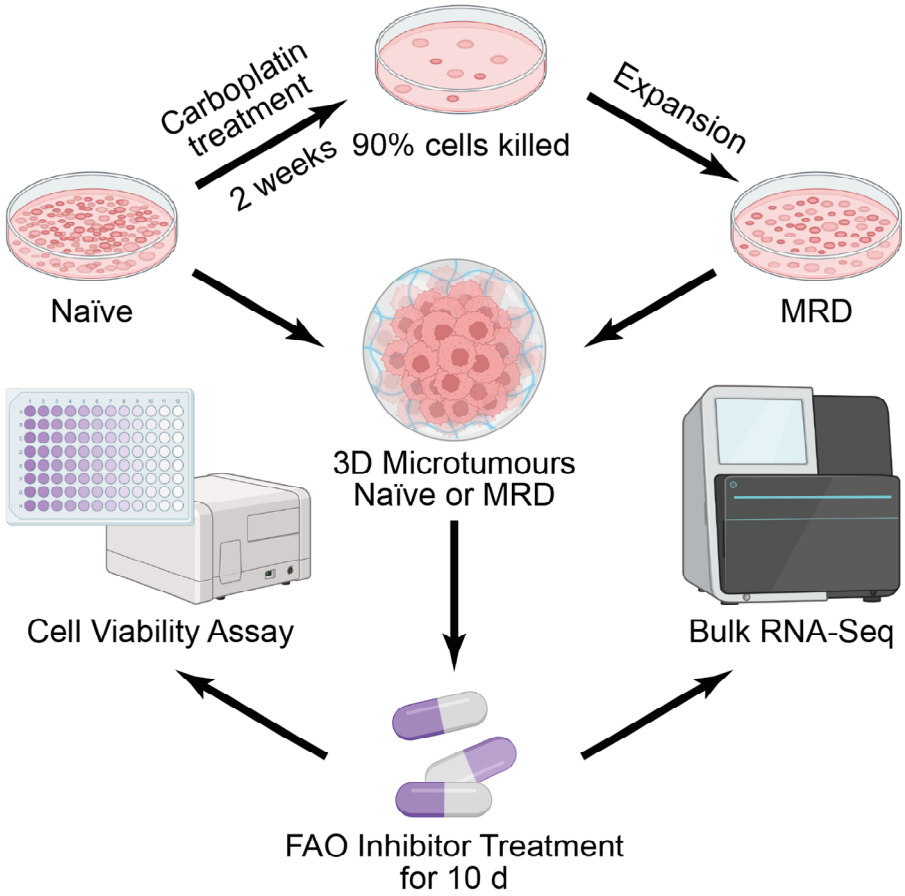


Figure 4.14. Schematic diagram of the treatment of naïve and MRD cells with therapeutics. The naïve ovarian cancer cells were treated with carboplatin for 2 weeks to achieve 90% cell killing and the surviving MRD cells were collected and expanded. 3D microtumours were fabricated (D0) from naïve cells or the corresponding MRD cells for each cell line. Next, FAO inhibitor treatment was applied to both types of microtumours for 10 days (D0 to D10). Cell viability assays were performed and mRNAs were extracted for bulk RNA sequencing on D10. The diagrams were created with BioRender.com.

Surprisingly, the responses of MRD 3D microtumours to etomoxir did not align with the results from MRD 2D cultures. For all the three cell lines used, etomoxir was unable to elicit significant cell killing effects to either naïve or MRD 3D microtumours (**Figure 4.15**, **Table 4.3**). In OVCAR5 naïve and OVCAR8 naïve 3D microtumours, cell proliferation was even promoted in etomoxir treated group compared to the dimethyl sulfoxide (DMSO) control group (**Table 4.4**).

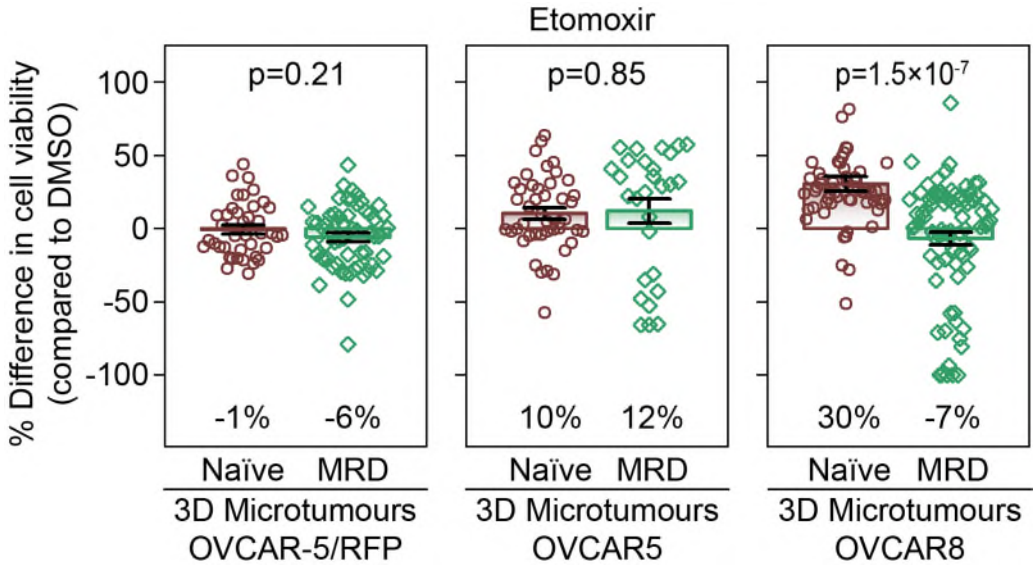


Figure 4.15. Responses of 3D microtumours to etomoxir. Cell viability changes of naïve and MRD 3D microtumours compared to a DMSO control after a 10-day treatment with 40 µM etomoxir (n = 28 to 85).

Table 4.3. Responses comparison between naïve and MRD 3D microtumours to etomoxir.

Cell line	Cancer type	N total	Difference in cell viability	SD	p-value
OVCAR-5/RFP	Naïve	40	-1%	19%	0.21 (n.s.)
	MRD	58	-6%	22%	
OVCAR5	Naïve	45	10%	25%	0.85 (n.s.)
	MRD	28	12%	43%	
OVCAR8	Naïve	60	30%	39%	1.5×10^{-7} (***)
	MRD	85	-7%	40%	

Table 4.4. Cell viability comparison between etomoxir treated and DMSO control group for 3D microtumours.

Cell line	Cell viability	DMSO	Etomoxir	p-value
OVCAR-5/RFP	Naïve	100 ± 19%	99 ± 19%	0.84 (n.s.)
	MRD	100 ± 23%	94 ± 22%	0.15 (n.s.)
OVCAR5	Naïve	100 ± 16%	110 ± 25%	0.019 (*)
	MRD	100 ± 34%	112 ± 43%	0.25 (n.s.)
OVCAR8	Naïve	100 ± 22%	130 ± 39%	1.49×10^{-6} (***)
	MRD	100 ± 59%	93 ± 40%	0.38 (n.s.)

On the contrary, MRD 3D microtumours were more sensitive than MRD 2D cultures in response to perhexiline. For all the three ovarian cancer cell lines used, naïve 3D microtumours treated with perhexiline showed a 6 to 15% reduction of cell viability compared to naïve 3D microtumours from DMSO control group; while MRD 3D microtumours treated with perhexiline exhibited a 54 to 97% decrease of cell viability compared to MRD 3D microtumours from DMSO control group (**Figure 4.16**, **Table 4.5**). Depending on cell line, perhexiline led to 48 to 82% more effective cell elimination in MRD 3D microtumours than in naïve counterparts (**Table 4.6**).

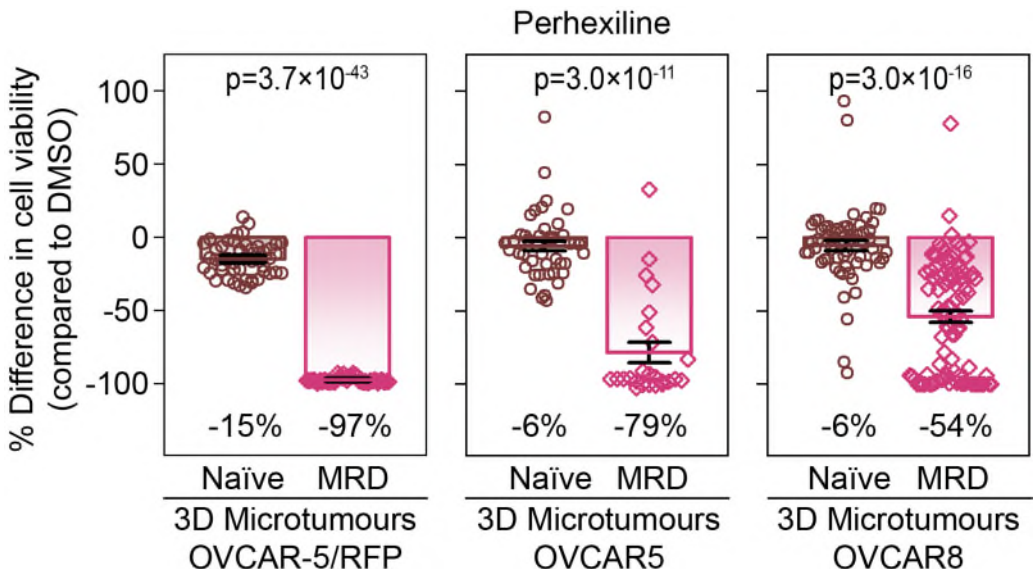


Figure 4.16. Responses of 3D microtumours to perhexiline. Cell viability changes of naïve and MRD 3D microtumours compared to a DMSO control after a 10-day treatment with 4 µM perhexiline (n = 25 to 93).

Table 4.5. Responses comparison between naïve and MRD 3D microtumours to perhexiline.

Cell line	Cancer type	N total	Difference in cell viability	SD	p-value
OVCAR-5/RFP	Naïve	48	-15%	12%	3.7×10^{-43} (***)
	MRD	54	-97%	2%	
OVCAR5	Naïve	44	-6%	23%	3.0×10^{-11} (***)
	MRD	25	-79%	35%	
OVCAR8	Naïve	61	-6%	27%	3.0×10^{-16} (***)
	MRD	93	-54%	38%	

Although both etomoxir and perhexiline are CPT1 inhibitors, perhexiline also targets CPT2, which locates at the inner membrane of mitochondria to mediate fatty acids transportation[216]. This possibly contributes to the differential efficacy of etomoxir and perhexiline towards 3D microtumours and 2D cultures.

Table 4.6. Killing effect comparison between naïve and MRD 3D microtumours.

Difference in cell viability (compared to DMSO)		Naïve	MRD	Δ = Naïve−MRD
Etomoxir	OVCAR-5/RFP	-1%	-6%	5%
	OVCAR5	10%	12%	-2%
	OVCAR8	30%	-7%	37%
Perhexiline	OVCAR-5/RFP	-15%	-97%	82%
	OVCAR5	-6%	-79%	73%
	OVCAR8	-6%	-54%	48%

4.5 Transcriptomes FAO inhibitor-resistant 3D microtumours

To acquire deeper insights into two key aspects: (1) the reason behind the ineffectiveness of etomoxir in 3D microtumours while perhexiline showed efficacy in the same model, (2) the potential pathways contributing to resistance against both etomoxir and perhexiline, we performed transcriptomic analysis on cells extracted from MRD 3D microtumours. This analysis involved a comparison of the transcriptomes between cells that had survived the inhibitor treatments and cells from the DMSO control group.

From the differential analysis, we found that, regardless of the cell line, the etomoxir-resistant cells upregulated the following genes: CPT1A, the long-chain fatty-acid- coenzyme A (CoA) ligase (ACSL5), the very long-chain specific acyl-CoA dehydrogenase (ACADVL), and the pyruvate dehydrogenase kinase (PDK4) (**Figure 4.17**). Immunofluorescence staining results confirmed the overexpression of CPT1 in etomoxir-resistant MRD 3D microtumours compared to DMSO control (**Figure 4.18**).

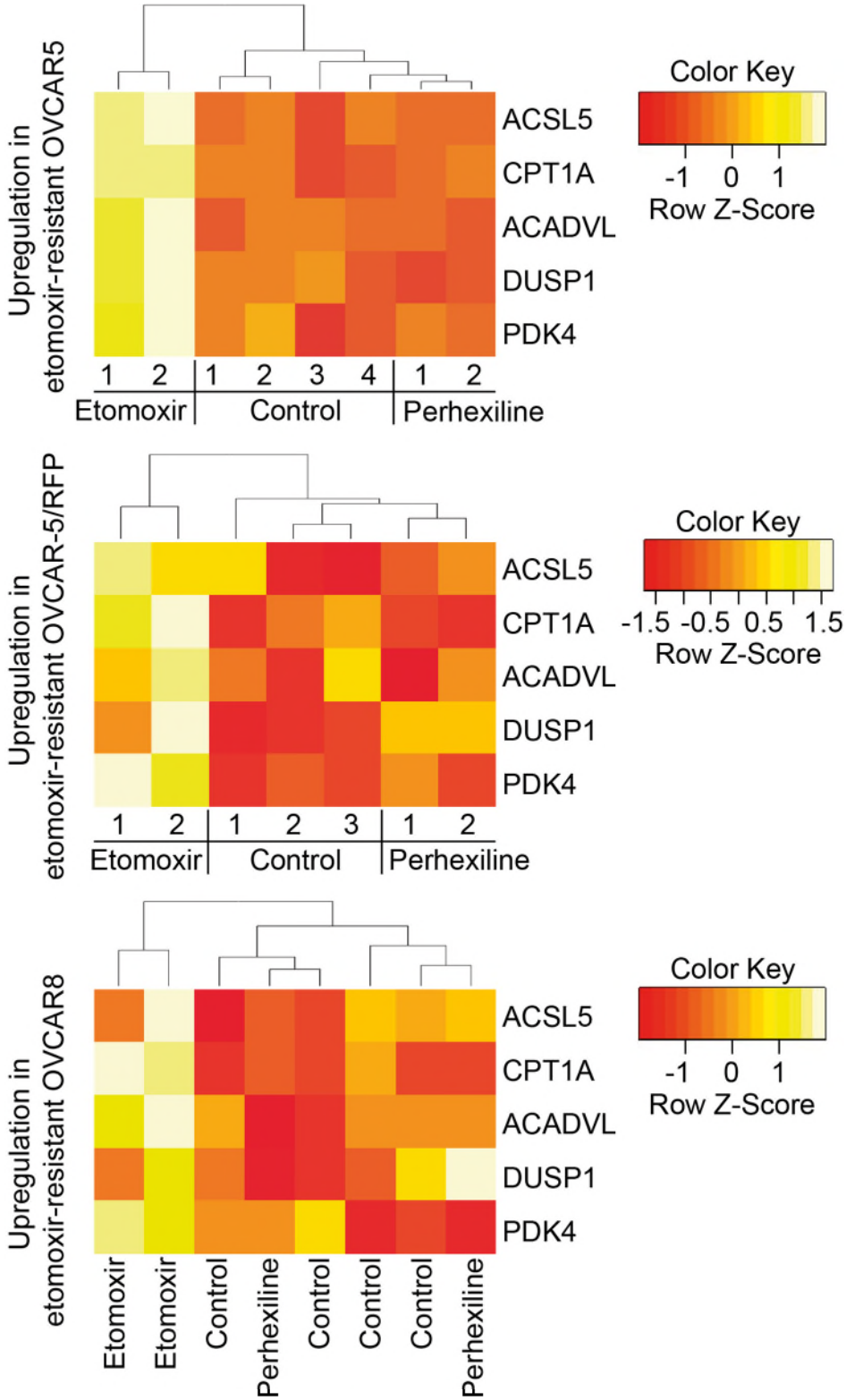


Figure 4.17. Genes upregulated in etomoxir-resistant MRD 3D microtumours. Heatmaps of DEGs upregulated in etomoxir-resistant MRD 3D microtumours composed of OVCAR5 (top), OVCAR-5/RFP (middle) and OVCAR8 (bottom).

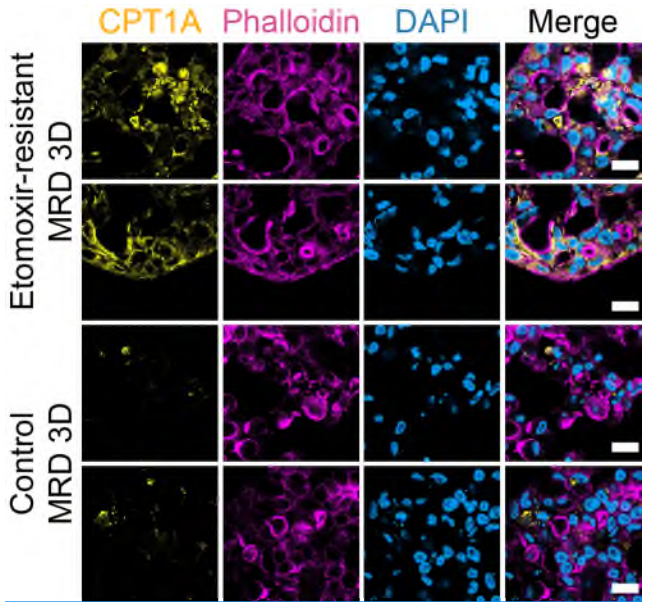


Figure 4.18. Etomoxir-resistant 3D microtumours stained with FAO marker. Confocal images of 3D microtumours (3D MT) at D10 stained with the FAO marker CPT1A (yellow). The cells were also stained with phalloidin (pink) and DAPI (blue). Scale bar = 20 μm.

CPT1A, the most ubiquitous isoform of CPT1, is responsible for transporting fatty acids into mitochondria for further metabolism[217]. ACSL5 locates in the outer membrane of mitochondria and participates in triglyceride synthesis and fatty acid degradation through esterification of long-chain fatty acids[218, 219]. ACADVL encodes the enzyme called very-long-chain acyl-CoA dehydrogenase (VLCAD), which locates in the mitochondrial membrane and is involved in the first-step of β-oxidation to activate fatty acids composed of 14 to 20 carbons[220-222]. PDK4 locates in the mitochondrial matrix and inhibits the activity of pyruvate dehydrogenase, resulting in a switch of metabolic strategy from glucose to fatty acids[223, 224]. More importantly, Wang et al. reported that overexpression of PDK4 promotes cancer cell stemness, enhances drug resistance, and relates to poor prognosis in ovarian cancer[225].

All of the above-mentioned genes are associated with FAO. Upregulation of these genes indicates that in response to CPT1 inhibition induced by etomoxir,

the cells upregulated other members of the FAO pathway to acquire energy from lipid oxidation. This may partially account for the failure of etomoxir to induce cytotoxicity in MRD 3D microtumours.

Due to the powerful cell killing effect of perhexiline towards MRD 3D microtumours, considerable low number of cells survived the treatment, which makes extracting sufficient RNA for libraries preparation challenging. Nevertheless, once we were successful, a distinct gene signature from etomoxir-resistant MRD 3D microtumours was revealed for the RNA-Seq analysis, even though it was still associated with lipid metabolism.

Depending on the cell line used, the perhexiline-resistant MRD 3D microtumours elevated the expression of at least 3 to 5 of the following genes: the long-chain-fatty-acid-CoA ligase ACSL1, the fatty acid synthase (FASN), the stearoyl-CoA desaturase (SCD) and the aldo-keto reductases (AKR) AKR1B10 and AKR1C2 (**Figure 4.19**). Immunofluorescence staining results confirmed the overexpression of FASN, SCD, AKR1B10 and AKR1C2 in perhexiline-resistant MRD 3D microtumours compared to DMSO control (**Figure 4.20**).

ACSL1, one of the five members of the ACSL family of CoA synthetases, locates on outer membrane of mitochondria and converts fatty acids to acyl-CoAs for β-oxidation[226-228].

FASN, which locates in the cytosol (type I FASN) or mitochondria (type II FASN), is involved in the *de novo* synthesis of fatty acids from glucoses[229]. Unlike normal cells, which obtain fatty acids exogenously, tumours cells acquire fatty acids both exogenously and from *de novo* synthesis via FASN[230]. *De novo* synthesised fatty acids nearly composed all of the triacylglycerol fatty acids in tumour cells[230].

SCD locates on the membrane of endoplasmic reticulum and reduces saturated fatty acids to monounsaturated fatty acids[231]. Overexpression of SCD was showed to increase cancer stemness, promote EMT, enhance metastatic potential in gastric cancer[232].

Both AKR1B10 and AKR1C2 belong to the AKR superfamily, which consists of 16 families, such as AKR1, and can be further divided into subfamilies, such as subfamily B[233]. They primarily locate in the cytosol and catalyses redox reaction among various substrates, for example, glucose, steroids, and lipid peroxidation products[234]. Overexpression of AKR1B10 in metastatic breast cancer caused increased utilisation of FAO[235]. Upregulation of AKR1C2 resulted in the development of anticancer drug resistance and was associated with poor prognosis for lung, breast and prostate cancer[236].

Similar to what was found in etomoxir-resistant cells, the genes upregulated in perhexiline-resistant MRD 3D microtumours were associated with lipid metabolism. The overexpressed proteins in etomoxir-resistant cells mostly locate in the mitochondria and are involved primarily in FAO. On the other hand, genes upregulated in perhexiline-resistant cells seem to have more complicated functions and involve multiple pathways. Moreover, the heatmaps DEGs showed a more pronounced overexpression of genes in etomoxir-resistant cells than in perhexiline-resistant cells – especially for perhexiline-resistant OVCAR8 and OVCAR-5/RFP, the gene expression difference is not that apparent among perhexiline, etomoxir and control group (**Figure 4.19**).

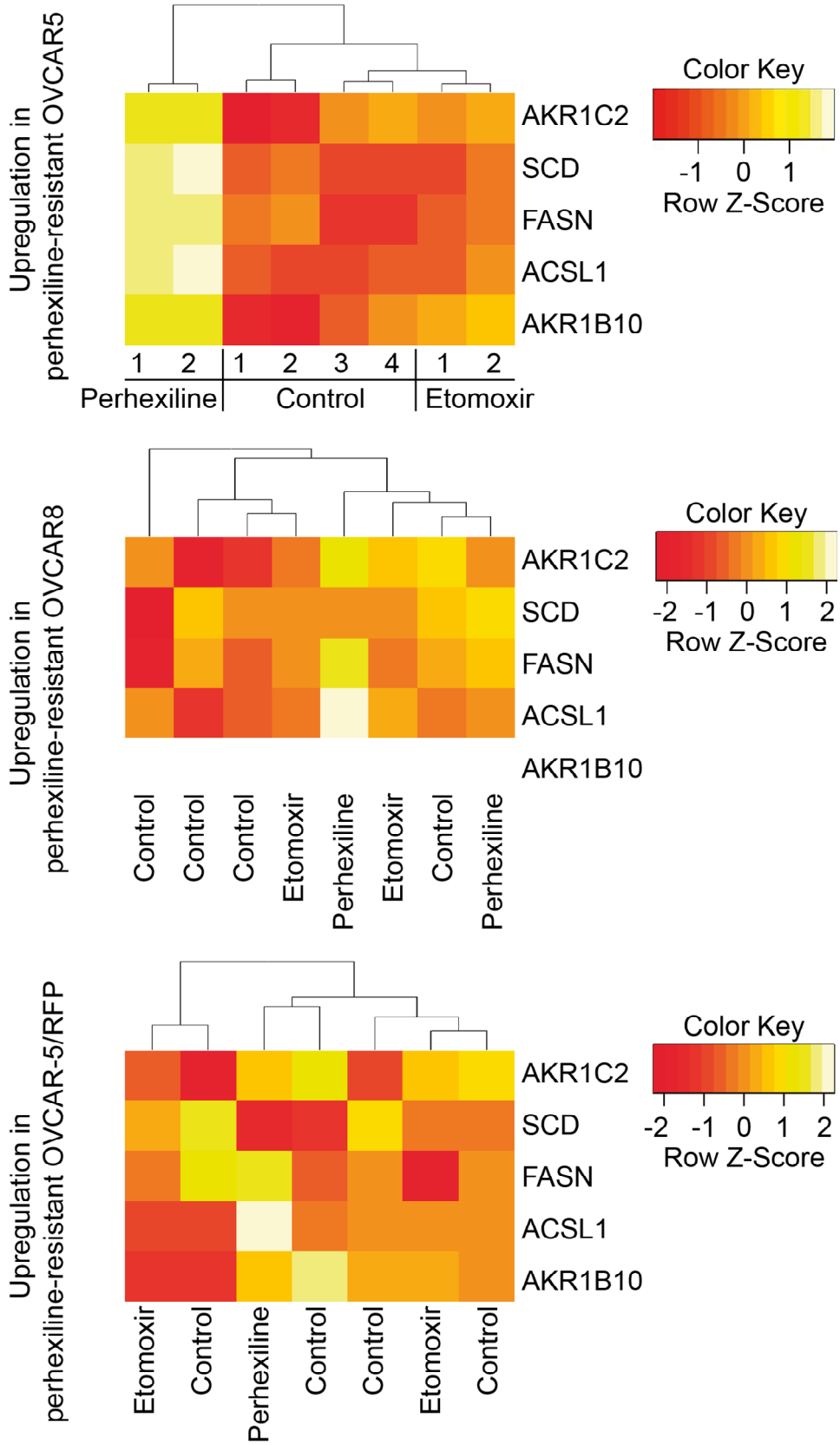


Figure 4.19. Genes upregulated in perhexiline-resistant MRD 3D microtumours. Heatmap of DEGs upregulated in perhexiline-resistant MRD 3D microtumours composed of OVCAR5 (top), OVCAR8 (middle, OVCAR8 cells do not express AKR1B10), and OVCAR-5/RFP (bottom).

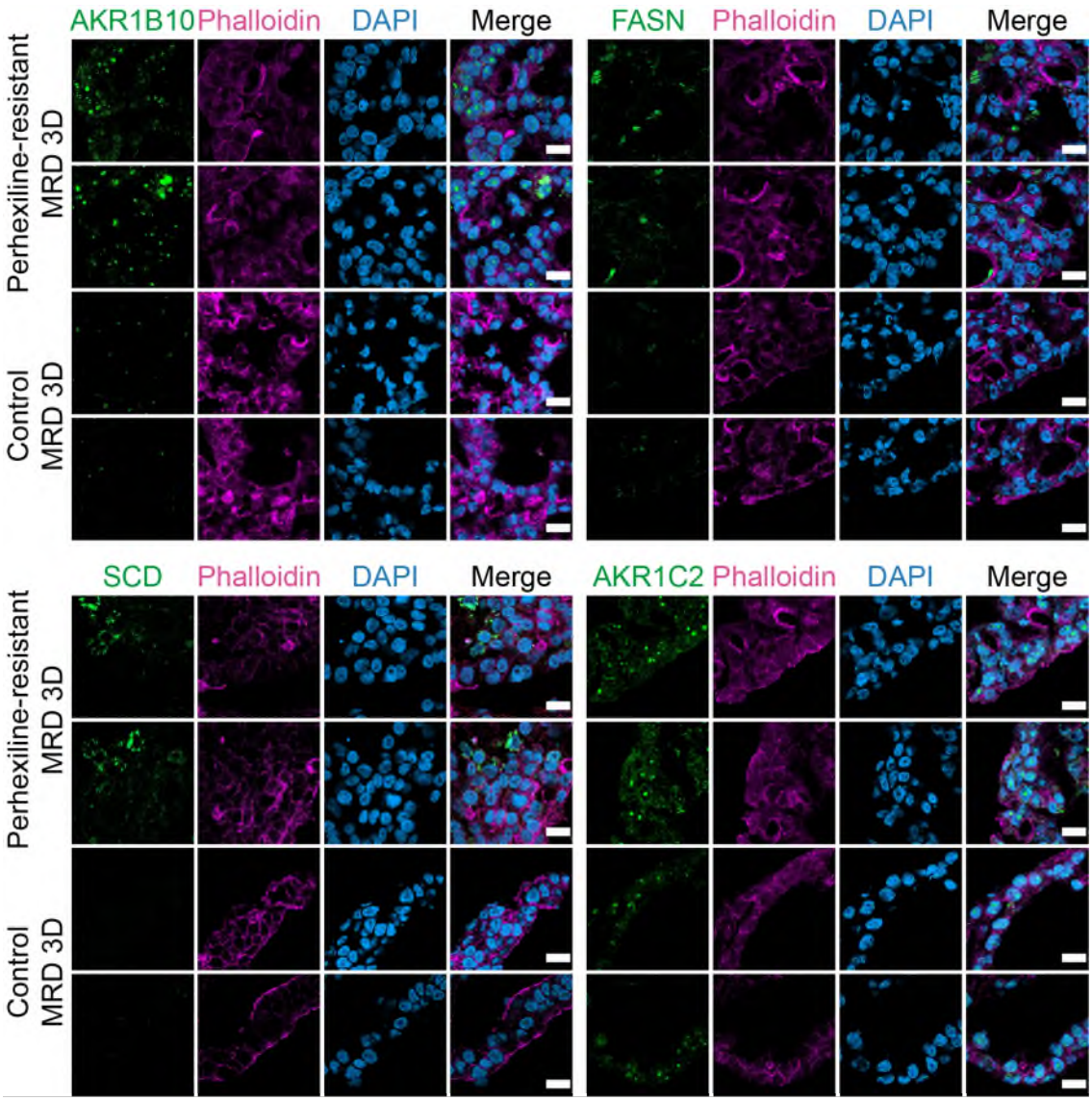


Figure 4.20. Perhexiline-resistant 3D microtumours stained with lipid metabolism marker. Confocal images showing DEGs upregulated in perhexiline-resistant MRD 3D microtumours composed of OVCAR5 at D10: AKR1B10 (green, top left), FASN (green, top right), SCD (green, bottom left), AKR1C2 (green, bottom right). The cells were also stained with phalloidin (pink) and DAPI (blue). Scale bar = 20 µm.

4.6 Summary

In this chapter, we successfully used 3D microtumours to model MRD of ovarian cancer and investigated potential FAO inhibitors that specifically targeted MRD. The transcriptomic analysis and immunofluorescence staining

demonstrated at both RNA and protein levels that the 3D microtumours are capable of recapitulating the key features of MRD, including lipid transport and metabolism, stemness of cancer cells, and non-genetic heterogeneity. These results underpin the application of 3D microtumours in disease modelling.

Differential responses to FAO inhibitors between 3D microtumours and 2D cultures highlight the significance of culturing format (3D or 2D) – even being derived from the same parental cells, the different culturing formats affect cell response to therapeutics. Transcriptomic analysis of the FAO inhibitor-resistant cells provides insight into potential resistance mechanisms. In detail, we identified perhexiline as a promising therapeutic that specifically targets MRD ovarian cancer cells. Biomarkers, such as ACSL1, FASN, SCD, AKR1B10 and AKR1C2, that were upregulated in cells survived perhexiline treatment, may serve as potential targets for eradicating residual cancer cells and preventing the development of resistance.

Statement of Authorship for joint/multi-authored papers for PGR thesis
To appear at the end of each thesis chapter submitted as an article/paper

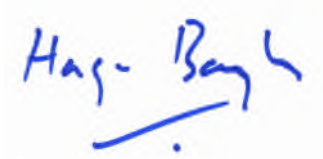
The statement shall describe the candidate's and co-authors' independent research contributions in the thesis publications. For each publication there should exist a complete statement that is to be filled out and signed by the candidate and supervisor **(only required where there isn't already a statement of contribution within the paper itself).**

Title of Paper	A 3D microtumour system that faithfully represents ovarian cancer minimal residual disease
Publication Status	□ Published □ Accepted for Publication X Submitted for Publication □ Unpublished and unsubmitted work written in a manuscript style
Publication Details	Yang, X., Artibani, M., Jin, Y., Aggarwal, A., Zhang, Y., Munoz-Galvan, S., ... & Bayley, H. (2023). A 3D microtumour system that faithfully represents ovarian cancer minimal residual disease. bioRxiv, 2023-07.

Student Confirmation

Student Name:	Xingyun Yang		
Contribution to the Paper	Conceived and designed the work; improved the microfluidic platform; performed 3D microtumour fabrication; conducted chemotherapy assays; cultured and manipulated cells; performed microscope imaging, cryo-sectioning, RNA-Seq library preparation and data and image analysis; wrote the manuscript.		
Signature: Xingyun Yang 		Date	08-09-2023

Supervisor Confirmation
By signing the Statement of Authorship, you are certifying that the candidate made a substantial contribution to the publication, and that the description described above is accurate.

Supervisor name and title: Hagan Bayley, Professor of Chemical Biology		
Supervisor comments Xingyun did most of the work reported in the preprint and submitted paper with significant contributions from Dr Mara Artibani, which will be duly acknowledged in the thesis.		
Signature: 	Date	13-09-2023

This completed form should be included in the thesis, at the end of the relevant chapter.

5 Concluding remarks

5.1 Conclusion

In December 2022, the FDA Modernisation Act 2.0 has removed the requirement for animal experiments before clinical trials, bolstering the standing of alternative drug evaluation strategy[237]. Considering together with the fact that more than 90% of medications entering clinical trials eventually failed to be licensed owing to efficacy and safety issues[153, 238], this regulation reform denotes a shift away from using animal models in favour of more competent models for drug evaluation.

This thesis describes a 3D microtumour system that represents one such model to lay between bench and bedside. 3D microtumours, tumour cells encapsulated in biocompatible hydrogels, can be conveniently fabricated by utilising the microfluidic platform. For the purpose of drug evaluation, the 3D microtumours are expected to fulfil technical requirements as well as be biologically accurate.

Technically speaking, the 3D microtumours for drug evaluation should follow these most crucial criteria: (1) consistent size; (2) uniform composition; (3) rapid production; (4) ease of scalability. Size consistency, which guarantees approximate cell number in each 3D microtumour, together with unified composition, underpin comparison among technical repeats. Rapid production (short culturing time required between fabrication and drug experiments) minimises variation induced by time, such as broad distribution of cell number caused by initial cell number differences. Ease of scalability undoubtedly

enhances throughput. The 3D microtumours formed from homogeneous cell-hydrogel suspensions exhibited small coefficient of variation (2 to 6%) in size. The microfluidic fabrication can be finished in 3 minutes, with an extra time for complete gelation of hydrogels, to produce around 100 3D microtumours. By loading more cell-hydrogel suspensions and using longer PTFE exit tubes, hundreds to thousands of 3D microtumours can be readily manufactured. The 3D microtumour system in this thesis satisfies all the above-mentioned technical criteria and outperforms conventional techniques for spheroids production.

In terms of biological accuracy, the 3D microtumours were proved to promptly recapitulate features of *in vivo* tumours, such as hypoxia and cytoskeleton organisation. With the 3D microtumour system in this work, the time needed to generate hypoxic cores was reduced to 1 day after fabrication, much shorter than the time requirement of 11 to 21 days reported by other methods[128, 156]. More specifically, 3D microtumours succeeded as the first 3D model to display MRD characteristics in drug resistant ovarian cancer, such as lipid transport and metabolism, stemness of cancer cells, and non-genetic heterogeneity, which cannot be well-represented by 2D cultures from the same parental cells. Especially, the non-genetic heterogeneity defined by five clusters of molecular cell signatures known as “Oxford Classic”[209, 239], is important for patient stratification and prognosis prediction. Therefore, the biological accuracy of the 3D microtumours reported in this thesis is also confirmed.

Another feature of 3D microtumours, the capability to incorporate multiple cell types, is of great interests. Tumour cells do not live on their own. Instead, they show extensive interactions with microenvironments, which compose of surrounding non-cancerous cells and non-cellular components[240]. To make 3D

microtumours more physiological relevant, we increased the composition complexity by producing co-culture 3D microtumours comprised of tumour cells and fibroblasts. Originally homogeneously distributed cells spontaneously self-organised into a tumour core-fibroblast shell structure, which resembles the fibrotic shell observed in tumours in patients. Cytokines released from tumour cells can induce trans-differentiation of fibroblasts at the border to myofibroblasts, which contributes to tumour invasion and drug resistance[241].

The potential of the 3D microtumours to be used for disease modelling was demonstrated in this thesis. We established the *in vitro* model of ovarian cancer MRD by using the 3D microtumours, which were employed to identify therapeutics that specifically target MRD, but not bulk tumour. We focused on the FAO pathway, which is uniquely upregulated in MRD. Different from previously reported results based on 2D cultures that etomoxir and perhexiline, both are FAO inhibitors, can selectively kill MRD cells[39], etomoxir was futile to MRD 3D microtumours, while perhexiline exhibited a far more pronounced cytotoxicity to MRD 3D microtumours than MRD 2D cultures. Transcriptomic analysis performed on the cells that survived FAO inhibitor treatment suggested possible explanations for the differential efficacy of etomoxir and perhexiline towards the MRD 3D microtumours. Significantly, the perhexiline doses that proved to be effective in 3D microtumours might be administered to ovarian cancer patients utilising hyperthermic intraperitoneal chemotherapy (HIPEC) safely and locally.

Overall, this work provided a convenient, efficient and flexible measure to fabricate 3D microtumours, which exhibited better physiological relevance than conventional 2D cultures. The microfluidic platform used for 3D microtumour

fabrication overcomes challenges that restrain 3D models from extensive applications. Successful recapitulation of MRD characteristics of ovarian cancer and identification of therapeutic candidates validated the potential of the 3D microtumours in disease modelling. Taking all together, the 3D microtumour system may seek broader applications in research and clinics.

5.2 Future directions

Further improvements of the 3D microtumour system should consider the following aspects.

First, to establish a one-step protocol for 3D microtumours fabrication, gelation and distribution. With the current established method in this thesis, the 3D microtumours are fabricated and temporarily stored in a PTFE exit tube. Only upon the complete gelation can the 3D microtumours be transferred to a culture plate and later distributed to 96-well plates for therapeutics screening. The thermal gelation takes 10 minutes to 2 hours depending on the hydrogels used. If gelation can occur synchronously with microfluidic fabrication and complete instantaneously, 3D microtumours can be distributed to 96-well plates simultaneously upon they arrive to the end of the PTFE exit tube. Automated distribution is possible with a motorised stage and a sensor for the detection of 3D microtumours. Instantaneous gelation may be achieved by photo-polymerisation. Yet, the biocompatibility of photo-initiator; intensity and wavelength of light source, and time of irradiation, should be considered carefully.

Second, to recreate the complicated tumour microenvironment with multiple cell types. Essential components of tumour microenvironment include, but are not limited to, fibroblasts, immune cells, endothelial cells (which contribute to

vascular networks), adipocytes, and neurons. These cells, together with tumour cells, create intricate crosstalk involving several members rather than just pairs of them. Initial trial in this thesis of incorporating fibroblasts in 3D microtumours was proved to be feasible and resembled the spatial distribution of the two cell types *in vivo*. For example, the combination of patient-derived ovarian cancer tumour fragments with their own immune cells in co-cultures has demonstrated the potential for tailoring immune checkpoint inhibitor therapy to individual patients[242]. Considering the fact that MRD ovarian cancer cells acquire energy from fatty acid metabolism, subsequent work of incorporating multiple cell types, such as adding adipocytes and endothelial cells to ovarian cancer cells, is worth attempts.

Next, to improve characterisation strategy for co-culture 3D microtumours. In the current work, the contributions from each cell type could not be discerned when examining properties of the co-culture 3D microtumours. For instance, cell viability quantified in co-culture 3D microtumours did not distinguish the viable fraction of each cell type. Property characterisation of individual cell type in co-culture system is, though challenging, but pivotal especially when investigating intricate crosstalk and differential responses among different cell species, or when overall characterisation results are not representative for individual cell types.

Finally, to use 3D microtumours for personalised medicine. This is a logical and pragmatic step to shift from research to clinics. The current work stood on cell lines can be conveniently adapted to primary cells without foreseeable technical issues. Biopsies, not restricted to ovarian cancer but also possible for various cancer types, collected from patients during surgery can be fabricated

into 3D microtumours. Combinations of therapeutics will then be applied to the patient-derived 3D microtumours to work out the most efficient drug cocktail. Drug resistance and recurrence may be predicted at early stage, which may give the opportunity to improve cancer outcomes.

6 Materials and methods

This chapter provides the experimental details in this thesis, including materials, methods and analysis used for the experiments described in Chapter 2, 3, and 4.

6.1 Cell maintenance

Various cells ranging from cancer to normal tissue cell lines were used in this thesis. OVCAR-5/RFP, NIH3T3/GFP, MDA-MB-231/RFP and HeLa/GFP cell lines were purchased from Cell Biolabs Inc., USA. HEK293T, OVCAR5, OVCAR8 and 3T3-L1 cell lines were purchased from ATCC. Kuramochi cells were obtained from the Japanese Collection of Research Biosources (JCRB) Cell Bank (**Table 2.2**).

6.1.1 Culture conditions

All cells (except OVCAR5, OVCAR8 and 3T3-L1) were cultured in Dulbecco's modified Eagle's medium (DMEM, Sigma-Aldrich), supplemented with 10% (v/v) fetal bovine serum (FBS, Sigma-Aldrich), 2 mM GlutaMAX™ Supplement (Gibco), 0.1 mM minimum essential medium (MEM) non-essential amino acids (NEAA, Sigma-Aldrich), and 1% (v/v) penicillin-streptomycin (Pen-Strep, 100 U mL^{-1} and 100 µg mL^{-1} respectively, Sigma-Aldrich).

OVCAR5 and OVCAR8 were cultured in RPMI 1640 (Gibco, Thermo Fisher), supplemented with 10% (v/v) FBS and 1% (v/v) Pen-Strep.

3T3-L1 cells were cultured routinely in DMEM supplemented with 10% (v/v) bovine calf serum (ATCC) and 1% (v/v) Pen-Strep. To induce differentiation of 3T3-L1 cells into adipocytes, the cells were cultured in differentiation medium following an established protocol (**Table 6.1**)[243].

All cells were cultured in tissue-culture treated flasks and maintained in a humidified incubator at 37°C and 5 % CO_2. Cells were passaged when they reached 80 to 90 % confluence.

Table 6.1. Protocol for differentiation of 3T3-L1 cells into adipocytes.

Day	Medium
D0	DMEM supplemented with 10% (v/v) bovine calf serum (ATCC) and 1% (v/v) Pen-Strep
D2	DMEM supplemented with 10% (v/v) FBS, 517 µM IBMX (Sigma-Aldrich), 1 µM dexamethasone (Sigma-Aldrich), and 167 nM insulin (Merck)
D4	DMEM supplemented with 10% (v/v) FBS and 167 nM insulin
D6	DMEM supplemented with 10% (v/v) FBS

*Cells were maintained at complete confluence for 2 d (D0 to D2).

6.1.2 Cell harvesting, counting and cryopreservation

The cells were harvested from culture flasks for passage, cryopreservation or experiments.

To harvest cells from a typical T-75 culture flask, medium was first removed from the flasks and then 10 mL phosphate-buffered saline (PBS, Sigma-Aldrich), prewarmed to 37°C, was used to rinse the cells for once. Next, the cells were incubated with 2 mL trypsin/ethylenediaminetetraacetic acid (EDTA, Sigma-Aldrich), a mild enzymatic solution, at 37°C until 90% of cells were detached from

flask surface. 2 mL medium was added to deactivate trypsin and a total of 4 mL cell suspension was transferred to a 15 mL falcon tube, which was then centrifuged at 300g for 3 minutes. The supernatant was removed and the cell pellet was resuspended in 10 mL medium.

To count the cells, a 10 µL of resuspended cell solution was mixed with a 10 µL of 0.4% trypan blue solution (Invitrogen). Cell number and viability were determined using a Countess™ Automated Cell Counter (Invitrogen).

Cells were passaged to a new T-75 flask with 10 mL prewarmed medium (37°C) at the cell number of 1×10^6 or as recommended by manufacturer (depending on cell type and doubling time).

For cryopreservation, 1×10^6 cells were resuspended in 1 mL freezing medium, which comprised 20% FBS and 10% dimethyl sulfoxide (DMSO) in DMEM, and then transferred to a 1.5 mL cryogenic vial (Thermo Scientific). The cryogenic vials were placed within a cell freezing container (Corning) and frozen at a rate of -1°C per minute by storing them in a -80°C freezer for a minimum of 2 hours. Subsequently, the vials were transferred to a liquid nitrogen dewar for long-term storage. The cells revived from liquid nitrogen storage should be passaged for at least once before they were used for experiments.

6.2 Cell-hydrogel suspension preparation

The cell-hydrogel suspension was freshly prepared by resuspending cell pellets in the desired pre-gel solution. The mixture was gently pipetted up and down to ensure thorough mixing and to prevent formation of air bubbles. Final cell density of the suspension was at the range of 3 to 4 x 10^7 cells mL^{-1}.

6.2.1 Matrigel

Matrigel® Matrix (Corning Life Sciences) is a liquid at 4°C and turns into a gel at 37°C according to manufacturer's instruction. To prepare cell-hydrogel suspension, Matrigel was thawed on ice in a 4°C refrigerator overnight. Cell pellets (4×10^6 cells) and was mixed with 90 µL Matrigel on ice with pre-cooled pipet tips. It was important to chill the pipet tips since Matrigel starts gelation above 10°C. The prepared cell-hydrogel suspension was kept on ice and should be used within 1 hour.

6.2.2 Collagen

Collagen I (Corning Life Sciences), similar to Matrigel, is a liquid at 4°C and gelates at 37°C. Collagen I was thawed on ice in a 4°C refrigerator overnight. To prepare a Collagen I pre-gel solution (2 mg mL^{-1}), 52.9 µL Collagen I (3.78 mg mL^{-1}) was diluted with 39.5 µL ice-cold DI-water, 6.15 µL 10X Dulbecco's PBS (Thermo Fisher) and 1.2 µL 1 N NaOH. Then the pre-gel solution was mixed with cell pellets on ice to make a suspension. The prepared cell-hydrogel suspension was kept on ice and should be used within 1 hour.

6.2.3 Agarose

Low melting point agarose (Thermo Fisher) melts at around 65.5°C and rapidly gelates below 25°C as instructed by the manufacturer. To prepare a 2% w/v agarose pre-gel solution, agarose powder was dissolved in sterile water at 100°C and then cooled to 37°C. Then the pre-gel solution was mixed with cell

pellets at 37°C to make a suspension. The prepared cell-hydrogel suspension was kept at 37°C and should be used within 1 hour.

6.2.4 Silk fibroin

Silk fibroin (Sigma-Aldrich) is a liquid at 4°C and gelates at raised temperature as instructed by the manufacturer. Silk fibroin was thawed in a 4°C refrigerator overnight. To prepare silk fibroin pre-gel solution, 50 mg mL^{-1} silk fibroin solution was supplemented with 10 U mL^{-1} horseradish peroxidase (type VI lyophilized powder, Sigma-Aldrich) and 0.4 µL mL^{-1} hydrogen peroxide solution (30% w/w, Sigma Aldrich). Then the pre-gel solution was mixed with cell pellets on ice to make a suspension. The prepared cell-hydrogel suspension was kept on ice and should be used within 1 hour.

6.3 Microfluidics platform and 3D microtumour fabrication

6.3.1 Microfluidic chips

The PDMS microfluidic chips employed in this thesis were manufactured using two methods: (1) the drilling hole method and, (2) the 3D printed master mould method.

In essence, both methods resulted in the three-channel microfluidic chips that operated in the same manner – single-emulsion droplets formed at the cross-junction when the oil phase encountered the aqueous phase. The distinction

between the two methods lay in the flexibility to create microfluidic chips with varying channel sizes.

6.3.1.1. Drilling hole method

In the drilling hole method following the previously reported work[106], the PDMS blocks were first prepared from Sylgard 184 (Scientific Laboratory Supplies) and then micro-sized channels were created by drilling holes through these PDMS blocks.

The two liquid components (base and curing agent) of Sylgard 184 were thoroughly mixed at a ratio of 10 to 1. This mixture (PDMS prepolymer) was poured into a petri dish with a diameter of 9 cm until it reached a liquid thickness of approximately 0.6 cm. After degassing for 30 minutes or until no air bubbles were present, the viscous liquid was heated at 70°C for 2 hours to solidify it and form PDMS. The resulting PDMS was removed from the petri dish and cut into small blocks with dimension of around 1 cm x 1 cm x 0.6 cm. Subsequently, a biopsy punch was used to drill holes through the PDMS blocks, creating three channels of T-shape (**Figure 6.1**).

Large 3D microtumours (size around 900 µm) in this thesis were created with microfluidic chips prepared with the drilling hole method.

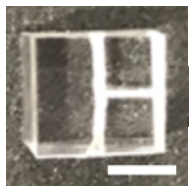


Figure 6.1. A microfluidic chip created by drilling hole method. Image of a 3-channel PDMS microfluidic chip with channel size of 900 µm. Scale bar = 0.5 cm.

With the drilling hold method, the channel size was determined by the dimensions of the biopsy punch, which provided only a few choices. To overcome this limitation, a new method involving 3D printed mould was employed to offer more options for channel dimensions.

6.3.1.2. 3D printed master mould method

In this method, PDMS prepolymer was cast onto two 3D printed master moulds, which were mirror images to each other. The two halves of the PDMS were assembled together to create a microfluidic chip.

Custom-made reverse moulds (**Figure 6.2**) were produced using a three-dimensional printer (Solid Print3D, Formlabs) using clear resin (Formlabs). PDMS prepolymer was poured into these moulds and degassed for 30 minutes. They were then heated at 70°C for approximately 1 hour until the top surface completed polymerisation, while the bottom surface was halfway polymerised and remained sticky. The two halves of the PDMS were removed from the moulds and the two sticky surfaces were firmly pressed together. Subsequently, the assembled PDMS was heated at 70°C for an additional 30 minutes to complete the polymerisation process, indicating the finalisation of the 3-channel PDMS microfluidic chip (**Figure 2.7**A).

In this thesis medium and small 3D microtumours (approximately 650 and 300 µm in size) were created using microfluidic chips prepared with the 3D printed master mould method.

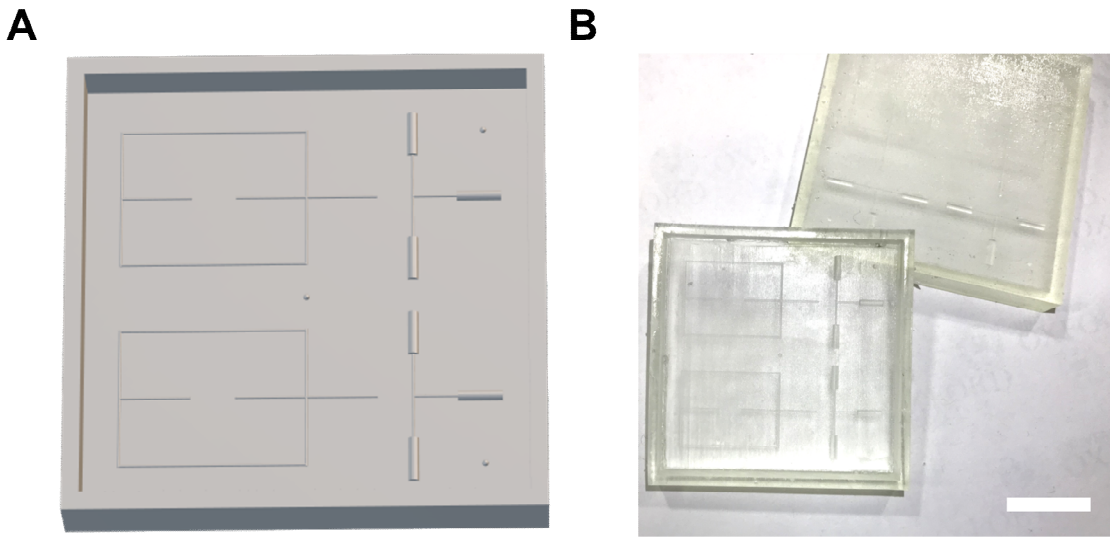


Figure 6.2. A reverse mould for the microfluidic chip. (A) Computer-aided design of the reverse mould for a microfluidic chip with channel size = 300 µm. (B) 3D printed reverse moulds. Scale bar = 1 cm.

6.3.2 Microfluidic system setup

The microfluidic system setup composed of:

(1) two Nemesys Low Pressure Syringe Pumps (Cetoni, Korbussen, Germany),

(2) a microfluidic chip and,

(3) a PTFE exit tube for collecting the formed droplets.

Two disposable syringes (BD PlastiPak) were utilised, with one loaded with the oil phase and the other with the aqueous phase. These syringes were controlled separately by two syringe pumps. Each syringe was connected to one channel of the microfluidic chip using a PTFE tube (Cole-Parmer, UK). The third channel of the microfluidic chip was linked to a PTFE exit tube. The flowrates of oil phase and aqueous phase were regulated using the software provided by the pump's manufacturer.

6.3.3 Fabrication of 3D microtumours

The microfluidic fabrication process aimed to dispense cell-hydrogel suspension fluids into approximately equal-sized droplets, which were separated by the oil phase. Subsequently, these liquid droplets were subjected to an appropriate temperature to initiate polymerisation, forming solid gels.

Since all the hydrogels used in this thesis were thermal-sensitive, temperature fluctuation could lead to partial gelation and viscosity changes, resulting in variations in droplet size. Therefore, precise temperature control was critical for microfluidic fabrication.

For the cell-hydrogel suspensions composed of Matrigel, collagen, and silk fibroin, the microfluidic fabrication was conducted in an 8°C refrigerator. For cell-agarose suspension, droplets were manufactured at approximately 37°C. The temperature control was achieved using an infrared heater (Beurer Ltd., 150 W), which was positioned at a fixed distance to equilibrate the temperature of syringes and PTFE tubes to around 37°C.

The syringes loaded with cell-hydrogel suspension and oil (tetradecane, Sigma-Aldrich) were assembled to the syringe pumps. Once the proper temperature range was reached, the syringe pumps were immediately started to pump the cell-hydrogel suspension and oil into the 3-channel microfluidic chip. Liquid droplets containing cells in hydrogels, separated by oil, were generated at the cross-junction of the microfluidic chip and then pumped into the PTFE exit tube (**Figure 2.1**). After the microfluidic fabrication was completed, the PTFE exit tube was disconnected from the microfluidic chip and brought to appropriate temperature for hydrogel polymerisation (**Table 2.1**). Once complete gelation had

occurred, the 3D microtumours were ejected from the exit tube, transferred to a flask containing cell culture medium, and maintained at 37°C with 5% CO_2. The co-culture 3D microtumours in this work consisted of 50: 50 mixture of OVCAR-5/RFP tumour cells and 3T3 fibroblasts.

6.4 Characterisations of 3D microtumours

6.4.1 Size distribution

The 3D microtumours on D0 of fabrication were imaged by using a Leica DMi8 inverted epifluorescence microscope platform equipped with a Leica DFC7000 CCD camera (Leica Microsystems Ltd, UK). Brightfield images were processed with Fiji ImageJ software to obtain the diameter of each 3D microtumour. For 3D microtumours with an elliptical cross-section, the dimensions were defined as $\text{size} = \sqrt{Major\ axis \times Minor\ axis}$ (**Figure 6.3**).

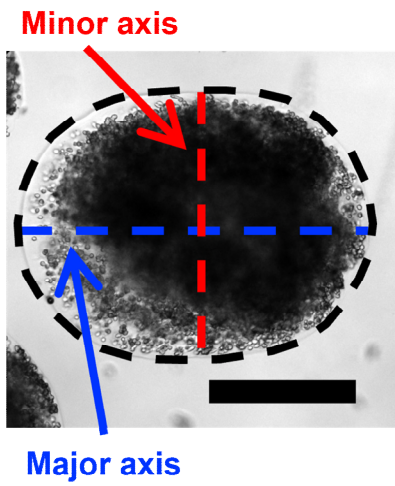


Figure 6.3. Example of size measurement for a 3D microtumour with an elliptical cross-section. In the brightfield microscope image of the 3D microtumour, the major axis and minor axis were shown in dash lines. Scale bar = 300 µm

6.4.2 Cell viability

To assess cell viability in 2D monolayer cultures and cell-hydrogel suspensions, a 10 µL cell sample was mixed with 10 µL of a 0.4% trypan blue solution (Invitrogen). Trypan blue stains dead cells without affecting viable ones. Cell viability was determined using a Countess™ Automated Cell Counter (Invitrogen).

For 3D microtumours, cell viability was evaluated using the PrestoBlue™ Cell Viability Reagent (Thermo Fisher) following the manufacturer's instructions. In a 96-well plate with black walls and clear bottoms (Greiner), each well was loaded with one 3D microtumour in 90 µL medium and 10 µL PrestoBlue™ Cell Viability Reagent. After incubation at 37°C for 30 minutes, fluorescence intensity was measured using a microplate reader (CLARIOstar Plus, BMG LABTECH) with the parameters outlined in **Table 6.2**. The fluorescence intensity, measured in relative fluorescence units (RFU), correlates with the number of viable cells. Background RFU was obtained from the wells containing 90 µL medium and 10 µL PrestoBlue reagent (without a 3D microtumour). To calculate cell viability, the background RFU was subtracted for all samples, and then the RFU from the experimental group were normalised to the control group.

Table 6.2. Microplate reader settings for fluorescence intensity measurement to evaluate cell viability.

Parameter	Value
Excitation wavelength	555 nm
Excitation bandwidth	30 nm
Emission wavelength	595 nm
Emission bandwidth	30 nm
Orbital averaging[a] diameter	4 mm

[a]With the orbital averaging on, measurements were taken within a circle of 4 mm to give the average fluorescence signal of the area. This setting is favoured in case the 3D microtumour does not sit in the centre of each well.

6.4.3 Hypoxic core staining

The hypoxic core staining was achieved using the Image-iT™ Green Hypoxia Reagent (Thermo Fisher), which exhibits fluorescence when O_2 level was below 5%. The fluorescence grows stronger with further decreasing O_2 level. Following the manufacturer's instructions, the reagent was dissolved in DMSO (Sigma-Aldrich) to prepare a 5 mM stock solution, which was then added to culture medium containing 3D microtumours, resulting in a final concentration of 5 µM. After an incubation period at 37°C for 3 hours, the 3D microtumours were imaged using a confocal laser scanning microscope (Leica TCS SP5, Leica Microsystems). A standard FITC/GFP excitation/emission filter set was applied for imaging. Z-stack images were captured with an optical section thickness of 10 µm. The optical z slices were projected to create 2D images using the z-project function in Fiji ImageJ software.

6.5 Anticancer drug responses

In this thesis, both 3D microtumours and 2D monolayer cells were subjected to treatment with two anticancer drugs, namely carboplatin and paclitaxel, to assess their responses.

For carboplatin, a 10 mM stock solution was prepared by dissolving carboplatin powder (Cayman Chemical) in sterile water. This stock solution was then serially diluted with sterile water to yield a range of working solutions, which were added to cell medium at a volume ratio of 1:20, resulting in a maximum final concentration of 500 µM.

As for paclitaxel, a 1 mM stock solution was prepared by dissolving paclitaxel powder (Invitrogen) in DMSO. This stock solution was then serially diluted with DMSO to yield a range of working solutions, which were added to cell medium at a volume ratio of 1:100, achieving a maximum final concentration of 1 µM.

Drug evaluation experiments were conducted in 96-well plates with black walls and clear bottoms (Greiner) to avoid signal crosstalk between individual wells.

In the case of 3D microtumours, on the day of microfluidic fabrication (D0), each well of the 96-well plate was filled with one 3D microtumour in 110 µL of medium (**Figure 3.9**). After incubating at 37°C for 2 days, the medium was replaced with drug-containing medium, and the treatment lasted for 4 days. At the end of the treatment, cell viability was evaluated by adding 10 µL PrestoBlue reagent to each well of the 96-well plate as described in section 6.4.2. For each treatment condition, 3D microtumours n = 20 to 32.

For 2D monolayer cultures, 5000 cells in 110 µL medium were seeded into each well of the 96-well plate. After incubating at 37°C for 2 days, the medium

was replaced with drug-containing medium, and the treatment continued for 4 days. The medium exchange was performed gently to minimise disturbance to the cells. At the end of the treatment, 10 µL PrestoBlue reagent was added to each well for cell viability assessment. For each treatment condition, 2D monolayer cultures n = 11 to 21.

The cell viability data were analysed and the fitted dose-response curves were generated using OriginPro 2023 (OriginLab Corporation). The IC_{50} values, representing the drug concentration at which 50% cell viability was observed, were derived from the dose-response curves.

6.6 Minimal residual disease modelling

6.6.1 Preparation of MRD- mimicking cells

In this thesis, three ovarian cancer cell lines – OVCAR-5/RFP, OVCAR8 and OVCAR5 – were employed to create models of MRD. As previously reported by Artibani et al., MRD-like cells can be prepared *in vitro* by subjecting 2D naïve cancer cells to a two-week treatment with carboplatin. This treatment results in the death of approximately 90% of the cells, and the remaining surviving cells constitute the MRD-mimicking population[39].

In details, on D0, 2D naïve cancer cells were seeded to culture flasks. One of these flasks was designated as the no-drug control, and it was supplied with regular medium throughout the two-week treatment period. For all other flasks, on D1, the regular culture medium was replaced with a carboplatin-containing medium. On D7, the old medium was removed and replaced with freshly prepared carboplatin-containing medium. The cells were monitored by

microscopy daily to determine whether the second dose of carboplatin on D7 was necessary. If around 10% cells remained viable (compared to the no-drug control) on D7, the cells were maintained with the initial dose of carboplatin for the remainder of the treatment window. On D14, all surviving cells were collected and subsequently expanded for 2 to 14 days (until enough cells could be extracted for experiments) to produce the MRD-mimicking cells for later use. The optimised parameters, including cell seeding density, carboplatin dose number and concentration, were summarised in **Table 4.1**.

6.6.2 Fatty acid oxidation inhibitor responses

To identify potential therapeutics for MRD, two FAO inhibitors, etomoxir and perhexiline, were tested on 3D microtumours.

For etomoxir, a 40 mM stock solution was prepared by dissolving etomoxir sodium salt (Stratech) in DMSO. This stock solution was then diluted in cell medium at a volume ratio of 1:1000, resulting in a final concentration of 40 µM.

For perhexiline, a 4 mM stock solution was prepared by dissolving perhexiline (Cambridge Bioscience) in DMSO. This stock solution was then diluted in cell medium at a volume ratio of 1:1000, resulting in a final concentration of 4 µM.

DMSO was added to cell medium at a volume ratio of 1:1000 to serve as the control group.

Both naïve and MRD 3D microtumours were subjected to a 10-day treatment with FAO inhibitors in 12-well plates. On D0 of microfluidic fabrication, five 3D microtumours were distributed into each well of a 12-well plate, and 2 mL of either drug-containing or DMSO-containing medium was supplied to each well. On D10,

the 3D microtumours were collected for cell viability evaluation using PrestoBlue reagent (**Figure 4.14**).

6.7 Transcriptomic analysis with bulk RNA-Sequencing

6.7.1 RNA extraction and library preparation

RNA extraction was carried out using the RNAqueous-Micro Total RNA Isolation Kit (Thermo Fisher). The quality of the extracted RNA was evaluated by RNA integrity number (RIN) using the 2200 TapeStation System (Agilent Technologies, Inc.). Only samples with RIN values above 7 were taken forward for library preparation.

Library preparation was performed using a KAPA HyperPrep Kit (Kapa Biosystems) following the manufacturer's instructions. The prepared libraries were assessed using the 2200 TapeStation System and then quantified with a Qubit 2.0 Fluorometer (Thermo Fisher, Invitrogen). For multiplexing, library pools containing different samples were quantified with the KAPA Library Quantification Kit (Roche) and subsequently subjected to sequencing. Sequencing was conducted on the NextSeq500 platform (Illumina) by using 75 bp paired-end reads.

6.7.2 Processing of RNA-Seq data

The sequencing reads obtained from FASTQ files were trimmed for adapter sequences and quality with Trim Galore!. The trimmed reads were then mapped to the UCSC hg19 human genome assembly using STAR (v2.7.3a).

Subsequently, read counts were generated through the application of subread FeatureCounts (v2.0.0).

Differential expression analysis was conducted utilising edgeR (v3.36.0). To identify significantly enriched pathways and processes, statistical overrepresentation analysis was performed using PANTHER (v17), with the significance threshold set at a false discovery rate (FDR) of less than 0.05.

Deconvolution analysis, as previously described[209], was performed in the relative mode. For each tumour sample, the scores of the five molecular signatures were normalised to sum up to 1, allowing for a relative assessment of their contributions.

6.8 Immunofluorescence staining

The 3D microtumours and the clinical samples were embedded in an optimal cutting temperature (OCT) compound (NEG-50, Richard-Allan Scientific), frozen and kept at -80°C until sectioning. Sections of 10 µm thickness were prepared using a CryoStar cryostat microtome (Thermo Fisher) and transferred to an adhesion glass slide (VWR, SuperFrost Plus).

These sections were subsequently stained for immunofluorescence imaging. The slides were washed with ice-cold PBS twice to remove the OCT compound. Next, they were fixed in 4% paraformaldehyde (PFA) for 10 minutes and permeabilized using a solution of 0.1%TritonX-100 in PBS for 10 minutes at room temperature. Following this, the samples were incubated in blocking buffer composed of 2% bovine serum albumin (BSA) and 0.1% TritonX-100 in PBS for 1 hour. After blocking, the samples were subjected to an overnight incubation with the diluted primary antibodies (**Table 6.3**) in a humidified chamber at 4°C.

The following day, the slides were washed with PBS and then incubated with secondary antibodies and phalloidin for 1 hour at room temperature. After extensive washes with PBS, the slides were mounted with VECTASHIELD Antifade Mounting Medium with DAPI (VectorLaboratories). Finally, the slides were dried in the dark before being imaged using a confocal microscope (Zeiss900).

Table 6.3. List of antibodies used for immunofluorescence staining.

Antibody	Catalogue number	Dilution
VEGFA	Thermo Fisher MA1-16629	1 in 200
NDRG1	abcam ab124689	1 in 200
P4HA1	abcam ab244302	1 in 200
ALDH3A1	abcam ab76976	1 in 100
SCD	Thermo Fisher MA5-27542	1 in 100
AKR1B10	abcam ab96417	1 in 500
CPT1A	abcam ab128568	1 in 50
ACADVL	abcam ab155138	1 in 200
AKR1C1/2	abcam ab131375	1 in 200
FASN	abcam ab128856	1 in 50

7 Bibliography

1. Zhang, R.; Siu, M. K. Y.; Ngan, H. Y. S.; Chan, K. K. L. Molecular Biomarkers for the Early Detection of Ovarian Cancer. *International Journal of Molecular Sciences* **2022**, *23* (19), 12041.

2. UK, C. R. *Ovarian cancer survival statistics*. https://www.cancerresearchuk.org/health-professional/cancer-statistics/statistics-by-cancer-type/ovarian-cancer/survival#heading-Zero (accessed 23/03/2023).

3. UK, C. R. *Cancer survival statistics for all cancers combined*. https://www.cancerresearchuk.org/health-professional/cancer-statistics/survival/all-cancers-combined#heading-Zero (accessed 23/03/2023).

4. UK, C. R. *Age-Standardised Ten-Year Net Survival Trends*. https://www.cancerresearchuk.org/health-professional/cancer-statistics/survival/common-cancers-compared#heading-Three (accessed 09/09/2023).

5. Cybula, M.; Bieniasz, M. Patient-derived tumor models are attractive tools to repurpose drugs for ovarian cancer treatment: pre-clinical updates. *Oncotarget* **2022**, *13*, 553-575.

6. Shah, S.; Cheung, A.; Kutka, M.; Sheriff, M.; Boussios, S. Epithelial Ovarian Cancer: Providing Evidence of Predisposition Genes. *International Journal of Environmental Research and Public Health* **2022**, *19* (13), 8113.

7. Van Nieuwenhuysen, E.; Busschaert, P.; Laenen, A.; Moerman, P.; Han, S. N.; Neven, P.; Lambrechts, D.; Vergote, I. Loss of 1p36.33 Frequent in Low-Grade Serous Ovarian Cancer. *Neoplasia* **2019**, *21* (6), 582-590.

8. Labidi-Galy, S. I.; Papp, E.; Hallberg, D.; Niknafs, N.; Adleff, V.; Noe, M.; Bhattacharya, R.; Novak, M.; Jones, S.; Phallen, J.; et al. High grade serous ovarian carcinomas originate in the fallopian tube. *Nature Communications* **2017**, *8* (1), 1093.

9. Zhu, J. W.; Charkhchi, P.; Akbari, M. R. Potential clinical utility of liquid biopsies in ovarian cancer. *Molecular Cancer* **2022**, *21* (1), 114.

10. Cheung, A.; Shah, S.; Parker, J.; Soor, P.; Limbu, A.; Sheriff, M.; Boussios, S. Non-Epithelial Ovarian Cancers: How Much Do We Really Know? *International journal of environmental research and public health* **2022**, *19* (3), 1106.

11. Pokhriyal, R.; Hariprasad, R.; Kumar, L.; Hariprasad, G. Chemotherapy Resistance in Advanced Ovarian Cancer Patients. *Biomarkers in Cancer* **2019**, *11*, 1179299X19860815.

12. Yang, L.; Xie, H.-J.; Li, Y.-Y.; Wang, X.; Liu, X.-X.; Mai, J. Molecular mechanisms of platinum-based chemotherapy resistance in ovarian cancer (Review). *Oncology Reports* **2022**, *47* (4), 82.

13. Giornelli, G. H. Management of relapsed ovarian cancer: a review. *SpringerPlus* **2016**, *5* (1), 1197.

14. Ferrero, J. M.; Weber, B.; Geay, J. F.; Lepille, D.; Orfeuvre, H.; Combe, M.; Mayer, F.; Leduc, B.; Bourgeois, H.; Paraiso, D.; Pujade-Lauraine, E. Second-line chemotherapy with pegylated liposomal doxorubicin and carboplatin is highly effective in patients with advanced ovarian cancer in late relapse: a GINECO phase II trial. *Annals of Oncology* **2007**, *18* (2), 263-268.

15. Vargas-Hernández, V. M.; Moreno-Eutimio, M. A.; Acosta-Altamirano, G.; Vargas-Aguilar, V. M. Management of recurrent epithelial ovarian cancer. *Gland Surg* **2014**, *3* (3), 198-202.

16. Davis, A.; Tinker, A. V.; Friedlander, M. “Platinum resistant” ovarian cancer: What is it, who to treat and how to measure benefit? *Gynecologic Oncology* **2014**, *133* (3), 624-631.

17. Song, M.; Cui, M.; Liu, K. Therapeutic strategies to overcome cisplatin resistance in ovarian cancer. *European Journal of Medicinal Chemistry* **2022**, *232*, 114205.

18. Oronsky, B.; Ray, C. M.; Spira, A. I.; Trepel, J. B.; Carter, C. A.; Cottrill, H. M. A brief review of the management of platinum-resistant–platinum-refractory ovarian cancer. *Medical Oncology* **2017**, *34* (6), 103.

19. Poveda, A. M.; Selle, F.; Hilpert, F.; Reuss, A.; Savarese, A.; Vergote, I.; Witteveen, P.; Bamias, A.; Scotto, N.; Mitchell, L.; Pujade-Lauraine, E. Bevacizumab Combined With Weekly Paclitaxel, Pegylated Liposomal Doxorubicin, or Topotecan in Platinum-Resistant Recurrent Ovarian Cancer: Analysis by Chemotherapy Cohort of the Randomized Phase III AURELIA Trial. *Journal of Clinical Oncology* **2015**, *33* (32), 3836-3838.

20. Cristea, M.; Han, E.; Salmon, L.; Morgan, R. J. Review: Practical considerations in ovarian cancer chemotherapy. *Therapeutic Advances in Medical Oncology* **2010**, *2* (3), 175-187.

21. Ricciardelli, C.; Rodgers, R. J. Extracellular Matrix of Ovarian Tumors. *Semin Reprod Med* **2006**, *24* (04), 270-282.

22. Kohlberger, P.; Muller-Klingspor, V.; Heinzl, H.; Obermair, A.; Breitenecker, G.; Leodolter, S. Prognostic value of laminin-5 in serous adenocarcinomas of the ovary. *Anticancer Res* **2002**, *22* (6B), 3541-3544.

23. Cracchiolo, B. M.; Hanauske-Abel, H. M.; Schwartz, P. E.; Chambers, J. T.; Holland, B.; Chambers, S. K. Procollagen-Derived Biomarkers in Malignant Ascites of Ovarian Cancer: Independent Prognosticators for Progression-Free Interval and Survival. *Gynecologic Oncology* **2002**, *87* (1), 24-33.

24. Rodríguez-Rodríguez, L.; Sancho-Torres, I.; Mesonero, C.; Gibbon, D. G.; Shih, W. J.; Zotalis, G. The CD44 receptor is a molecular predictor of survival in ovarian cancer. *Medical Oncology* **2003**, *20* (3), 255-263.

25. Ouni, E.; Peaucelle, A.; Haas, K. T.; Van Kerk, O.; Dolmans, M.-M.; Tuuri, T.; Otala, M.; Amorim, C. A. A blueprint of the topology and mechanics of the human ovary for next-generation bioengineering and diagnosis. *Nature Communications* **2021**, *12* (1), 5603.

26. Ahir, B. K.; Engelhard, H. H.; Lakka, S. S. Tumor Development and Angiogenesis in Adult Brain Tumor: Glioblastoma. *Molecular Neurobiology* **2020**, *57* (5), 2461-2478.

27. Folkman, J. Role of angiogenesis in tumor growth and metastasis. *Seminars in Oncology* **2002**, *29* (6), 15-18.

28. Ortiz-Prado, E.; Dunn, J. F.; Vasconez, J.; Castillo, D.; Viscor, G. Partial pressure of oxygen in the human body: a general review. *American journal of blood research* **2019**, *9* (1), 1-14.

29. Vitale, F.; Cacciottola, L.; Yu, F. S.; Barretta, M.; Hossay, C.; Donnez, J.; Dolmans, M. M. Importance of oxygen tension in human ovarian tissue in vitro culture. *Human Reproduction* **2023**, *38* (8), 1538-1546.

30. De Munck, N.; Janssens, R.; Segers, I.; Tournaye, H.; Van de Velde, H.; Verheyen, G. Influence of ultra-low oxygen (2%) tension on in-vitro human embryo development. *Human Reproduction* **2019**, *34* (2), 228-234.

31. Liberto, J. M.; Chen, S.-Y.; Shih, I.-M.; Wang, T.-H.; Wang, T.-L.; Pisanic, T. R. Current and Emerging Methods for Ovarian Cancer Screening and Diagnostics: A Comprehensive Review. *Cancers* **2022**, *14* (12), 2885.

32. Zhang, M.; Chen, Z.; Wang, Y.; Zhao, H.; Du, Y. The Role of Cancer-Associated Fibroblasts in Ovarian Cancer. *Cancers* **2022**, *14* (11), 2637.

33. Chien, J.; Kuang, R.; Landen, C.; Shridhar, V. Platinum-Sensitive Recurrence in Ovarian Cancer: The Role of Tumor Microenvironment. *Frontiers in Oncology* **2013**, *3*, 251.

34. Pantel, K.; Alix-Panabières, C. Liquid biopsy and minimal residual disease — latest advances and implications for cure. *Nature Reviews Clinical Oncology* **2019**, *16* (7), 409-424.

35. Larribère, L.; Martens, U. M. Advantages and Challenges of Using ctDNA NGS to Assess the Presence of Minimal Residual Disease (MRD) in Solid Tumors. *Cancers* **2021**, *13* (22), 5698.

36. Honoré, N.; Galot, R.; van Marcke, C.; Limaye, N.; Machiels, J.-P. Liquid Biopsy to Detect Minimal Residual Disease: Methodology and Impact. *Cancers* **2021**, *13* (21), 5364.

37. Buccisano, F.; Maurillo, L.; Del Principe, M. I.; Del Poeta, G.; Sconocchia, G.; Lo-Coco, F.; Arcese, W.; Amadori, S.; Venditti, A. Prognostic and therapeutic implications of minimal residual disease detection in acute myeloid leukemia. *Blood* **2012**, *119* (2), 332-341.

38. Luskin, M. R.; Murakami, M. A.; Manalis, S. R.; Weinstock, D. M. Targeting minimal residual disease: a path to cure? *Nature Reviews Cancer* **2018**, *18* (4), 255-263.

39. Artibani, M.; Masuda, K.; Hu, Z.; Rauher, P. C.; Mallett, G.; Wietek, N.; Morotti, M.; Chong, K.; KaramiNejadRanjbar, M.; Zois, C. E.; et al. Adipocyte-like signature in ovarian cancer minimal residual disease identifies metabolic vulnerabilities of tumor-initiating cells. *JCI Insight* **2021**, *6* (11), e147929.

40. Day, C.-P.; Merlino, G.; Van Dyke, T. Preclinical Mouse Cancer Models: A Maze of Opportunities and Challenges. *Cell* **2015**, *163* (1), 39-53.

41. Hickman, J. A.; Graeser, R.; de Hoogt, R.; Vidic, S.; Brito, C.; Gutekunst, M.; van der Kuip, H.; consortium, I. P. Three-dimensional models of cancer for pharmacology and cancer cell biology: Capturing tumor complexity in vitro/ex vivo. *Biotechnology Journal* **2014**, *9* (9), 1115-1128.

42. Kapałczyńska, M.; Kolenda, T.; Przybyła, W.; Zajączkowska, M.; Teresiak, A.; Filas, V.; Ibbs, M.; Bliźniak, R.; Łuczewski, Ł.; Lamperska, K. 2D and 3D cell cultures – a comparison of different types of cancer cell cultures. *Arch Med Sci* **2018**, *14* (4), 910-919.

43. Augustine, R.; Kalva, S. N.; Ahmad, R.; Zahid, A. A.; Hasan, S.; Nayeem, A.; McClements, L.; Hasan, A. 3D Bioprinted cancer models: Revolutionizing personalized cancer therapy. *Translational Oncology* **2021**, *14* (4), 101015.

44. Vergani, L.; Grattarola, M.; Nicolini, C. Modifications of chromatin structure and gene expression following induced alterations of cellular shape. *The International Journal of Biochemistry & Cell Biology* **2004**, *36* (8), 1447-1461.

45. Jensen, C.; Teng, Y. Is It Time to Start Transitioning From 2D to 3D Cell Culture? *Frontiers in Molecular Biosciences* **2020**, *7*, 33.

46. Wang, R.; Xu, J.; Juliette, L.; Castilleja, A.; Love, J.; Sung, S.-Y.; Zhau, H. E.; Goodwin, T. J.; Chung, L. W. K. Three-dimensional co-culture models to study prostate cancer growth, progression, and metastasis to bone. *Seminars in Cancer Biology* **2005**, *15* (5), 353-364.

47. Cekanova, M.; Rathore, K. Animal models and therapeutic molecular targets of cancer: utility and limitations. *Drug Design, Development and Therapy* **2014**, *8*, 1911-1922.

48. Sharpless, N. E.; DePinho, R. A. The mighty mouse: genetically engineered mouse models in cancer drug development. *Nature Reviews Drug Discovery* **2006**, *5* (9), 741-754.

49. Bakiri, L.; Wagner, E. F. Mouse models for liver cancer. *Molecular Oncology* **2013**, *7* (2), 206-223.

50. Zitvogel, L.; Pitt, J. M.; Daillère, R.; Smyth, M. J.; Kroemer, G. Mouse models in oncoimmunology. *Nature Reviews Cancer* **2016**, *16* (12), 759-773.

51. Langhans, S. A. Three-Dimensional in Vitro Cell Culture Models in Drug Discovery and Drug Repositioning. *Frontiers in Pharmacology* **2018**, *9*, 6.

52. Johnson, P. A.; Giles, J. R. The hen as a model of ovarian cancer. *Nature Reviews Cancer* **2013**, *13* (6), 432-436.

53. Asghar, W.; El Assal, R.; Shafiee, H.; Pitteri, S.; Paulmurugan, R.; Demirci, U. Engineering cancer microenvironments for in vitro 3-D tumor models. *Materials Today* **2015**, *18* (10), 539-553.

54. Ravi, M.; Paramesh, V.; Kaviya, S. R.; Anuradha, E.; Solomon, F. D. P. 3D Cell Culture Systems: Advantages and Applications. *Journal of Cellular Physiology* **2015**, *230* (1), 16-26.

55. Ravi, M.; Ramesh, A.; Pattabhi, A. Contributions of 3D Cell Cultures for Cancer Research. *Journal of Cellular Physiology* **2017**, *232* (10), 2679-2697.

56. Alemany-Ribes, M.; Semino, C. E. Bioengineering 3D environments for cancer models. *Advanced Drug Delivery Reviews* **2014**, *79-80*, 40-49.

57. Velletri, T.; Villa, C. E.; Cilli, D.; Barzaghi, B.; Lo Riso, P.; Lupia, M.; Luongo, R.; Lopez-Tobon, A.; De Simone, M.; Bonnal, R. J. P.; et al. Single cell-derived spheroids capture the self-renewing subpopulations of metastatic ovarian cancer. *Cell Death & Differentiation* **2022**, *29* (3), 614-626.

58. Leonard, F.; Collnot, E.-M.; Lehr, C.-M. A Three-Dimensional Coculture of Enterocytes, Monocytes and Dendritic Cells To Model Inflamed Intestinal Mucosa in Vitro. *Molecular Pharmaceutics* **2010**, *7* (6), 2103-2119.

59. Zhu, Y.; Kang, E.; Wilson, M.; Basso, T.; Chen, E.; Yu, Y.; Li, Y.-R. 3D Tumor Spheroid and Organoid to Model Tumor Microenvironment for Cancer Immunotherapy. *Organoids* **2022**, *1* (2), 149-167.

60. Gunti, S.; Hoke, A. T. K.; Vu, K. P.; London, N. R. Organoid and Spheroid Tumor Models: Techniques and Applications. *Cancers* **2021**, *13* (4), 874.

61. Tuveson, D.; Clevers, H. Cancer modeling meets human organoid technology. *Science* **2019**, *364* (6444), 952-955.

62. Sato, T.; Vries, R. G.; Snippert, H. J.; van de Wetering, M.; Barker, N.; Stange, D. E.; van Es, J. H.; Abo, A.; Kujala, P.; Peters, P. J.; Clevers, H. Single Lgr5 stem cells build crypt-villus structures in vitro without a mesenchymal niche. *Nature* **2009**, *459* (7244), 262-265.

63. Yang, Q.; Li, M.; Yang, X.; Xiao, Z.; Tong, X.; Tuerdi, A.; Li, S.; Lei, L. Flourishing tumor organoids: History, emerging technology, and application. *Bioengineering & Translational Medicine* **2023**, *8* (5), e10559.

64. Gilazieva, Z.; Ponomarev, A.; Rutland, C.; Rizvanov, A.; Solovyeva, V. Promising Applications of Tumor Spheroids and Organoids for Personalized Medicine. *Cancers* **2020**, *12* (10), 2727.

65. Li, W.; Zhou, Z.; Zhou, X.; Khoo, B. L.; Gunawan, R.; Chin, Y. R.; Zhang, L.; Yi, C.; Guan, X.; Yang, M. 3D Biomimetic Models to Reconstitute Tumor Microenvironment In Vitro: Spheroids, Organoids, and Tumor-on-a-Chip. *Advanced Healthcare Materials* **2023**, *12* (18), 2202609.

66. Kopper, O.; de Witte, C. J.; Lõhmussaar, K.; Valle-Inclan, J. E.; Hami, N.; Kester, L.; Balgobind, A. V.; Korving, J.; Proost, N.; Begthel, H.; et al. An organoid platform for ovarian cancer captures intra- and interpatient heterogeneity. *Nature Medicine* **2019**, *25* (5), 838-849.

67. Lõhmussaar, K.; Kopper, O.; Korving, J.; Begthel, H.; Vreuls, C. P. H.; van Es, J. H.; Clevers, H. Assessing the origin of high-grade serous ovarian cancer using CRISPR-modification of mouse organoids. *Nature Communications* **2020**, *11* (1), 2660.

68. Driehuis, E.; Kretzschmar, K.; Clevers, H. Establishment of patient-derived cancer organoids for drug-screening applications. *Nature Protocols* **2020**, *15* (10), 3380-3409.

69. Driehuis, E.; van Hoeck, A.; Moore, K.; Kolders, S.; Francies, H. E.; Gulersonmez, M. C.; Stigter, E. C. A.; Burgering, B.; Geurts, V.; Gracanin, A.; et al. Pancreatic cancer organoids recapitulate disease and allow personalized drug screening. *Proceedings of the National Academy of Sciences* **2019**, *116* (52), 26580-26590.

70. Ferreira, L. P.; Gaspar, V. M.; Mano, J. F. Design of spherically structured 3D in vitro tumor models -Advances and prospects. *Acta Biomaterialia* **2018**, *75*, 11-34.

71. Weiswald, L.-B.; Bellet, D.; Dangles-Marie, V. Spherical Cancer Models in Tumor Biology. *Neoplasia* **2015**, *17* (1), 1-15.

72. Breslin, S.; O'Driscoll, L. Three-dimensional cell culture: the missing link in drug discovery. *Drug Discovery Today* **2013**, *18* (5), 240-249.

73. Rojek, K. O.; Ćwiklińska, M.; Kuczak, J.; Guzowski, J. Microfluidic Formulation of Topological Hydrogels for Microtissue Engineering. *Chemical Reviews* **2022**, *122* (22), 16839-16909.

74. Knight, E.; Przyborski, S. Advances in 3D cell culture technologies enabling tissue-like structures to be created in vitro. *Journal of Anatomy* **2015**, *227* (6), 746-756.

75. Thiele, J.; Ma, Y.; Bruekers, S. M. C.; Ma, S.; Huck, W. T. S. 25th Anniversary Article: Designer Hydrogels for Cell Cultures: A Materials Selection Guide. *Advanced Materials* **2014**, *26* (1), 125-148.

76. Kleinman, H. K.; Martin, G. R. Matrigel: Basement membrane matrix with biological activity. *Seminars in Cancer Biology* **2005**, *15* (5), 378-386.

77. Benton, G.; George, J.; Kleinman, H. K.; Arnaoutova, I. P. Advancing science and technology via 3D culture on basement membrane matrix. *Journal of Cellular Physiology* **2009**, *221* (1), 18-25.

78. Lee, G. Y.; Kenny, P. A.; Lee, E. H.; Bissell, M. J. Three-dimensional culture models of normal and malignant breast epithelial cells. *Nature Methods* **2007**, *4* (4), 359-365.

79. Murphy, S. V.; Atala, A. 3D bioprinting of tissues and organs. *Nature Biotechnology* **2014**, *32* (8), 773-785.

80. Barbosa, M. A. G.; Xavier, C. P. R.; Pereira, R. F.; Petrikaitė, V.; Vasconcelos, M. H. 3D Cell Culture Models as Recapitulators of the Tumor Microenvironment for the Screening of Anti-Cancer Drugs. *Cancers* **2022**, *14* (1), 190.

81. Kwapiszewska, K.; Michalczuk, A.; Rybka, M.; Kwapiszewski, R.; Brzózka, Z. A microfluidic-based platform for tumour spheroid culture, monitoring and drug screening. *Lab on a Chip* **2014**, *14* (12), 2096-2104.

82. Casey, J.; Yue, X.; Nguyen, T. D.; Acun, A.; Zellmer, V. R.; Zhang, S.; Zorlutuna, P. 3D hydrogel-based microwell arrays as a tumor microenvironment model to study breast cancer growth. *Biomedical Materials* **2017**, *12* (2), 025009.

83. Hoarau-Véchot, J.; Rafii, A.; Touboul, C.; Pasquier, J. Halfway between 2D and Animal Models: Are 3D Cultures the Ideal Tool to Study Cancer-Microenvironment Interactions? *International Journal of Molecular Sciences* **2018**, *19* (1), 181.

84. Ao, Z.; Cai, H.; Wu, Z.; Ott, J.; Wang, H.; Mackie, K.; Guo, F. Controllable fusion of human brain organoids using acoustofluidics. *Lab on a Chip* **2021**, *21* (4), 688-699.

85. Whitesides, G. M. The origins and the future of microfluidics. *Nature* **2006**, *442* (7101), 368-373.

86. Convery, N.; Gadegaard, N. 30 years of microfluidics. *Micro and Nano Engineering* **2019**, *2*, 76-91.

87. Niculescu, A.-G.; Chircov, C.; Bîrcă, A. C.; Grumezescu, A. M. Fabrication and Applications of Microfluidic Devices: A Review. *International Journal of Molecular Sciences* **2021**, *22* (4), 2011.

88. Amir, S.; Arathi, A.; Reshma, S.; Mohanan, P. V. Microfluidic devices for the detection of disease-specific proteins and other macromolecules, disease modelling and drug development: A review. *International Journal of Biological Macromolecules* **2023**, *235*, 123784.

89. Hong, J. W.; Quake, S. R. Integrated nanoliter systems. *Nature Biotechnology* **2003**, *21* (10), 1179-1183.

90. Garstecki, P.; Fischbach, M. A.; Whitesides, G. M. Design for mixing using bubbles in branched microfluidic channels. *Applied Physics Letters* **2005**, *86* (24), 244108.

91. Laser, D. J.; Santiago, J. G. A review of micropumps. *Journal of Micromechanics and Microengineering* **2004**, *14* (6), R35.

92. van Duinen, V.; Trietsch, S. J.; Joore, J.; Vulto, P.; Hankemeier, T. Microfluidic 3D cell culture: from tools to tissue models. *Current Opinion in Biotechnology* **2015**, *35*, 118-126.

93. Boussommier-Calleja, A.; Li, R.; Chen, M. B.; Wong, S. C.; Kamm, R. D. Microfluidics: A New Tool for Modeling Cancer–Immune Interactions. *Trends in Cancer* **2016**, *2* (1), 6-19.

94. Wang, Y.; Zhao, L.; Tian, C.; Ma, C.; Wang, J. Geometrically controlled preparation of various cell aggregates by droplet-based microfluidics. *Analytical Methods* **2015**, *7* (23), 10040-10051.

95. Sharp, K. V.; Adrian, R. J. Transition from laminar to turbulent flow in liquid filled microtubes. *Experiments in Fluids* **2004**, *36* (5), 741-747.

96. Chen, Q.; Utech, S.; Chen, D.; Prodanovic, R.; Lin, J.-M.; Weitz, D. A. Controlled assembly of heterotypic cells in a core–shell scaffold: organ in a droplet. *Lab on a Chip* **2016**, *16* (8), 1346-1349.

97. Chen, Y.; Gao, D.; Wang, Y.; Lin, S.; Jiang, Y. A novel 3D breast-cancer-on-chip platform for therapeutic evaluation of drug delivery systems. *Analytica Chimica Acta* **2018**, *1036*, 97-106.

98. Jeon, J. S.; Zervantonakis, I. K.; Chung, S.; Kamm, R. D.; Charest, J. L. In Vitro Model of Tumor Cell Extravasation. *PLOS ONE* **2013**, *8* (2), e56910.

99. Ford, C. E.; Werner, B.; Hacker, N. F.; Warton, K. The untapped potential of ascites in ovarian cancer research and treatment. *British Journal of Cancer* **2020**, *123* (1), 9-16.

100. Burleson, K. M.; Casey, R. C.; Skubitz, K. M.; Pambuccian, S. E.; Oegema, T. R.; Skubitz, A. P. N. Ovarian carcinoma ascites spheroids adhere to extracellular matrix components and mesothelial cell monolayers. *Gynecologic Oncology* **2004**, *93* (1), 170-181.

101. Yee, C.; Dickson, K.-A.; Muntasir, M. N.; Ma, Y.; Marsh, D. J. Three-Dimensional Modelling of Ovarian Cancer: From Cell Lines to Organoids for Discovery and Personalized Medicine. *Frontiers in Bioengineering and Biotechnology* **2022**, *10*, 836984.

102. Sontheimer-Phelps, A.; Hassell, B. A.; Ingber, D. E. Modelling cancer in microfluidic human organs-on-chips. *Nature Reviews Cancer* **2019**, *19* (2), 65-81.

103. Coluccio, M. L.; Perozziello, G.; Malara, N.; Parrotta, E.; Zhang, P.; Gentile, F.; Limongi, T.; Raj, P. M.; Cuda, G.; Candeloro, P.; Di Fabrizio, E. Microfluidic platforms for cell cultures and investigations. *Microelectronic Engineering* **2019**, *208*, 14-28.

104. Akgönüllü, S.; Bakhshpour, M.; Pişkin, A. K.; Denizli, A. Microfluidic Systems for Cancer Diagnosis and Applications. *Micromachines* **2021**, *12* (11), 1349.

105. Moshksayan, K.; Kashaninejad, N.; Warkiani, M. E.; Lock, J. G.; Moghadas, H.; Firoozabadi, B.; Saidi, M. S.; Nguyen, N.-T. Spheroids-on-a-chip: Recent advances and design considerations in microfluidic platforms for spheroid formation and culture. *Sensors and Actuators B: Chemical* **2018**, *263*, 151-176.

106. Ma, S.; Mukherjee, N.; Mikhailova, E.; Bayley, H. Gel Microrods for 3D Tissue Printing. *Advanced Biosystems* **2017**, *1* (8), 1700075.

107. Badr-Eldin, S. M.; Aldawsari, H. M.; Kotta, S.; Deb, P. K.; Venugopala, K. N. Three-Dimensional In Vitro Cell Culture Models for Efficient Drug Discovery: Progress So Far and Future Prospects. *Pharmaceuticals* **2022**, *15* (8), 926.

108. Tibbitt, M. W.; Anseth, K. S. Hydrogels as extracellular matrix mimics for 3D cell culture. *Biotechnology and Bioengineering* **2009**, *103* (4), 655-663.

109. Passaniti, A.; Kleinman, H. K.; Martin, G. R. Matrigel: history/background, uses, and future applications. *Journal of cell communication and signaling* **2022**, *16* (4), 621-626.

110. Benton, G.; Arnaoutova, I.; George, J.; Kleinman, H. K.; Koblinski, J. Matrigel: From discovery and ECM mimicry to assays and models for cancer research. *Advanced Drug Delivery Reviews* **2014**, *79-80*, 3-18.

111. Hughes, C. S.; Postovit, L. M.; Lajoie, G. A. Matrigel: A complex protein mixture required for optimal growth of cell culture. *Proteomics* **2010**, *10* (9), 1886-1890.

112. Lou, J.; Stowers, R.; Nam, S.; Xia, Y.; Chaudhuri, O. Stress relaxing hyaluronic acid-collagen hydrogels promote cell spreading, fiber remodeling, and focal adhesion formation in 3D cell culture. *Biomaterials* **2018**, *154*, 213-222.

113. Ma, S.; Natoli, M.; Liu, X.; Neubauer, M. P.; Watt, F. M.; Fery, A.; Huck, W. T. S. Monodisperse collagen–gelatin beads as potential platforms for 3D cell culturing. *Journal of Materials Chemistry B* **2013**, *1* (38), 5128-5136.

114. Jee, J. H.; Lee, D. H.; Ko, J.; Hahn, S.; Jeong, S. Y.; Kim, H. K.; Park, E.; Choi, S. Y.; Jeong, S.; Lee, J. W.; et al. Development of Collagen-Based 3D Matrix for Gastrointestinal Tract-Derived Organoid Culture. *Stem Cells International* **2019**, *2019*, 8472712.

115. Kroehne, V.; Heschel, I.; Schügner, F.; Lasrich, D.; Bartsch, J. W.; Jockusch, H. Use of a novel collagen matrix with oriented pore structure for muscle cell differentiation in cell culture and in grafts. *Journal of Cellular and Molecular Medicine* **2008**, *12* (5a), 1640-1648.

116. Rieu, C.; Parisi, C.; Mosser, G.; Haye, B.; Coradin, T.; Fernandes, F. M.; Trichet, L. Topotactic Fibrillogenesis of Freeze-Cast Microridged Collagen Scaffolds for 3D Cell Culture. *ACS Applied Materials & Interfaces* **2019**, *11* (16), 14672-14683.

117. Atoufi, Z.; Zarrintaj, P.; Motlagh, G. H.; Amiri, A.; Bagher, Z.; Kamrava, S. K. A novel bio electro active alginate-aniline tetramer/ agarose scaffold for tissue engineering: synthesis, characterization, drug release and cell culture study. *Journal of Biomaterials Science, Polymer Edition* **2017**, *28* (15), 1617-1638.

118. Yamada, Y.; Yoshida, C.; Hamada, K.; Kikkawa, Y.; Nomizu, M. Development of Three-Dimensional Cell Culture Scaffolds Using Laminin Peptide-Conjugated Agarose Microgels. *Biomacromolecules* **2020**, *21* (9), 3765-3771.

119. Mercey, E.; Obeïd, P.; Glaise, D.; Calvo-Muñoz, M.-L.; Guguen-Guillouzo, C.; Fouqué, B. The application of 3D micropatterning of agarose substrate for cell culture and in situ comet assays. *Biomaterials* **2010**, *31* (12), 3156-3165.

120. Zhuang, A.; Huang, X.; Fan, S.; Yao, X.; Zhu, B.; Zhang, Y. One-Step Approach to Prepare Transparent Conductive Regenerated Silk Fibroin/PEDOT:PSS Films for Electroactive Cell Culture. *ACS Applied Materials & Interfaces* **2022**, *14* (1), 123-137.

121. Motta, A.; Migliaresi, C.; Faccioni, F.; Torricelli, P.; Fini, M.; Giardino, R. Fibroin hydrogels for biomedical applications: preparation, characterization and in vitro cell culture studies. *Journal of Biomaterials Science, Polymer Edition* **2004**, *15* (7), 851-864.

122. Zou, S.; Yao, X.; Shao, H.; Reis, R. L.; Kundu, S. C.; Zhang, Y. Nonmulberry silk fibroin-based biomaterials: Impact on cell behavior regulation and tissue regeneration. *Acta Biomaterialia* **2022**, *153*, 68-84.

123. Prastowo, A.; Feuerborn, A.; Cook, P. R.; Walsh, E. J. Biocompatibility of fluids for multiphase drops-in-drops microfluidics. *Biomedical Microdevices* **2016**, *18* (6), 114.

124. Neagu, A.-A.; Niţă, I.; Botez, E. Correlations between some physico-chemical properties of sunflower oil. *Ovidius University Annals of Chemistry* **2014**, *25* (2), 71-74.

125. Poon, C. Measuring the density and viscosity of culture media for optimized computational fluid dynamics analysis of in vitro devices. *Journal of the Mechanical Behavior of Biomedical Materials* **2022**, *126*, 105024.

126. Kim, Y.-N.; Koo, K. H.; Sung, J. Y.; Yun, U.-J.; Kim, H. Anoikis Resistance: An Essential Prerequisite for Tumor Metastasis. *International Journal of Cell Biology* **2012**, *2012*, 306879.

127. Riffle, S.; Hegde, R. S. Modeling tumor cell adaptations to hypoxia in multicellular tumor spheroids. *Journal of Experimental & Clinical Cancer Research* **2017**, *36* (1), 102.

128. Riffle, S.; Pandey, R. N.; Albert, M.; Hegde, R. S. Linking hypoxia, DNA damage and proliferation in multicellular tumor spheroids. *BMC Cancer* **2017**, *17* (1), 338.

129. Scabini, M.; Stellari, F.; Cappella, P.; Rizzitano, S.; Texido, G.; Pesenti, E. In vivo imaging of early stage apoptosis by measuring real-time caspase-3/7 activation. *Apoptosis* **2011**, *16* (2), 198-207.

130. Tawa, P.; Hell, K.; Giroux, A.; Grimm, E.; Han, Y.; Nicholson, D. W.; Xanthoudakis, S. Catalytic activity of caspase-3 is required for its degradation: stabilization of the active complex by synthetic inhibitors. *Cell Death & Differentiation* **2004**, *11* (4), 439-447.

131. Crouch, S. P. M.; Kozlowski, R.; Slater, K. J.; Fletcher, J. The use of ATP bioluminescence as a measure of cell proliferation and cytotoxicity. *Journal of Immunological Methods* **1993**, *160* (1), 81-88.

132. Xu, M.; McCanna, D. J.; Sivak, J. G. Use of the viability reagent PrestoBlue in comparison with alamarBlue and MTT to assess the viability of human corneal epithelial cells. *Journal of Pharmacological and Toxicological Methods* **2015**, *71*, 1-7.

133. Chisti, Y. Hydrodynamic Damage to Animal Cells. *Critical Reviews in Biotechnology* **2001**, *21* (2), 67-110.

134. Regmi, S.; Fu, A.; Luo, K. Q. High Shear Stresses under Exercise Condition Destroy Circulating Tumor Cells in a Microfluidic System. *Scientific Reports* **2017**, *7* (1), 39975.

135. Abbott, R. D.; Kaplan, D. L. Strategies for improving the physiological relevance of human engineered tissues. *Trends in Biotechnology* **2015**, *33* (7), 401-407.

136. Aw Yong, K. M.; Li, Z.; Merajver, S. D.; Fu, J. Tracking the tumor invasion front using long-term fluidic tumoroid culture. *Scientific Reports* **2017**, *7* (1), 10784.

137. Abbott, R. D.; Kimmerling, E. P.; Cairns, D. M.; Kaplan, D. L. Silk as a Biomaterial to Support Long-Term Three-Dimensional Tissue Cultures. *ACS Applied Materials & Interfaces* **2016**, *8* (34), 21861-21868.

138. Zhang, Y.; Li, T.-S.; Lee, S.-T.; Wawrowsky, K. A.; Cheng, K.; Galang, G.; Malliaras, K.; Abraham, M. R.; Wang, C.; Marbán, E. Dedifferentiation and Proliferation of Mammalian Cardiomyocytes. *PLOS ONE* **2010**, *5* (9), e12559.

139. Dallo, S. F.; Baseman, J. B. Intracellular DNA replication and long-term survival of pathogenic mycoplasmas. *Microbial Pathogenesis* **2000**, *29* (5), 301-309.

140. Habanjar, O.; Diab-Assaf, M.; Caldefie-Chezet, F.; Delort, L. 3D Cell Culture Systems: Tumor Application, Advantages, and Disadvantages. *International Journal of Molecular Sciences* **2021**, *22* (22), 12200.

141. Costa, E. C.; Moreira, A. F.; de Melo-Diogo, D.; Gaspar, V. M.; Carvalho, M. P.; Correia, I. J. 3D tumor spheroids: an overview on the tools and techniques used for their analysis. *Biotechnology Advances* **2016**, *34* (8), 1427-1441.

142. Jayson, G. C.; Kohn, E. C.; Kitchener, H. C.; Ledermann, J. A. Ovarian cancer. *The Lancet* **2014**, *384* (9951), 1376-1388.

143. Bookman, M. A.; Brady, M. F.; McGuire, W. P.; Harper, P. G.; Alberts, D. S.; Friedlander, M.; Colombo, N.; Fowler, J. M.; Argenta, P. A.; De Geest, K.; et al. Evaluation of New Platinum-Based Treatment Regimens in Advanced-Stage Ovarian Cancer: A Phase III Trial of the Gynecologic Cancer InterGroup. *Journal of Clinical Oncology* **2009**, *27* (9), 1419-1425.

144. Fuertes, M. A.; Alonso, C.; Pérez, J. M. Biochemical Modulation of Cisplatin Mechanisms of Action: Enhancement of Antitumor Activity and Circumvention of Drug Resistance. *Chemical Reviews* **2003**, *103* (3), 645-662.

145. Hah, S. S.; Stivers, K. M.; de Vere White, R. W.; Henderson, P. T. Kinetics of Carboplatin−DNA Binding in Genomic DNA and Bladder Cancer Cells As Determined by Accelerator Mass Spectrometry. *Chemical Research in Toxicology* **2006**, *19* (5), 622-626.

146. Brabec, V.; Kasparkova, J. Modifications of DNA by platinum complexes: Relation to resistance of tumors to platinum antitumor drugs. *Drug Resistance Updates* **2005**, *8* (3), 131-146.

147. Sousa, G. F. d.; Wlodarczyk, S. R.; Monteiro, G. Carboplatin: molecular mechanisms of action associated with chemoresistance. *Brazilian Journal of Pharmaceutical Sciences* **2014**, *50* (4), 693-701.

148. Khanna, C.; Rosenberg, M.; Vail, D. M. A Review of Paclitaxel and Novel Formulations Including Those Suitable for Use in Dogs. *Journal of Veterinary Internal Medicine* **2015**, *29* (4), 1006-1012.

149. Yang, Y.-H.; Mao, J.-W.; Tan, X.-L. Research progress on the source, production, and anti-cancer mechanisms of paclitaxel. *Chinese Journal of Natural Medicines* **2020**, *18* (12), 890-897.

150. Zhang, D.; Yang, R.; Wang, S.; Dong, Z. Paclitaxel: new uses for an old drug. *Drug Design, Development and Therapy* **2014**, *8*, 279-284.

151. Zhao, S.; Tang, Y.; Wang, R.; Najafi, M. Mechanisms of cancer cell death induction by paclitaxel: an updated review. *Apoptosis* **2022**, *27* (9), 647-667.

152. Duval, K.; Grover, H.; Han, L.-H.; Mou, Y.; Pegoraro, A. F.; Fredberg, J.; Chen, Z. Modeling Physiological Events in 2D vs. 3D Cell Culture. *Physiology* **2017**, *32* (4), 266-277.

153. Seyhan, A. A. Lost in translation: the valley of death across preclinical and clinical divide – identification of problems and overcoming obstacles. *Translational Medicine Communications* **2019**, *4* (1), 18.

154. Klemba, A.; Bodnar, L.; Was, H.; Brodaczewska, K. K.; Wcislo, G.; Szczylik, C. A.; Kieda, C. Hypoxia-Mediated Decrease of Ovarian Cancer Cells Reaction to Treatment: Significance for Chemo- and Immunotherapies. *International Journal of Molecular Sciences* **2020**, *21* (24), 9492.

155. Popova, A. A.; Tronser, T.; Demir, K.; Haitz, P.; Kuodyte, K.; Starkuviene, V.; Wajda, P.; Levkin, P. A. Facile One Step Formation and Screening of Tumor Spheroids Using Droplet-Microarray Platform. *Small* **2019**, *15* (25), 1901299.

156. Däster, S.; Amatruda, N.; Calabrese, D.; Ivanek, R.; Turrini, E.; Droeser, R. A.; Zajac, P.; Fimognari, C.; Spagnoli, G. C.; Iezzi, G.; et al. Induction of hypoxia and necrosis in multicellular tumor spheroids is associated with resistance to chemotherapy treatment. *Oncotarget* **2017**, *8* (1), 1725-1736.

157. Baker, A. F.; Malm, S. W.; Pandey, R.; Laughren, C.; Cui, H.; Roe, D.; Chambers, S. K. Evaluation of a Hypoxia Regulated Gene Panel in Ovarian Cancer. *Cancer Microenvironment* **2015**, *8* (1), 45-56.

158. Olson, M. F.; Sahai, E. The actin cytoskeleton in cancer cell motility. *Clinical & Experimental Metastasis* **2009**, *26* (4), 273-287.

159. Yamada, K. M.; Cukierman, E. Modeling Tissue Morphogenesis and Cancer in 3D. *Cell* **2007**, *130* (4), 601-610.

160. Kelm, J. M.; Timmins, N. E.; Brown, C. J.; Fussenegger, M.; Nielsen, L. K. Method for generation of homogeneous multicellular tumor spheroids applicable to a wide variety of cell types. *Biotechnology and Bioengineering* **2003**, *83* (2), 173-180.

161. Yu, L.; Chen, M. C. W.; Cheung, K. C. Droplet-based microfluidic system for multicellular tumor spheroid formation and anticancer drug testing. *Lab on a Chip* **2010**, *10* (18), 2424-2432.

162. Godugu, C.; Patel, A. R.; Desai, U.; Andey, T.; Sams, A.; Singh, M. AlgiMatrix™ Based 3D Cell Culture System as an In-Vitro Tumor Model for Anticancer Studies. *PLOS ONE* **2013**, *8* (1), e53708.

163. Lacey, L. F.; Keene, O. N.; Duquesnoy, C.; Bye, A. Evaluation of Different Indirect Measures of Rate of Drug Absorption in Comparative Pharmacokinetic Studies. *Journal of Pharmaceutical Sciences* **1994**, *83* (2), 212-215.

164. Kim, H. S.; Park, N.-H.; Chung, H. H.; Kim, J. W.; Song, Y.-S.; Kang, S.-B. Are Three Additional Cycles of Chemotherapy Useful in Patients with Advanced-stage Epithelial Ovarian Cancer After a Complete Response to Six Cycles of Intravenous Adjuvant Paclitaxel and Carboplatin?†. *Japanese Journal of Clinical Oncology* **2008**, *38* (6), 445-450.

165. Gaver, R. C.; Colombo, N.; Green, M. D.; George, A. M.; Deeb, G.; Morris, A. D.; Canetta, R. M.; Speyer, J. L.; Farmen, R. H.; Muggia, F. M. The disposition of carboplatin in ovarian cancer patients. *Cancer Chemotherapy and Pharmacology* **1988**, *22* (3), 263-270.

166. Kobayashi, H.; Gail Eckhardt, S.; Lockridge, J. A.; Rothenberg, M. L.; Sandler, A. B.; O'Bryant, C. L.; Cooper, W.; Holden, S. N.; Aitchison, R. D.; Usman, N.; et al. Safety and pharmacokinetic study of RPI.4610 (ANGIOZYME), an anti-VEGFR-1 ribozyme, in combination with carboplatin and paclitaxel in patients with advanced solid tumors. *Cancer Chemotherapy and Pharmacology* **2005**, *56* (4), 329-336.

167. Kessous, R.; Wissing, M. D.; Piedimonte, S.; Abitbol, J.; Kogan, L.; Laskov, I.; Yasmeen, A.; Salvador, S.; Lau, S.; Gotlieb, W. H. CA-125 reduction during neoadjuvant chemotherapy is associated with success of cytoreductive surgery and outcome of patients with advanced high-grade ovarian cancer. *Acta Obstetricia et Gynecologica Scandinavica* **2020**, *99* (7), 933-940.

168. Matulonis, U. A.; Sood, A. K.; Fallowfield, L.; Howitt, B. E.; Sehouli, J.; Karlan, B. Y. Ovarian cancer. *Nature Reviews Disease Primers* **2016**, *2* (1), 16061.

169. Zhou, Y.; Irwin, M. L.; Risch, H. A. Pre- and post-diagnosis body mass index, weight change, and ovarian cancer mortality. *Gynecologic Oncology* **2011**, *120* (2), 209-213.

170. Oguri, S.; Sakakibara, T.; Mase, H.; Shimizu, T.; Ishikawa, K.; Kimura, K.; Smyth, R. D. Clinical Pharmacokinetics of Carboplatin. *The Journal of Clinical Pharmacology* **1988**, *28* (3), 208-215.

171. Hansen, J. M.; Coleman, R. L.; Sood, A. K. Targeting the tumour microenvironment in ovarian cancer. *European Journal of Cancer* **2016**, *56*, 131-143.

172. Horst, E. N.; Bregenzer, M. E.; Mehta, P.; Snyder, C. S.; Repetto, T.; Yang-Hartwich, Y.; Mehta, G. Personalized models of heterogeneous 3D epithelial tumor microenvironments: Ovarian cancer as a model. *Acta Biomaterialia* **2021**, *132*, 401-420.

173. Yang, Y.; Yang, Y.; Yang, J.; Zhao, X.; Wei, X. Tumor Microenvironment in Ovarian Cancer: Function and Therapeutic Strategy. *Frontiers in Cell and Developmental Biology* **2020**, *8*.

174. Mhawech-Fauceglia, P.; Yan, L.; Sharifian, M.; Ren, X.; Liu, S.; Kim, G.; Gayther, S. A.; Pejovic, T.; Lawrenson, K. Stromal Expression of Fibroblast Activation Protein Alpha (FAP) Predicts Platinum Resistance and Shorter Recurrence in patients with Epithelial Ovarian Cancer. *Cancer Microenvironment* **2015**, *8* (1), 23-31.

175. Wang, T.-H.; Wang, H.-S.; Soong, Y.-K. Paclitaxel-induced cell death. *Cancer* **2000**, *88* (11), 2619-2628.

176. Akbarian, M.; Mahjoub, S.; Elahi, S. M.; Zabihi, E.; Tashakkorian, H. Green synthesis, formulation and biological evaluation of a novel ZnO nanocarrier loaded with paclitaxel as drug delivery system on MCF-7 cell line. *Colloids and Surfaces B: Biointerfaces* **2020**, *186*, 110686.

177. Li, J.; Gu, Y.; Zhang, W.; Bao, C.-Y.; Li, C.-R.; Zhang, J.-Y.; Liu, T.; Li, S.; Huang, J.-X.; Xie, Z.-G.; et al. Molecular Mechanism for Selective Cytotoxicity towards Cancer Cells of Diselenide-Containing Paclitaxel Nanoparticles. *International Journal of Biological Sciences* **2019**, *15* (8), 1755-1770.

178. Trielli, M. O.; Andreassen, P. R.; Lacroix, F. B.; Margolis, R. L. Differential Taxol-dependent arrest of transformed and nontransformed cells in the G1 phase of the cell cycle, and specific-related mortality of transformed cells. *Journal of Cell Biology* **1996**, *135* (3), 689-700.

179. Nowacka, M.; Sterzynska, K.; Andrzejewska, M.; Nowicki, M.; Januchowski, R. Drug resistance evaluation in novel 3D in vitro model. *Biomedicine & Pharmacotherapy* **2021**, *138*, 111536.

180. Fontoura, J. C.; Viezzer, C.; dos Santos, F. G.; Ligabue, R. A.; Weinlich, R.; Puga, R. D.; Antonow, D.; Severino, P.; Bonorino, C. Comparison of 2D and 3D cell culture models for cell growth, gene expression and drug resistance. *Materials Science and Engineering: C* **2020**, *107*, 110264.

181. Loessner, D.; Stok, K. S.; Lutolf, M. P.; Hutmacher, D. W.; Clements, J. A.; Rizzi, S. C. Bioengineered 3D platform to explore cell–ECM interactions and drug resistance of epithelial ovarian cancer cells. *Biomaterials* **2010**, *31* (32), 8494-8506.

182. Zhang, Y.; Tang, H.; Cai, J.; Zhang, T.; Guo, J.; Feng, D.; Wang, Z. Ovarian cancer-associated fibroblasts contribute to epithelial ovarian carcinoma metastasis by promoting angiogenesis, lymphangiogenesis and tumor cell invasion. *Cancer Letters* **2011**, *303* (1), 47-55.

183. Oren, R.; Addadi, Y.; Narunsky Haziza, L.; Dafni, H.; Rotkopf, R.; Meir, G.; Fishman, A.; Neeman, M. Fibroblast recruitment as a tool for ovarian cancer detection and targeted therapy. *International Journal of Cancer* **2016**, *139* (8), 1788-1798.

184. Ingber, D. E. Human organs-on-chips for disease modelling, drug development and personalized medicine. *Nature Reviews Genetics* **2022**, *23* (8), 467-491.

185. Santoro, A.; Angelico, G.; Piermattei, A.; Inzani, F.; Valente, M.; Arciuolo, D.; Spadola, S.; Mulè, A.; Zorzato, P.; Fagotti, A.; et al. Pathological Chemotherapy Response Score in Patients Affected by High Grade Serous Ovarian Carcinoma: The Prognostic Role of Omental and Ovarian Residual Disease. *Frontiers in Oncology* **2019**, *9*, 778.

186. Vasseur, S.; Guillaumond, F. Lipids in cancer: a global view of the contribution of lipid pathways to metastatic formation and treatment resistance. *Oncogenesis* **2022**, *11* (1), 46.

187. Hoy, A. J.; Nagarajan, S. R.; Butler, L. M. Tumour fatty acid metabolism in the context of therapy resistance and obesity. *Nature Reviews Cancer* **2021**, *21* (12), 753-766.

188. Lee, L.; Horowitz, J.; Frenneaux, M. Metabolic manipulation in ischaemic heart disease, a novel approach to treatment. *European Heart Journal* **2004**, *25* (8), 634-641.

189. Estañ, M. C.; Calviño, E.; Calvo, S.; Guillén-Guío, B.; Boyano-Adánez, M. d. C.; de Blas, E.; Rial, E.; Aller, P. Apoptotic Efficacy of Etomoxir in Human Acute Myeloid Leukemia Cells. Cooperation with Arsenic Trioxide and Glycolytic Inhibitors, and Regulation by Oxidative Stress and Protein Kinase Activities. *PLOS ONE* **2014**, *9* (12), e115250.

190. Cheng, S.; Wang, G.; Wang, Y.; Cai, L.; Qian, K.; Ju, L.; Liu, X.; Xiao, Y.; Wang, X. Fatty acid oxidation inhibitor etomoxir suppresses tumor progression and induces cell cycle arrest via PPARγ-mediated pathway in bladder cancer. *Clinical Science* **2019**, *133* (15), 1745-1758.

191. Dhakal, B.; Li, C. M.; Li, R.; Yeo, K.; Wright, J. A.; Gieniec, K. A.; Vrbanac, L.; Sammour, T.; Lawrence, M.; Thomas, M.; et al. The Antianginal Drug Perhexiline Displays Cytotoxicity against Colorectal Cancer Cells In Vitro: A Potential for Drug Repurposing. *Cancers* **2022**, *14* (4), 1043.

192. Ashrafian, H.; Horowitz, J. D.; Frenneaux, M. P. Perhexiline. *Cardiovascular Drug Reviews* **2007**, *25* (1), 76-97.

193. Dhakal, B.; Tomita, Y.; Drew, P.; Price, T.; Maddern, G.; Smith, E.; Fenix, K. Perhexiline: Old Drug, New Tricks? A Summary of Its Anti-Cancer Effects. *Molecules* **2023**, *28* (8), 3624.

194. Pignata, S.; C Cecere, S.; Du Bois, A.; Harter, P.; Heitz, F. Treatment of recurrent ovarian cancer. *Annals of Oncology* **2017**, *28*, viii51-viii56.

195. Stewart, C.; Ralyea, C.; Lockwood, S. Ovarian Cancer: An Integrated Review. *Seminars in Oncology Nursing* **2019**, *35* (2), 151-156.

196. Tachtsidis, A.; McInnes, L. M.; Jacobsen, N.; Thompson, E. W.; Saunders, C. M. Minimal residual disease in breast cancer: an overview of circulating and disseminated tumour cells. *Clinical & Experimental Metastasis* **2016**, *33* (6), 521-550.

197. Begicevic, R.-R.; Falasca, M. ABC Transporters in Cancer Stem Cells: Beyond Chemoresistance. *International Journal of Molecular Sciences* **2017**, *18* (11), 2362.

198. Jiang, Z. S.; Sun, Y. Z.; Wang, S. M.; Ruan, J. S. Epithelial-mesenchymal transition: potential regulator of ABC transporters in tumor progression. *Journal of Cancer* **2017**, *8* (12), 2319-2327.

199. Marzagalli, M.; Fontana, F.; Raimondi, M.; Limonta, P. Cancer Stem Cells—Key Players in Tumor Relapse. *Cancers* **2021**, *13* (3), 376.

200. Fang, D.; Nguyen, T. K.; Leishear, K.; Finko, R.; Kulp, A. N.; Hotz, S.; Van Belle, P. A.; Xu, X.; Elder, D. E.; Herlyn, M. A Tumorigenic Subpopulation with Stem Cell Properties in Melanomas. *Cancer Research* **2005**, *65* (20), 9328-9337.

201. Al-Alem, L. F.; Pandya, U. M.; Baker, A. T.; Bellio, C.; Zarrella, B. D.; Clark, J.; DiGloria, C. M.; Rueda, B. R. Ovarian cancer stem cells: What progress have we made? *The International Journal of Biochemistry & Cell Biology* **2019**, *107*, 92-103.

202. Kryczek, I.; Liu, S.; Roh, M.; Vatan, L.; Szeliga, W.; Wei, S.; Banerjee, M.; Mao, Y.; Kotarski, J.; Wicha, M. S.; et al. Expression of aldehyde

dehydrogenase and CD133 defines ovarian cancer stem cells. *International Journal of Cancer* **2012**, *130* (1), 29-39.

203. Lee, J.-S.; Oh, S.-J.; Choi, H.-J.; Kang, J. H.; Lee, S.-H.; Ha, J. S.; Woo, S. M.; Jang, H.; Lee, H.; Kim, S.-Y. ATP Production Relies on Fatty Acid Oxidation Rather than Glycolysis in Pancreatic Ductal Adenocarcinoma. *Cancers* **2020**, *12* (9), 2477.

204. Lee, J.-S.; Kim, S. H.; Lee, S.; Kang, J. H.; Lee, S.-H.; Cheong, J.-H.; Kim, S.-Y. Gastric cancer depends on aldehyde dehydrogenase 3A1 for fatty acid oxidation. *Scientific Reports* **2019**, *9* (1), 16313.

205. Huang, S. Non-genetic heterogeneity of cells in development: more than just noise. *Development* **2009**, *136* (23), 3853-3862.

206. Tomlinson, I.; Sasieni, P.; Bodmer, W. How Many Mutations in a Cancer? *The American Journal of Pathology* **2002**, *160* (3), 755-758.

207. Brock, A.; Chang, H.; Huang, S. Non-genetic heterogeneity — a mutation-independent driving force for the somatic evolution of tumours. *Nature Reviews Genetics* **2009**, *10* (5), 336-342.

208. Barzgar Barough, N.; Sajjadian, F.; Jalilzadeh, N.; Shafaei, H.; Velaei, K. Understanding breast cancer heterogeneity through non-genetic heterogeneity. *Breast Cancer* **2021**, *28* (4), 777-791.

209. Hu, Z.; Artibani, M.; Alsaadi, A.; Wietek, N.; Morotti, M.; Shi, T.; Zhong, Z.; Santana Gonzalez, L.; El-Sahhar, S.; Carrami, E. M.; et al. The Repertoire of Serous Ovarian Cancer Non-genetic Heterogeneity Revealed by Single-Cell Sequencing of Normal Fallopian Tube Epithelial Cells. *Cancer Cell* **2020**, *37* (2), 226-242.e227.

210. Konecny, G. E.; Wang, C.; Hamidi, H.; Winterhoff, B.; Kalli, K. R.; Dering, J.; Ginther, C.; Chen, H.-W.; Dowdy, S.; Cliby, W.; et al. Prognostic and Therapeutic Relevance of Molecular Subtypes in High-Grade Serous Ovarian Cancer. *JNCI: Journal of the National Cancer Institute* **2014**, *106* (10), dju249.

211. Tan, T. Z.; Miow, Q. H.; Huang, R. Y.-J.; Wong, M. K.; Ye, J.; Lau, J. A.; Wu, M. C.; Bin Abdul Hadi, L. H.; Soong, R.; Choolani, M.; et al. Functional genomics identifies five distinct molecular subtypes with clinical relevance and pathways for growth control in epithelial ovarian cancer. *EMBO Molecular Medicine* **2013**, *5* (7), 1051-1066.

212. Thiery, J. P.; Sleeman, J. P. Complex networks orchestrate epithelial–mesenchymal transitions. *Nature Reviews Molecular Cell Biology* **2006**, *7* (2), 131-142.

213. Yang, M.-H.; Hsu, D. S.-S.; Wang, H.-W.; Wang, H.-J.; Lan, H.-Y.; Yang, W.-H.; Huang, C.-H.; Kao, S.-Y.; Tzeng, C.-H.; Tai, S.-K.; et al. Bmi1 is essential in Twist1-induced epithelial–mesenchymal transition. *Nature Cell Biology* **2010**, *12* (10), 982-992.

214. Ince, T. A.; Sousa, A. D.; Jones, M. A.; Harrell, J. C.; Agoston, E. S.; Krohn, M.; Selfors, L. M.; Liu, W.; Chen, K.; Yong, M.; et al. Characterization of twenty-five ovarian tumour cell lines that phenocopy primary tumours. *Nature Communications* **2015**, *6* (1), 7419.

215. Yao, C.-H.; Liu, G.-Y.; Wang, R.; Moon, S. H.; Gross, R. W.; Patti, G. J. Identifying off-target effects of etomoxir reveals that carnitine palmitoyltransferase I is essential for cancer cell proliferation independent of β-oxidation. *PLOS Biology* **2018**, *16* (3), e2003782.

216. Schlaepfer, I. R.; Joshi, M. CPT1A-mediated Fat Oxidation, Mechanisms, and Therapeutic Potential. *Endocrinology* **2020**, *161* (2), bqz046.

217. Paraiso, W. K. D.; Garcia-Chica, J.; Ariza, X.; Zagmutt, S.; Fukushima, S.; Garcia, J.; Mochida, Y.; Serra, D.; Herrero, L.; Kinoh, H.; et al. Poly-ion complex micelles effectively deliver CoA-conjugated CPT1A inhibitors to modulate lipid metabolism in brain cells. *Biomaterials Science* **2021**, *9* (21), 7076-7091.

218. Bowman, T. A.; O'Keeffe, K. R.; D'Aquila, T.; Yan, Q. W.; Griffin, J. D.; Killion, E. A.; Salter, D. M.; Mashek, D. G.; Buhman, K. K.; Greenberg, A. S. Acyl CoA synthetase 5 (ACSL5) ablation in mice increases energy expenditure and insulin sensitivity and delays fat absorption. *Molecular Metabolism* **2016**, *5* (3), 210-220.

219. Iacoangeli, A.; Lin, T.; Al Khleifat, A.; Jones, A. R.; Opie-Martin, S.; Coleman, J. R. I.; Shatunov, A.; Sproviero, W.; Williams, K. L.; Garton, F.; et al. Genome-wide Meta-analysis Finds the ACSL5-ZDHHC6 Locus Is Associated with ALS and Links Weight Loss to the Disease Genetics. *Cell Reports* **2020**, *33* (4), 108323.

220. Pan, X.; Zhang, X.; Ban, J.; Yue, L.; Ren, L.; Chen, S. Effects of High-Fat Diet on Cardiovascular Protein Expression in Mice Based on Proteomics. *Diabetes, Metabolic Syndrome and Obesity* **2023**, *16*, 873-882.

221. Peng, P.; Liu, Y.; Zheng, W.; Han, B.; Wang, K.; Sun, D. Identification of Genetic Effects of ACADVL and IRF6 Genes with Milk Production Traits of Holstein Cattle in China. *Genes* **2022**, *13* (12), 2393.

222. Goetzman, E. S.; Wang, Y.; He, M.; Mohsen, A.-W.; Ninness, B. K.; Vockley, J. Expression and characterization of mutations in human very long-chain acyl-CoA dehydrogenase using a prokaryotic system. *Molecular Genetics and Metabolism* **2007**, *91* (2), 138-147.

223. Lundsgaard, A.-M.; Fritzen, A. M.; Kiens, B. Chapter 36 - Exercise Physiology in Men and Women. In *Principles of Gender-Specific Medicine (Third Edition)*, Legato, M. J. Ed.; Academic Press, 2017; pp 525-542.

224. Connaughton, S.; Chowdhury, F.; Attia, R. R.; Song, S.; Zhang, Y.; Elam, M. B.; Cook, G. A.; Park, E. A. Regulation of pyruvate dehydrogenase

kinase isoform 4 (PDK4) gene expression by glucocorticoids and insulin. *Molecular and Cellular Endocrinology* **2010**, *315* (1), 159-167.

225. Wang, J.; Qian, Y.; Gao, M. Overexpression of PDK4 is associated with cell proliferation, drug resistance and poor prognosis in ovarian cancer. *Cancer Management and Research* **2019**, *11*, 251-262.

226. Wu, Z.; Sun, J.; Liao, Z.; Qiao, J.; Chen, C.; Ling, C.; Wang, H. An update on the therapeutic implications of long-chain acyl-coenzyme A synthetases in nervous system diseases. *Frontiers in Neuroscience* **2022**, *16*, 1030512.

227. Ellis, J. M.; Li, L. O.; Wu, P.-C.; Koves, T. R.; Ilkayeva, O.; Stevens, R. D.; Watkins, S. M.; Muoio, D. M.; Coleman, R. A. Adipose Acyl-CoA Synthetase-1 Directs Fatty Acids toward β-Oxidation and Is Required for Cold Thermogenesis. *Cell Metabolism* **2010**, *12* (1), 53-64.

228. Young, P. A.; Senkal, C. E.; Suchanek, A. L.; Grevengoed, T. J.; Lin, D. D.; Zhao, L.; Crunk, A. E.; Klett, E. L.; Füllekrug, J.; Obeid, L. M.; Coleman, R. A. Long-chain acyl-CoA synthetase 1 interacts with key proteins that activate and direct fatty acids into niche hepatic pathways. *Journal of Biological Chemistry* **2018**, *293* (43), 16724-16740.

229. Liu, H.; Liu, J.-Y.; Wu, X.; Zhang, J.-T. Biochemistry, molecular biology, and pharmacology of fatty acid synthase, an emerging therapeutic target and diagnosis/prognosis marker. *International journal of biochemistry and molecular biology* **2010**, *1* (1), 69-89.

230. Fhu, C. W.; Ali, A. Fatty Acid Synthase: An Emerging Target in Cancer. *Molecules* **2020**, *25* (17), 3935.

231. Paton, C. M.; Ntambi, J. M. Biochemical and physiological function of stearoyl-CoA desaturase. *American Journal of Physiology-Endocrinology and Metabolism* **2009**, *297* (1), E28-E37.

232. Gao, Y.; Li, J.; Xi, H.; Cui, J.; Zhang, K.; Zhang, J.; Zhang, Y.; Xu, W.; Liang, W.; Zhuang, Z.; et al. Stearoyl-CoA-desaturase-1 regulates gastric cancer stem-like properties and promotes tumour metastasis via Hippo/YAP pathway. *British Journal of Cancer* **2020**, *122* (12), 1837-1847.

233. Khayami, R.; Hashemi, S. R.; Kerachian, M. A. Role of aldo-keto reductase family 1 member B1 (AKR1B1) in the cancer process and its therapeutic potential. *Journal of Cellular and Molecular Medicine* **2020**, *24* (16), 8890-8902.

234. Barski, O. A.; Tipparaju, S. M.; Bhatnagar, A. The Aldo-Keto Reductase Superfamily and its Role in Drug Metabolism and Detoxification. *Drug Metabolism Reviews* **2008**, *40* (4), 553-624.

235. van Weverwijk, A.; Koundouros, N.; Iravani, M.; Ashenden, M.; Gao, Q.; Poulogiannis, G.; Jungwirth, U.; Isacke, C. M. Metabolic adaptability in

metastatic breast cancer by AKR1B10-dependent balancing of glycolysis and fatty acid oxidation. *Nature Communications* **2019**, *10* (1), 2698.

236. Shiiba, M.; Yamagami, H.; Yamamoto, A.; Minakawa, Y.; Okamoto, A.; Kasamatsu, A.; Sakamoto, Y.; Uzawa, K.; Takiguchi, Y.; Tanzawa, H. Mefenamic acid enhances anticancer drug sensitivity via inhibition of aldo-keto reductase 1C enzyme activity. *Oncology Reports* **2017**, *37* (4), 2025-2032.

237. Wadman, M. FDA no longer has to require animal testing for new drugs. *Science* **2023**, *379* (6628), 127-128.

238. Kola, I.; Landis, J. Can the pharmaceutical industry reduce attrition rates? *Nature Reviews Drug Discovery* **2004**, *3* (8), 711-716.

239. Hu, Z.; Cunnea, P.; Zhong, Z.; Lu, H.; Osagie, O. I.; Campo, L.; Artibani, M.; Nixon, K.; Ploski, J.; Santana Gonzalez, L.; et al. The Oxford Classic Links Epithelial-to-Mesenchymal Transition to Immunosuppression in Poor Prognosis Ovarian Cancers. *Clinical Cancer Research* **2021**, *27* (5), 1570-1579.

240. Xiao, Y.; Yu, D. Tumor microenvironment as a therapeutic target in cancer. *Pharmacology & Therapeutics* **2021**, *221*, 107753.

241. Yao, Q.; Qu, X.; Yang, Q.; Wei, M.; Kong, B. CLIC4 mediates TGF-β1-induced fibroblast-to-myofibroblast transdifferentiation in ovarian cancer. *Oncology Reports* **2009**, *22* (3), 541-548.

242. Anderle, N.; Koch, A.; Gierke, B.; Keller, A.-L.; Staebler, A.; Hartkopf, A.; Brucker, S. Y.; Pawlak, M.; Schenke-Layland, K.; Schmees, C. A Platform of Patient-Derived Microtumors Identifies Individual Treatment Responses and Therapeutic Vulnerabilities in Ovarian Cancer. *Cancers* **2022**, *14* (12), 2895.

243. Freyre, C. A. C.; Rauher, P. C.; Ejsing, C. S.; Klemm, R. W. MIGA2 Links Mitochondria, the ER, and Lipid Droplets and Promotes De Novo Lipogenesis in Adipocytes. *Molecular Cell* **2019**, *76* (5), 811-825.e814.